JETP Letters, Vol. 80, No. 12, 2004, pp. 715–720. From Pis'ma v Zhurnal Éksperimental'noĭ i Teoreticheskoĭ Fiziki, Vol. 80, No. 12, 2004, pp. 845–849.

Systematization of Tensor Mesons and the Determination of the 2^{++} Glueball¶

V. V. Anisovich

St. Petersburg Nuclear Physics Institute, Gatchina, 188300 Russia

e-mail: anisovic@pnpi.spb.ru

Received November 22, 2004

It is shown that new data on the ($J^{PC} = 2^{++}$) resonances in the mass range $M \sim 1700$–2400 MeV support the linearity of the (n, M^2) trajectories, where n is the radial quantum number of the quark–antiquark state. In this way, all the vacancies for the isoscalar tensor $q\bar{q}$ mesons in the range up to 2450 MeV are filled in. This allows one to fix the broad f_2 state with $M = 2000 \pm 30$ MeV and $\Gamma = 530 \pm 40$ MeV as the lowest-tensor glueball.
© 2004 MAIK "Nauka/Interperiodica".

PACS numbers: 12.38.–t; 12.39.Mk; 14.40.–n

Recent phase space analysis of the process $\gamma\gamma \longrightarrow K_S K_S$ [1] and reanalysis of the $\phi\phi$ spectra [2] observed in the reaction $\pi^- p \longrightarrow \phi\phi n$ [3] have clarified the situation with f_2 mesons in the mass region 1700–2400 MeV. Hence, now one may definitely speak about the location of $q\bar{q}$ states on the (n, M^2) trajectories [4] (see also [5, 6]). This fact enables us to determine which one of f_2 mesons is an extra state for the (n, M^2) trajectories. Such an extra state is the broad resonance $f_2(2000 \pm 30)$. According to [2, 7, 8], its parameters are as follows:

$$M = 2050 \pm 30 \text{ MeV}, \quad \Gamma = 570 \pm 70 \text{ MeV [2]},$$
$$M = 1980 \pm 20 \text{ MeV}, \quad \Gamma = 520 \pm 50 \text{ MeV [7]}, \quad (1)$$
$$M = 2010 \pm 25 \text{ MeV}, \quad \Gamma = 495 \pm 35 \text{ MeV [8]}.$$

In [4], we have put quark–antiquark meson states with different radial excitations ($n = 1, 2, 3, 4, \ldots$) on the (n, M^2) trajectories. With a good accuracy, the trajectories occurred as linear:

$$M^2 = M_0^2 + (n-1)\mu^2, \quad (2)$$

with a universal slope $\mu^2 = 1.2 \pm 0.1$ GeV^2; M_0 is the mass of the lowest (basic) state. For the ($I = 0$, $J^{PC} = 2^{++}$) mesons, the present status of the trajectories (i.e., with the results given by [1, 2]) is shown in the figure.

The quark states with ($I = 0$, $J^{PC} = 2^{++}$) are defined by two flavor components, $n\bar{n} = (u\bar{u} + d\bar{d})/\sqrt{2}$ and $s\bar{s}$, with $^{2S+1}L_J = {}^3P_2, {}^3F_2$. Generally, all mesons are a mixture of the flavor component in the P and F waves. But, as concerns the f_2 mesons with $M \lesssim 2$ GeV, they are dominated by the flavor component $n\bar{n}$ or $s\bar{s}$ in a definite P or F wave. The f_2 mesons shown in the figure, which belong to four trajectories, are dominated by the following states:

$$[f_2(1275), f_2(1580), f_2(1920), f_2(2240)] \longrightarrow {}^3P_2 n\bar{n},$$
$$[f_2(1525), f_2(1755), f_2(2120), f_2(2410)] \longrightarrow {}^3P_2 s\bar{s}, \quad (3)$$
$$[f_2(2020), f_2(2300)] \longrightarrow {}^3F_2 n\bar{n},$$
$$f_2(2340) \longrightarrow {}^3F_2 s\bar{s}.$$

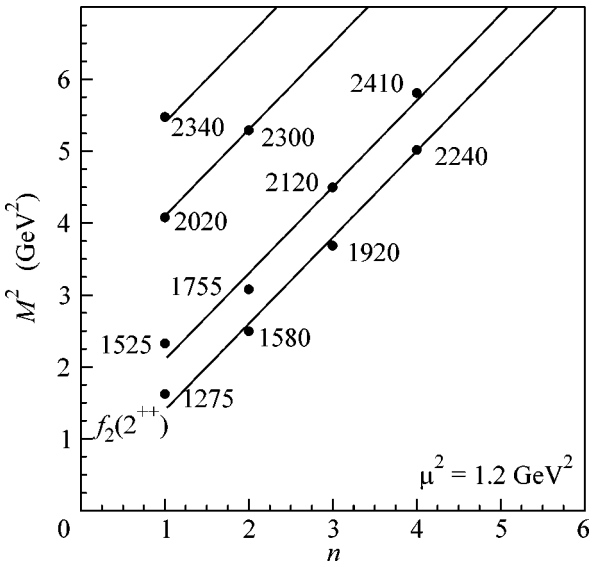

The f_2 trajectories on the (n, M^2) plane; n is the radial quantum number of the $q\bar{q}$ state. The numbers stand for the experimentally observed f_2 meson masses M.

¶ This article was submitted by the author in English.

0021-3640/04/8012-0715$26.00 © 2004 MAIK "Nauka/Interperiodica"

The constants of the tensor glueball decay into two mesons in the leading (planar diagrams) and next-to-leading (nonplanar diagrams) terms of the $1/N$ expansion. The mixing angles for the η–η' and ω–ϕ mesons are defined as follows: $\eta = n\bar{n}\cos\theta - s\bar{s}\sin\theta$, $\eta' = n\bar{n}\sin\theta + s\bar{s}\cos\theta$ and $\omega = n\bar{n}\cos\varphi_V - s\bar{s}\sin\varphi_V$, $\phi = n\bar{n}\sin\varphi_V + s\bar{s}\cos\varphi_V$. Because of the small value of φ_V, we kept in the table only the terms of the order of φ_V

Channel	Constants for glueball decays in the leading order of $1/N$ expansion	Constants for glueball decays in the next-to-leading order of $1/N$ expansion	Identity factor for decay products
$\pi^0\pi^0$	G_P^L	0	1/2
$\pi^+\pi^-$	G_P^L	0	1
K^+K^-	$\sqrt{\lambda}G_P^L$	0	1
$K^0\bar{K}^0$	$\sqrt{\lambda}G_P^L$	0	1
$\eta\eta$	$G_P^L(\cos^2\theta + \lambda\sin^2\theta)$	$2G_P^{NL}\left(\cos^2\theta - \sqrt{\frac{\lambda}{2}}\sin^2\theta\right)^2$	1/2
$\eta\eta'$	$G_P^L(1-\lambda)\sin\theta\cos\theta$	$2G_P^{NL}\left(\cos\theta - \sqrt{\frac{\lambda}{2}}\sin\theta\right)\left(\sin\theta + \sqrt{\frac{\lambda}{2}}\cos\theta\right)$	1
$\eta'\eta'$	$G_P^L(\sin^2\theta + \lambda\cos^2\theta)$	$2G_P^{NL}\left(\sin\theta + \sqrt{\frac{\lambda}{2}}\cos\theta\right)^2$	1/2
$\rho^0\rho^0$	G_V^L	0	1/2
$\rho^+\rho^-$	G_V^L	0	1
$K^{*+}K^{*-}$	$\sqrt{\lambda}G_V^L$	0	1
$K^{*0}\bar{K}^{*0}$	$\sqrt{\lambda}G_V^L$	0	1
$\omega\omega$	G_V^L	$2G_V^{NL}$	1/2
$\omega\phi$	$G_V^L(1-\lambda)\varphi_V$	$2G_V^{NL}\left(\sqrt{\frac{\lambda}{2}} + \varphi_V\left(1 - \frac{\lambda}{2}\right)\right)$	1
$\phi\phi$	λG_V^L	$2G_V^{NL}\left(\frac{\lambda}{2} + \sqrt{2\lambda}\varphi_V\right)$	1/2

To avoid the confusion, in (3), the experimentally observed masses of mesons are shown: these are the magnitudes drawn in the figure but not those from the compilation [9].

Let us discuss the states that lie on the trajectories of the figure.

The trajectory [$f_2(1275)$, $f_2(1580)$, $f_2(1920)$, $f_2(2240)$]. (1) $f_2(1275)$. This resonance is almost pure $1^3P_2 n\bar{n}$ state: this is favored by the comparison of the branching ratios $f_2(1275) \longrightarrow \pi\pi$, $\eta\eta$, $K\bar{K}$ with the quark model calculations. The dominance of the $1^3P_2 n\bar{n}$ component is also supported by the value of the partial width of the decay $f_2(1275) \longrightarrow \gamma\gamma$ [10, 11].

(2) $f_2(1580)$ (in compilation [9], it is denoted as $f_2(1565)$). About ten years ago, there existed a number of indications of the presence of 2^{++} mesons in the vicinity of 1500 MeV [12–15]. After the discovery of a strong signal in the 0^{++} wave related to the $f_0(1500)$ [16, 17], as well as correct account being taken for the interference of the 0^{++} and 2^{++} waves, the resonance signal in the 2^{++} wave moved towards higher masses, ~1570 MeV. According to the latest combined analysis of meson spectra [6, 18], this resonance has the following characteristics (see Table 1 in [6]):

$$M = 1580 \pm 6 \text{ MeV}, \quad \Gamma = 160 \pm 20 \text{ MeV}. \qquad (4)$$

Hadronic decays, together with the partial width in the channel $\gamma\gamma$ [10], support the $f_2(1580)$ as a system with a dominant $n\bar{n}$ component.

In [9], the $f_2(1640)$ state is marked as a separate resonance: this identification is based on resonance signals at $M = 1620 \pm 16$ MeV [19] (Mark 3 data for $J/\Psi \longrightarrow \gamma\pi^+\pi^-\pi^+\pi^-$), $M = 1647 \pm 7$ MeV [13] (reaction $\bar{n}p \longrightarrow 3\pi^+2\pi^-$), $M = 1590 \pm 30$ MeV [20], 1635 ± 7 MeV [21] (reaction $\pi^-p \longrightarrow \omega\omega n$). Without doubt, these signals are the reflections of $f_2(1580 \pm 20)$, and the data [19, 20] do not contradict this fact. In [9], the mass of this state is determined as 1638 ± 6 MeV, which reflects small errors in the mass definition in [13, 21].

(3) $f_2(1920)$ (in compilation [9], it is denoted as $f_2(1910)$). This resonance was observed in the signals $\omega\omega$ [20–22] and $\eta\eta'$ [23, 24]. In [8], the $f_2(1920)$ is seen as a shoulder in the $p\bar{p}$ ($I = 0$, $C = +1$) $\longrightarrow \pi^0\pi^0$, $\eta\eta$, $\eta\eta'$ spectra in the wave ${}^3P_2 p\bar{p}$. According to [6, 18],

$$M = 1920 \pm 40 \text{ MeV}, \quad \Gamma = 260 \pm 40 \text{ MeV}. \quad (5)$$

A strong signal in the channels with nonstrange mesons surmises a large $n\bar{n}$ component in the $f_2(1920)$.

(4) $f_2(2240)$. It is seen in the spectra $p\bar{p}$ ($I = 0$, $C = +1$) $\longrightarrow \pi^0\pi^0$, $\eta\eta$, $\eta\eta'$, in the wave ${}^3P_2 p\bar{p}$ [8]. According to [6, 18],

$$M = 2240 \pm 30 \text{ MeV}, \quad \Gamma = 245 \pm 45 \text{ MeV}. \quad (6)$$

The decay of $f_2(2240)$ into channels with nonstrange mesons makes it very similar to the assumption about a considerable $n\bar{n}$ component.

(5) The next radial excitation on the ${}^3P_2 n\bar{n}$ trajectory ($n = 5$) is predicted at 2490 MeV.

The trajectory [$f_2(1525)$, $f_2(1755)$, $f_2(2120)$, $f_2(2410)$]. This is the meson trajectory with a dominant $s\bar{s}$ component. The states lying on this trajectory are the nonet partners of mesons from the first trajectory [$f_2(1275)$, $f_2(1580)$, $f_2(1920)$, $f_2(2240)$]. This suggests a dominance of the P wave in these $q\bar{q}$ systems: ${}^3P_2 q\bar{q}$.

(1) $f_2(1525)$. This is the basic state ($n = 1$), the nonet partner of $f_2(1275)$. The mixing angle of the $n\bar{n}$ and $s\bar{s}$ components, which can be determined neglecting the gluonium admixture,

$$\begin{aligned} f_2(1275) &= n\bar{n}\cos\varphi_{n=1} + s\bar{s}\sin\varphi_{n=1}, \\ f_2(1525) &= -n\bar{n}\sin\varphi_{n=1} + s\bar{s}\cos\varphi_{n=1}, \end{aligned} \quad (7)$$

may be evaluated from the value of the partial widths $\gamma\gamma$ and the ratios of the decay channels $\pi\pi$, $K\bar{K}$, $\eta\eta$ within the frame of quark combinatorics (see [5], Chapter 5, and references therein). The evaluations given in [1, 10] provide us with the mixing angle as follows:

$$\varphi_{n=1} = -1^\circ \pm 3^\circ. \quad (8)$$

(2) $f_2(1755)$. This state belongs to the nonet of the first radial excitation, $n = 2$; it is dominantly in the P wave $s\bar{s}$ state. The mixing angle $\varphi_{n=2}$ can be evaluated using the data on $\gamma\gamma \longrightarrow K_S K_S$. Neglecting a possible admixture of the glueball component, it was found [1]:

$$\begin{aligned} f_2(1580) &= n\bar{n}\cos\varphi_{n=2} + s\bar{s}\sin\varphi_{n=2}, \\ f_2(1755) &= -n\bar{n}\sin\varphi_{n=2} + s\bar{s}\cos\varphi_{n=1}, \\ \varphi_{n=2} &= -10^{\circ\,+5^\circ}_{-10^\circ}. \end{aligned} \quad (9)$$

(3) $f_2(2120)$. This resonance was observed in the $\phi\phi$ spectrum in the reaction $\pi^-p \longrightarrow n\phi\phi$ [3]. At small momenta transferred to the nucleon, the pion exchange dominates; as a result, we have the transition $\pi\pi \longrightarrow \phi\phi$. The $f_2(2120)$ resonance is seen in the $\phi\phi$ system in the S wave with the spin 2 (the state S_2). According to [2], its parameters are as follows:

$$\begin{gathered} M = 2120 \pm 30 \text{ MeV}, \quad \Gamma = 290 \pm 60 \text{ MeV}, \\ W(S_2) \simeq 90\%, \end{gathered} \quad (10)$$

where $W(S_2)$ is the probability of the S_2 wave. The previous analysis [3], which did not account for the existence of the broad f_2 state around 2000 MeV, provided the value $M \simeq 2010$ MeV, $\Gamma \simeq 200$ MeV [3]; accordingly, this resonance was denoted as $f_2(2010)$ in [9]. At the same time, there is a resonance denoted in [9] as $f_2(2150)$, which was observed in the spectra $\eta\eta$, $\eta\eta'$, $K\bar{K}$, which assumes a large $s\bar{s}$ component:

$$\begin{gathered} \eta\eta\ [25]\colon M = 2151 \pm 16 \text{ MeV}, \quad \Gamma = 280 \pm 70 \text{ MeV}, \\ \eta\eta\ [26]\colon 2130 \pm 35 \text{ MeV}, \quad \Gamma = 130 \pm 30 \text{ MeV}, \\ \eta\eta, \eta\eta'\ [27]\colon 2105 \pm 10 \text{ MeV}, \\ \Gamma = 200 \pm 25 \text{ MeV}, \\ \eta\eta\ [15]\colon 2104 \pm 20 \text{ MeV}, \quad \Gamma = 203 \pm 10 \text{ MeV}, \\ K\bar{K}\ [28]\colon 2130 \pm 35 \text{ MeV}, \quad \Gamma = 270 \pm 50 \text{ MeV}. \end{gathered} \quad (11)$$

The reanalysis [2] points definitely to the fact that the resonances denoted in [9] as $f_2(2010)$ and $f_2(2150)$ are actually the same state.

(4) $f_2(2410)$. It is seen in the reaction $\pi^-p \longrightarrow n\phi\phi$ [3]. According to the reanalysis [2], its parameters are as follows:

$$\begin{gathered} M = 2410 \pm 30 \text{ MeV}, \quad \Gamma = 360 \pm 70 \text{ MeV}, \\ W(S_2) \simeq 50\%, \quad W(D_0) \simeq 20\%, \quad W(D_2) \simeq 30\%. \end{gathered} \quad (12)$$

If the contribution of the broad f_2 state in the region 2000 MeV is neglected, the resonance parameters move to smaller values: $M \simeq 2340$ MeV, $\Gamma \simeq 320$ MeV [3]; correspondingly, in [9], it was denoted as $f_2(2340)$.

(5) The linearity of the (n, M^2) trajectory predicts the next ${}^3P_2 s\bar{s}$ state at 2630 MeV ($n = 5$).

The states with a dominant ${}^3F_2 n\bar{n}$ component. For the time being, we may speak about the observation of the two states with the dominant ${}^3F_2 n\bar{n}$ component.

(1) $f_2(2020)$. It is seen in the partial wave analysis of the reactions $p\bar{p} \longrightarrow \pi^0\pi^0, \eta\eta, \eta\eta'$, in the wave ${}^3F_2 p\bar{p}$ [8]. According to [6, 18], its parameters are as follows:

$$M = 2020 \pm 30 \text{ MeV}, \quad \Gamma = 275 \pm 35 \text{ MeV}. \quad (13)$$

In [9], this meson was placed in the Section "other light mesons"; it is denoted as $f_2(2000)$. This is the basic ${}^3F_2$ meson ($n = 1$) with the dominant $n\bar{n}$ component.

(2) $f_2(2300)$. It is seen in the partial wave analysis of the reaction $p\bar{p} \longrightarrow \pi^0\pi^0, \eta\eta, \eta\eta'$, in the wave ${}^3F_2 p\bar{p}$ [8]. According to [6, 18], its parameters are as follows:

$$M = 2300 \pm 35 \text{ MeV}, \quad \Gamma = 290 \pm 50 \text{ MeV}. \quad (14)$$

This is the first radial excitation of the ${}^3F_2$ state ($n = 2$) with a dominant $n\bar{n}$ component. There is a resonance denoted in [9] as $f_2(2300)$, but this is the state observed in the $\phi\phi$ spectrum [3], the mass and width of which, in accordance with the reanalysis [2], are 2340 ± 15 and 150 ± 50 MeV; of course, they are different states (see the discussion below).

(3) The second radial excitation state ($n = 3$) on the trajectory ${}^3F_2 n\bar{n}$ is predicted to be at $M \simeq 2550$ MeV.

The state with the dominant ${}^3F_2 s\bar{s}$ component. This trajectory is marked only by one observed state.

(1) $f_2(2340)$. It is seen in the $\phi\phi$ spectrum [3] and $\gamma\gamma \longrightarrow K^+K^-$ [29] with the mass ~2330 MeV and width 275 ± 60 MeV. According to [2],

$$M = 2340 \pm 15 \text{ MeV}, \quad \Gamma = 150 \pm 50 \text{ MeV},$$
$$W(S_2) \simeq 10\%, \quad W(D_0) \simeq 10\%, \quad W(D_2) \simeq 80\%. \quad (15)$$

In the previous analysis of the $\phi\phi$ spectrum [3], this resonance had a mass of 2300 MeV; in [9], it is denoted as $f_2(2300)$.

(2) The next state on the ${}^3F_2 s\bar{s}$ trajectory ($n = 2$) should be located near $M \simeq 2575$ MeV.

The broad 2^{++} state near 2000 MeV—the tensor glueball. Averaging over the parameters of the broad resonance using the data in [2, 7, 8] (see (1)) gives us the following values:

$$M = 2000 \pm 30 \text{ MeV}, \quad \Gamma = 530 \pm 40 \text{ MeV}. \quad (16)$$

This broad state is superfluous with respect to the $q\bar{q}$ trajectories on the (n, M^2) plane, i.e., it is the exotics. It is reasonable to believe that this is the lowest tensor glueball. This statement is favored by the estimates of the parameters of the pomeron trajectory (e.g., see [5], Chapter 5.4, and references therein), according to which $M_{2^{++}\text{glueball}} \simeq 1.7$–$2.5$ GeV. The lattice calculations result in a close value, namely, 2.2–2.4 GeV [30].

Another characteristic signature of the glueball is its large width, which was especially emphasized in [31]. The problem is that the exotic state accumulates the widths of its neighbors resonances due to the transitions *meson*(1) $\longrightarrow$ *real mesons* $\longrightarrow$ *meson*(2).

Precisely this phenomenon took place with the lightest scalar glueball near 1500 MeV: the decay processes led to a strong mixing of the glueball with the neighboring resonances; consequently, the glueball turned into the broad resonance $f_0(1200$–$1600)$ [32–35] (see also the discussion in [6]). Of course, the width of this scalar isoscalar state is rather large, though its precise value is poorly determined: $\Gamma \simeq 500$–1500 MeV. Although the accuracy in the determination of the absolute value is low, the ratios of the partial widths of this state to the channels $\pi\pi$, $K\bar{K}$, $\eta\eta$, $\eta\eta'$ are well defined [36]. As a result, the ratios $\Gamma(\pi\pi) : \Gamma(K\bar{K}) : \Gamma(\eta\eta) : \Gamma(\eta\eta')$ tell us definitely that $f_0(1200$–$1600)$ is a mixture of the gluonium (gg) and quarkonium ($q\bar{q}$) components being close to the flavor singlet $(q\bar{q})_{\text{glueball}}$. Namely,

$$gg\cos\gamma + (q\bar{q})_{\text{glueball}}\sin\gamma,$$
$$(q\bar{q})_{\text{glueball}} = n\bar{n}\cos\varphi_{\text{glueball}} + s\bar{s}\sin\varphi_{\text{glueball}} \quad (17)$$

with $\varphi_{\text{glueball}} = \arctan\sqrt{\lambda/2} \simeq 26°$–$33°$. The mixing angle $\varphi_{\text{glueball}}$ is determined by the fact that the gluon field creates the light quark pairs with probabilities $u\bar{u} : d\bar{d} : s\bar{s} = 1 : 1 : \lambda$ and the probability to produce strange quarks (λ) is suppressed $\lambda \simeq 0.5$–0.8 (see [37] and the discussion in Chapter 5 of [5]). The mixing angle γ for gluonium and quarkonium components cannot be defined by the ratios $\Gamma(\pi\pi) : \Gamma(K\bar{K}) : \Gamma(\eta\eta) : \Gamma(\eta\eta')$; it should be fixed by radiative transitions, for example, $\gamma\gamma \longrightarrow f_0(1200$–$1600)$; such experimental information is still missing. One may find a detailed discussion of the situation in [5, 6].

If the broad resonance $f_2(2000)$ is the tensor glueball, it must also be the mixture of components gg and $(q\bar{q})_{\text{glueball}}$. Then, the decay vertices of $f_2(2000) \longrightarrow$

$\pi\pi$, $K\bar{K}$, $\eta\eta$, $\eta\eta'$, $\eta'\eta'$ and $f_2(2000) \longrightarrow \omega\omega$, $\rho\rho$, K^*K^*, $\phi\phi$, $\phi\omega$ should obey the constraints shown in the table.

The decays *glueball* $\longrightarrow$ *two* $q\bar{q}$ *mesons* may be realized through both planar quark–gluon diagrams and nonplanar ones, the contribution from nonplanar diagrams being suppressed in terms of the $1/N$-expansion [38]. One may expect that, in the next-to-leading order, the vertices are suppressed as $G_P^{NL}/G_P^L \sim 1/10$, $G_V^{NL}/G_V^L \sim 1/10$; in any case, such a level of suppression is observed in the decay of the scalar glueball $f_0(1200–1600)$ [39]. Therefore, the next-to-leading terms are important for the channel *glueball* $\longrightarrow \omega\phi$ only; for other channels, they may be omitted.

In particle data compilation [9], there is a narrow state $f_J(2220)$ with $J^{PC} = 2^{++}$ or 4^{++} and $\Gamma \simeq 23$ MeV, which is sometimes discussed as a candidate for a tensor glueball under the assumption $J = 2$ (see [40] and references therein). If this state does exist with $J = 2$, we see that there is no room for it on the $q\bar{q}$ trajectories shown in Fig. 1: in this case, it should also be considered as an exotic state.

In the mean time, there exist two statements about the value of the glueball width: according to [41], it should be less than the hadronic widths of the $q\bar{q}$ mesons, while, following [6, 31], it must be considerably greater. The arguments given in [41] are based on the evaluation of the decay couplings in lattice calculations. However, such calculations do not take into account the large-distance processes such as *meson*(1) $\longrightarrow$ *real mesons* $\longrightarrow$ *meson*(2) in case of resonance overlapping. Precisely these transitions are responsible for the large width of the state, which is exotic as a result of its origin [31]. The phenomenon of width accumulation for meson resonances was studied in [32–35], but, much earlier, this phenomenon was observed in nuclear physics [42–44]. Therefore, I think that, at the present time, just the large width of $f_2(2000)$ is an argument in favor of the glueball origin of this resonance. However, to prove the glueball nature of $f_2(1200)$, the measurement of the decay constants and their comparison to the ratios given in the table is needed.

I am grateful to L.G. Dakhno, S.S. Gershtein, V.A. Nikonov, and A.V. Sarantsev for stimulating discussions, comments, and help. This paper was supported by the Russian Foundation for Basic Research (project no. 04-02-17091).

REFERENCES

1. V. A. Schegelsky, A. V. Sarantsev, and V. A. Nikonov, L3 Note 3001 (2004).
2. R. S. Longacre and S. J. Lindenbaum, Report BNL-72371-2004.
3. A. Etkin *et al.*, Phys. Lett. B **165B**, 217 (1985); **201**, 568 (1988).
4. A. V. Anisovich, V. V. Anisovich, and A. V. Sarantsev, Phys. Rev. D **62**, 051502 (2000).
5. V. V. Anisovich, M. N. Kobrinsky, J. Nyiri, and Yu. M. Shabelski, *Quark Model and High Energy Collisions*, 2nd ed. (World Sci., Singapore, 2004).
6. V. V. Anisovich, Usp. Fiz. Nauk **174**, 49 (2004) [Phys. Usp. **47**, 45 (2004)].
7. D. Barberis *et al.* (WA 102 Collab.), Phys. Lett. B **471**, 440 (2000).
8. A. V. Anisovich *et al.*, Phys. Lett. B **491**, 47 (2000).
9. S. Eidelman *et al.* (PDG), Phys. Lett. B **592**, 1 (2004).
10. A. V. Anisovich, V. V. Anisovich, M. A. Matveev, and V. A. Nikonov, Yad. Fiz. **66**, 946 (2003) [Phys. At. Nucl. **66**, 914 (2003)].
11. A. V. Anisovich, V. V. Anisovich, and V. A. Nikonov, Eur. Phys. J. A **12**, 103 (2001).
12. E. Aker *et al.* (Crystall Barrel Collab.), Phys. Lett. B **260**, 249 (1991).
13. A. Adamo *et al.* (OBELIX Collab.), Phys. Lett. B **287**, 368 (1992); Nucl. Phys. A **558**, 13C (1993).
14. A. Bertin *et al.* (OBELIX Collab.), Phys. Lett. B **408**, 476 (1997).
15. T. A. Armstrong *et al.* (E760 Collab.), Phys. Lett. B **307**, 394 (1993); **307**, 399 (1993).
16. V. V. Anisovich, D. S. Armstrong, I. Augustin, *et al.* (Crystal Barrel Collab.), Phys. Lett. B **323**, 233 (1994).
17. V. V. Anisovich, D. V. Bugg, A. V. Sarantsev, and B. S. Zou, Phys. Rev. D **50**, 1972 (1994).
18. A. V. Anisovich, V. A. Nikonov, A. V. Sarantsev, and V. V. Sarantsev, in *Proceedings of PNPI XXX: Scientific Highlight, Theoretical Physics Division* (Gatchina, 2001), p. 58.
19. D. V. Bugg *et al.*, Phys. Lett. B **353**, 378 (1995).
20. G. M. Beladidze *et al.* (VES Collab.), Z. Phys. C **54**, 367 (1992).
21. D. M. Alde *et al.* (GAMS Collab.), Phys. Lett. B **241**, 600 (1990).
22. D. Barberis *et al.* (WA 102 Collab.), Phys. Lett. B **484**, 198 (2000).
23. D. M. Alde *et al.* (GAMS Collab.), Phys. Lett. B **276**, 375 (1992).
24. D. Barberis *et al.* (WA 102 Collab.), Phys. Lett. B **471**, 429 (2000).
25. D. Barberis *et al.* (WA 102 Collab.), Phys. Lett. A **479**, 59 (2000).
26. A. V. Singovsky, Nuovo Cimento A **107**, 1911 (1994).
27. A. V. Anisovich *et al.*, Phys. Lett. B **468**, 309 (1999).
28. D. Barberis *et al.* (WA 102 Collab.), Phys. Lett. B **453**, 305 (1999).
29. K. Abe *et al.* (BELLE Collab.), Eur. Phys. J. C **32**, 323 (2004).
30. G. S. Bali, K. Schilling, A. Hulsebos, *et al.* (UK QCD Collab.), Phys. Lett. B **309**, 378 (1993); C. J. Morningstar and M. J. Peardun, Phys. Rev. D **60**, 034 509 (1999).
31. V. V. Anisovich, D. V. Bugg, and A. V. Sarantsev, Phys. Rev. D **58**, 111 503 (1998).

32. V. V. Anisovich, Yu. D. Prokoshkin, and A. V. Sarantsev, Phys. Lett. B **389**, 388 (1996).
33. V. V. Anisovich, Yu. D. Prokoshkin, and A. V. Sarantsev, Z. Phys. A **357**, 123 (1997).
34. A. V. Anisovich, V. V. Anisovich, and A. V. Sarantsev, Phys. Lett. B **395**, 123 (1997).
35. A. V. Anisovich, V. V. Anisovich, and A. V. Sarantsev, Z. Phys. A **359**, 173 (1997).
36. V. V. Anisovich and A. V. Sarantsev, Eur. Phys. J. A **16**, 229 (2003).
37. K. Peters and E. Klempt, Phys. Lett. B **352**, 467 (1995).
38. G. t'Hooft, Nucl. Phys. B **72**, 461 (1974); G. Veneziano, Nucl. Phys. B **117**, 519 (1976).
39. V. V. Anisovich, A. A. Kondashov, Yu. D. Prokoshkin, *et al.*, Yad. Fiz. **63**, 1489 (2000) [Phys. At. Nucl. **63**, 1410 (2000)].
40. M. Doser, Phys. Lett. B **592**, 594 (2004).
41. J. Sexton, A. Vaccarino, and D. Weingarten, Phys. Rev. Lett. **75**, 4563 (1995); W. Lee and D. Weingarten, Phys. Rev. D **61**, 014015 (2000).
42. I. S. Shapiro, Nucl. Phys. A **122**, 645 (1968).
43. I. Yu. Kobzarev, N. N. Nikolaev, and L. B. Okun, Yad. Fiz. **10**, 864 (1969) [Sov. J. Nucl. Phys. **10**, 499 (1969)].
44. L. Stodolsky, Phys. Rev. D **1**, 2683 (1970).

JETP Letters, Vol. 80, No. 12, 2004, pp. 721–724. Translated from Pis'ma v Zhurnal Éksperimental'noĭ i Teoreticheskoĭ Fiziki, Vol. 80, No. 12, 2004, pp. 850–854.

Refraction of Autowaves: Tangent Rule

O. A. Mornev

Institute of Theoretical and Experimental Biophysics, Russian Academy of Sciences, Pushchino, Moscow region, 142292 Russia

e-mail: mornev@mail.ru

Received July 27, 2004; in final form, November 9, 2004

The refraction of autowaves at the interface between homogeneous regions of a reaction–diffusion medium with different diffusion coefficients obeys the tangent rule. © *2004 MAIK "Nauka/Interperiodica".*

PACS numbers: 05.45.–a; 82.40.Ck; 87.10.+e

Nonlinear self-sustained waves (autowaves) propagating in active reaction–diffusion media specifically differ from waves in conservative media [1–3]. One of these differences concerns the refraction law, i.e., a rule that relates the directions of the propagation of a wave front on both sides of the interface between homogeneous regions of a medium. In this work, it has been shown that, if the diffusion properties of the homogeneous regions are different and the active properties are identical, autowaves are refracted according to the tangent rule (see below) rather than the sine rule, which expresses the known Snell's law for optical refraction.

Let us consider piecewise homogeneous active media, where the state of homogeneous regions evolves according to the continuity equation

$$u_t + \mathrm{div}\mathbf{J} = f(u) \tag{1}$$

and the phenomenological linear diffusion law (Fick's law)

$$\mathbf{J} = -D\nabla u. \tag{2}$$

Here, $u = u(\mathbf{r}, t)$ is the density of the reagent (activator) filling the medium at the point $\mathbf{r} \equiv \{x, y, z\}$ at time t, $u_t \equiv \partial u/\partial t$; the activator-production rate $f(u)$ per unit volume as a function of the density u is continuous and has the same form over the entire medium; $\mathbf{J}$ is the diffusion flux density of the activator; the activator diffusion coefficient D is constant in each homogeneous region but changes stepwise at the interfaces between the homogeneous regions; and div and $\nabla \equiv$ grad are the spatial divergence and gradient operators, respectively.

In homogeneous regions, an evolving autowave is represented by a family of fronts, i.e., isoconcentration surfaces $u(\mathbf{r}, t) = \mathrm{const} \equiv u_\mathrm{F}$, where u_F is the density at a front and $u(\mathbf{r}, t)$ is the solution of the reaction–diffusion equation

$$u_t = D\Delta u + f(u) \quad (\Delta \equiv \mathrm{divgrad}), \tag{3}$$

which is obtained by substituting Eq. (2) into Eq. (1). Equation (3) describes, e.g., the diffusion of genes in biological populations [4, 5], temperature and/or density autowaves in combustible and other autocatalytic media [6, 7], autowaves of boiling-regime changes in coolers [8], autowaves of resistance rearrangements in normal metals and superconductors [9], and the leading fronts of excitation pulses in electrically excitable biological media [10].

On surfaces separating homogeneous regions, solutions of Eq. (3) must be joined according to certain joining rules. However, for any such rule, the density fronts must obviously be refracted on these surfaces, because the velocities $\mathbf{v}_D = u^{-1}\mathbf{J} = -Du^{-1}\nabla u$ of the diffusion transport of the activator are different in regions with different D values.

It is convenient to describe refraction phenomena by the concept of rays that is dual to the concept of fronts. Rays are curves orthogonal to the one-parameter family of isochronic fronts that is separated from the two-parameter family $u(\mathbf{r}, t) = u_\mathrm{F}$ by fixing t. In other words, rays are integral curves of the vector field of the gradient of the density u at a given t value. A tangent to a ray at the point $\mathbf{r}$ is determined by any vector collinear to the vector $\nabla u(\mathbf{r}, t)$, in particular, by this vector itself and the diffusion flux vector $\mathbf{J}(\mathbf{r}, t) = -D\nabla u(\mathbf{r}, t)$. Let regions *1* and *2* be two neighboring regions where the diffusion coefficients are D_1 and D_2, respectively, and which are separated by the surface Π, which is ideally permeable for diffusion fluxes. Similar to optics, a smooth ray intersecting the surface Π at a certain point $O \in \Pi$ is bent at this point; i.e., two smooth components of the ray, one of which is located in region *1* and the other in region *2*, have two different limiting tangents at the point O. These tangents are determined by the tangent vectors $(\nabla u)_1$ and $(\nabla u)_2$ that are obtained from ∇u by unilateral limiting transitions at the point O along the smooth components of the ray in regions *1* and *2*, respectively. The relation between the directions of the aforementioned tangents s specifies the refraction law for the autowave. We aim to determine this law.

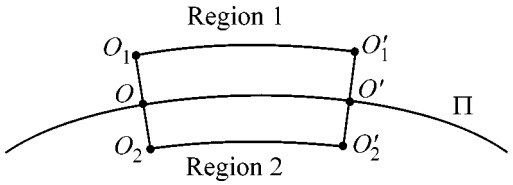

Fig. 1. Illustration of the derivation of boundary condition (4). See the explanation in the main body of the text.

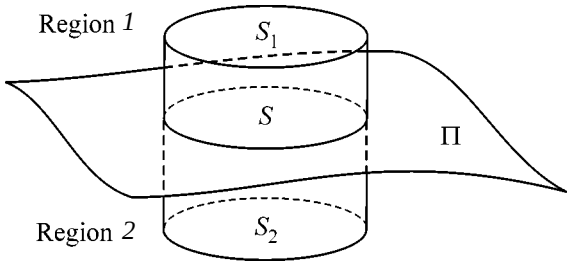

Fig. 2. Illustration of the derivation of boundary condition (6). See the explanation in the main body of the text.

To find the refraction law, it is obviously sufficient to reveal the relation between the tangent vectors $(\nabla u)_1$ and $(\nabla u)_2$ of the ray at the point O. This may be done using two general reasons: the requirement of the continuity of the density field u on the surface Π and the integral continuity equation describing the activator balance in the medium.[1]

Accepting the requirement of the continuity of the field u on the surface Π, we consider the contour $O_1O_1'O_2'O_2$ shown in Fig. 1. Owing to the continuity, the u values at the points O_1 and O_1' in region *1* are close to the u values at the respective points O_2 and O_2' in region *2*. Therefore, the difference $u(O_1', t) - u(O_1, t)$ is close to the difference $u(O_2', t) - u(O_2, t)$. Correspondingly, the spatial derivatives of u calculated at the points O_1 and O_2 along the directions tangent to the arcs O_1O_1' and O_2O_2' are close to each other. In the limit where the contour shown in Fig. 1 is contracted to the arc $OO' \subset \Pi$, we arrive at the boundary condition

$$(\partial u/\partial\tau)_1 = (\partial u/\partial\tau)_2 \Leftrightarrow (\nabla u)_1 \cdot \boldsymbol{\tau} = (\nabla u)_2 \cdot \boldsymbol{\tau}. \quad (4)$$

Here, $\partial/\partial\tau = \boldsymbol{\tau} \cdot \nabla$ is the derivative operator along the unit vector $\boldsymbol{\tau}$ tangent to the surface Π at the point O and, as above, subscripts *1* and *2* stand for the unilateral limits of the quantities on the surface Π. Condition (4) is valid at any point $O \in \Pi$ for any $\boldsymbol{\tau}$ and means that the projection of the vector ∇u onto any direction tangent to the surface Π at the point of the intersection of the surface Π varies continuously. At the same time, the tangent projection of the vector $\mathbf{J} = -D\nabla u$ is discontinuous as is seen from the equality $D_1^{-1}\boldsymbol{\tau} \cdot \mathbf{J}_1 = D_2^{-1}\boldsymbol{\tau} \cdot \mathbf{J}_2$, which is equivalent to Eq. (4).

To obtain a boundary condition relating the normal projections of the vectors $(\nabla u)_1$ and $(\nabla u)_2$ on the surface Π, we consider the integral continuity equation

$$\frac{\partial}{\partial t}\int_V u dV + \oint_{\partial V} \mathbf{J} d\mathbf{S} = \int_V f(u) dV. \quad (5)$$

Describing the activator balance in an arbitrary closed spatial region V bounded by the surface ∂V, this integral equation is more general than differential continuity equation (1): indeed, Eq. (5) is valid not only in homogeneous regions, where it evidently reduces to Eq. (1), but also at the interface Π between these regions, where Eq. (1) does not hold. On the surface Π, Eq. (5) degenerates into the desired boundary condition, which can be found in the standard way: by applying Eq. (5) to the cylinder that has the bases S_1 and S_2 and cuts an arbitrary area S on the surface Π (see Fig. 2). When the cylinder is contracted by converging its bases S_1 and S_2 to $S \subset \Pi$, the volume integrals and integral over the lateral surface of the cylinder in Eq. (5) vanish and Eq. (5) takes the form

$$\oint_S (\mathbf{J}_1 - \mathbf{J}_2) \cdot \mathbf{n} dS$$
$$\equiv -\oint_S [D_1(\nabla u)_1 - D_2(\nabla u)_2] \cdot \mathbf{n} dS = 0.$$

Here, $\mathbf{n}$ is the unit vector that is normal to S and directed towards region *1*. Since the area S is chosen arbitrarily, the latter equality is equivalent to the boundary condition

$$D_1(\nabla u)_1 \cdot \mathbf{n} = D_2(\nabla u)_2 \cdot \mathbf{n}. \quad (6)$$

In particular, according to this condition, the projection of the vector ∇u onto the direction normal to the surface Π is discontinuous on this surface. At the same time, the normal projection of the vector $\mathbf{J}$ is continuous onto this surface. Indeed, Eq. (6) is equivalent to the equality $\mathbf{n}\mathbf{J}_1 = \mathbf{n}\mathbf{J}_2$.

Boundary conditions (4) and (6) determine the relation between the directions of the vectors $(\nabla u)_1$ and $(\nabla u)_2$ at the points of the surface Π, i.e., the refraction law. This law is determined in two steps.

First, let us show that three vectors $(\nabla u)_1$, $\mathbf{n}$, and $(\nabla u)_2$, which have the common beginning at the point

[1] The requirement of the continuity of the field u on the surface Π is justified as follows. A stepwise change in the diffusion coefficient D when passing through the surface Π simulates the real physical case where D continuously changes between the values D_1 and D_2 in a spatial layer of small nonzero width δ that is adjacent to the surface Π from both sides. In this case, the field u is continuous and must remain continuous in the limit $\delta \longrightarrow 0$. Otherwise, the surface-jump model for D is inadequate for the physical case.

$O \in \Pi$, are located in one plane (refraction plane). This can be proved via the decomposition $(\nabla u)_i = \mathbf{N}_i + \mathbf{T}_i$ ($i = 1, 2$), where $\mathbf{N}_i$ and $\mathbf{T}_i$ are the normal and tangential components of the vectors $(\nabla u)_i$ to the surface Π at the point O. Since $\mathbf{N}_1$ and $\mathbf{N}_2$ belong to the straight line extended along the normal $\mathbf{n}$, the vectors $(\nabla u)_1$ and $(\nabla u)_2$ lie in planes spanned by the vector pairs $\{\mathbf{n}, \mathbf{T}_1\}$ and $\{\mathbf{n}, \mathbf{T}_2\}$, respectively. Using the decomposition indicates above, one can rewrite boundary condition (4) in the form $(\mathbf{T}_1 - \mathbf{T}_2) \cdot \boldsymbol{\tau} = 0$, which is valid for any vector $\boldsymbol{\tau}$ tangent to the surface Π at the point $O \in \Pi$. Consequently, $\mathbf{T}_1 = \mathbf{T}_2$ and the planes $\{\mathbf{n}, \mathbf{T}_1\}$ and $\{\mathbf{n}, \mathbf{T}_2\}$ coincide with each other and form the refraction plane containing the three vectors $\mathbf{n}$, $(\nabla u)_1$, and $(\nabla u)_2$.

Let us consider the refraction plane (the *R* plane in Fig. 3), which contains the normal $\mathbf{n}$ to the surface Π at the point *O* of the ray refraction. We introduce the orthogonal coordinate system *Oxy* on the plane *R* whose *Ox* axis is directed along the unit vector $\boldsymbol{\tau}$ tangent to the surface Π at the point *O* and the *Oy* axis is directed along the vector $\mathbf{n}$ (Fig. 3). According to the above consideration, the plane *R* contains the vectors $(\nabla u)_1$ and $(\nabla u)_2$. It follows from Eq. (4) that the projections of these vectors onto the *Ox* axis have the same sign. It follows from Eq. (6) that the signs of the projections of these vectors onto the *Oy* axis are also identical. Therefore, the vectors $(\nabla u)_1$ and $(\nabla u)_2$ are placed in the same quadrant of the plane *R*. Without the restriction of generality, we may consider that it is the IV quadrant of the plane *R* (Fig. 3). Indeed, this can be made by the appropriate rotations of the coordinate system about $\boldsymbol{\tau}$ and $\mathbf{n}$ and/or permutation of the numbers of homogeneous regions *1* and *2*. The angles φ_1 and φ_2 between the vectors $(\nabla u)_1$ and $(\nabla u)_2$, respectively, and the *Oy* axis are related to the angles ψ_1 and ψ_2 between the vectors $(\nabla u)_1$ and $(\nabla u)_2$, respectively, and the *Ox* axis as $\psi_i = \varphi_i - 3\pi/2$ ($i = 1$ and 2). It is easily seen in Fig. 3 that

$$\begin{aligned} \tan\psi_1 &= ((\nabla u)_1 \cdot \boldsymbol{\tau})/|(\nabla u)_1 \cdot \mathbf{n}|, \\ \tan\psi_2 &= ((\nabla u)_2 \cdot \boldsymbol{\tau})/|(\nabla u)_2 \cdot \mathbf{n}|. \end{aligned} \tag{7}$$

According to these relations and Eqs. (4) and (6), the desired refraction law (tangent rule) has the form

$$\tan\psi_1/\tan\psi_2 = \text{const} \equiv D_1/D_2. \tag{8}$$

We emphasize that this law is local: it describes refraction near the surface Π rather than far from it. Therefore, Eq. (8) is valid even when the coefficient *D* is not constant in regions *1* and *2* but varies smoothly from point to point and changes stepwise between the local values D_1 and D_2 on the surface.

Tangent rule (8) is applicable to both the unsteady evolution of a refracting autowave and the steady refraction regime, when the geometry of fronts and rays ceases to change. In the latter case, the tangent rule is consistent with the results obtained in [11] and makes it possible to independently reproduce them by additional analysis.

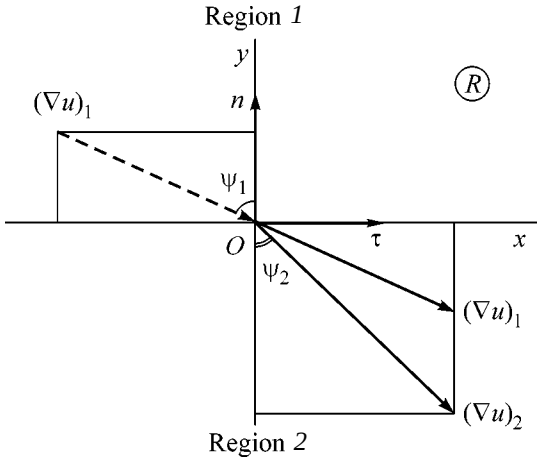

Fig. 3. Position of the vectors $(\nabla u)_1$ and $(\nabla u)_2$ in the refraction plane *R*.

Taking into account the relation $c = c_s D^{1/2}$,[2] where *c* is the steady velocity of the plane autowave in the infinite homogeneous medium with the diffusion coefficient *D* and c_s is the dimensional constant independent of *D*, one can obtain the following representation of formula (8):

$$\tan\psi_1/\tan\psi_2 = \text{const} \equiv c_1^2/c_2^2. \tag{9}$$

Here, c_1 and c_2 are the values of the steady velocity *c* at $D = D_1$ and D_2, respectively.

According to the tangent rule, the rays and fronts are bent on the surfaces of the jumps of the diffusion coefficient. Since this rule is a direct consequence of the general physical laws, these kinks can be eliminated neither by diffusion nor by special dynamic effects accompanying the propagation of autowaves, contrary to the opinion of the authors of [12]. Moreover, exact formula (9) does not corroborate certain results of the approximate analysis performed in [13], where the case of negligibly small diffusion was considered.

The properties presented above concern active media satisfying Eqs. (1) and (2). Let us briefly discuss the case of multicomponent active media that contain several reagents (components)—activators and depressors—and are described by pairs of relations of form (1) and (2) (the number of pairs is equal to the number of components). In these cases, tangent rule (8) is valid for each of the refracted diffusible components. For these cases, D_1 and D_2 entering into Eq. (8) are associ-

[2] This relation follows from the scale properties of Eq. (3). The c_s value equal to the velocity of a steadily propagating plane autowave for $D = 1$ is determined only by the form of the kinetic function $f(u)$ entering into Eqs. (1) and (3) and the system of physical units.

ated with the refracting component for which this relation is written.

In contrast to refraction law (8), representation (9) of this law loses sense for media with several diffusible components, because the relation $c = c_s D^{1/2}$ in such media is not generally valid. However, if only one component diffuses in a multicomponent medium, this relation is valid for this component. Therefore, the refraction of this component satisfies both relations (8) and (9). Biological electrically excitable media [10] such as a nerve fiber and heart present important examples of multicomponent active media with one diffusible component. In such media, the excitation is transferred from cell to cell due to the electrodiffusion of the excitation activator—alkali-metal ions—through the intercellular electrolytes and intercellular contacts. The electrodiffusion coefficient of the ions linearly depends on the electrical conductivity of the intercellular contacts. Therefore, in the regions of sharp change in this parameter, an excitation autowave detected by a change in the difference of the electrical potentials on the cellular membranes must be refracted according to Eqs. (8) and (9).

The statement that the tangent rule is valid for the refraction of autowaves in multicomponent media is associated with the ordinary annihilation regime, where colliding autowaves are damped without the generation of reflected waves, which are not taken into account in the above analysis. The laws of the refraction of autowaves under the conditions allowing reflection [14] require individual analysis.

In summary, we note that the derivation of tangent rule (8) is independent of the form of the kinetic function $f(u)$ entering into Eqs. (1), (3), and (5). Therefore, the refraction law for density and/or temperature fronts, which is expressed by this rule, is valid even for inhomogeneous media without autocatalysis, where substances and/or heat diffuse and possibly interact with each other, but autowaves do not propagate. However, representation (9) of the refraction law in such media is meaningless, because the values c_1 and c_2 entering into Eq. (9) are determined by the kinetic function via the solution of the problem of the steady motion of a plane autowave.

In all the cases under consideration, the tangent rule can directly be verified experimentally.

I am grateful to E.E. Shnol for stimulating discussions and remarks. This work was supported by the Russian Foundation for Basic Research, project no. 02-01-00626.

REFERENCES

1. V. A. Vasil'ev, Yu. M. Romanovskiĭ, and V. G. Yakhno, Usp. Fiz. Nauk **128**, 625 (1979) [Sov. Phys. Usp. **22**, 615 (1979)].
2. V. I. Krinskiĭ and A. S. Mikhaĭlov, *Autowaves* (Znanie, Moscow, 1984) [in Russian].
3. V. A. Vasil'ev, Yu. M. Romanovskiĭ, and V. G. Yakhno, *Autowave Processes* (Nauka, Moscow, 1987) [in Russian].
4. A. N. Kolmogorov, I. G. Petrovskiĭ, and N. S. Piskunov, Byull. Mosk. Univ., Ser. 4: Mat. Mekh. **1**, 1 (1937).
5. R. A. Fischer, Ann. Eugen. **7**, 355 (1937).
6. Ya. B. Zeldovich and D. A. Frank-Kamenetskiĭ, Dokl. Akad. Nauk SSSR **19**, 693 (1938).
7. D. A. Frank-Kamenetskiĭ, *Diffuison and Heat Transfer in Chemical Kinetics* (Nauka, Moscow, 1967; Plenum, New York, 1969).
8. S. A. Zhukov, V. V. Barelko, and A. G. Merzhanov, Int. J. Heat Mass Transf. **24**, 47 (1980).
9. A. Vl. Gurevich and R. G. Mints, Usp. Fiz. Nauk **142**, 61 (1984) [Sov. Phys. Usp. **27**, 19 (1984)].
10. A. C. Scott, Rev. Mod. Phys. **47**, 487 (1975); *Neuroscience: A Mathematical Primer* (Springer, New York, 2002); *Nonlinear Science: Emergence and Dynamics of Coherent Structures*, 2nd ed. (Oxford Univ. Press, Oxford, 2003).
11. O. A. Mornev, in *Self-Organization: Autowaves and Structures Far from Equilibrium*, Ed. by V. I. Krinsky (Springer, Berlin, 1984), p. 111.
12. P. K. Brazhnik and J. J. Tyson, Phys. Rev. E **54**, 1958 (1996).
13. C. Matsuoka *et al.*, Phys. Lett. A **243**, 47 (1998).
14. O. A. Mornev, O. V. Aslanidi, and I. M. Tsyganov, Macromol. Symp. **160**, 115 (2000).

Translated by R. Tyapaev

JETP Letters, Vol. 80, No. 12, 2004, pp. 725–729. From Pis'ma v Zhurnal Éksperimental'noĭ i Teoreticheskoĭ Fiziki, Vol. 80, No. 12, 2004, pp. 855–859.

Statistics of Impedance, Local Density of States, and Reflection in Quantum Chaotic Systems with Absorption¶

Y. V. Fyodorov[1, 2] and D. V. Savin[3]

[1] *Department of Mathematical Sciences, Brunel University, Uxbridge, UB8 3PH, United Kingdom*

[2] *St. Petersburg Nuclear Physics Institute, Russian Academy of Sciences, Gatchina, 188300 Russia*

[3] *Fachbereich Physik, Universität Duisburg–Essen, 45117 Essen, Germany*

Received November 11, 2004

We are interested in finding the joint distribution function of the real and imaginary parts of the local Green's function for a system with chaotic internal wave scattering and a uniform energy loss (absorption). For a microwave cavity attached to a single-mode antenna, the same quantity has a meaning of the complex cavity impedance. Using the random matrix approach, we relate its statistics to that of the reflection coefficient and scattering phase and provide exact distributions for systems with the $\beta = 2$ and $\beta = 4$ symmetry class. In the case of $\beta = 1$, we provide an interpolation formula that incorporates all the known limiting cases and excellently fits the available experimental data as well as diverse numeric tests. © *2004 MAIK "Nauka/Interperiodica".*

PACS numbers: 05.45.Mt; 42.25.Bs; 73.23.–b

Characterizing statistical fluctuations of physical observables in quantum systems with underlying chaotic classical dynamics remains a very active field of research in theoretical and experimental physics. Considerable progress in understanding the phenomenon was underpinned by revealing the apparent universality of the fluctuations in systems of very diverse microscopic nature, ranging from atomic nuclei and Rydberg atoms in strong external fields to complex molecules, quantum dots, and mesoscopic samples (see, e.g., [1]). From the theoretical side, the universality allows one to exploit the random matrix theory (RMT) as a powerful tool for analysis of the generic features of the energy spectra of such systems [2, 3].

In many atomic, molecular, and mesoscopic systems, the quantity that is readily obtained experimentally is the absorption spectrum for transitions from a given initial state $|g\rangle$ to highly excited chaotic states at the energy E. For high-resolution experiments, chaotic spectra consist of well-resolved narrow resonance peaks, and one can, in principle, study the statistics of the peak heights and widths, as well as that of the spacings between consecutive peaks. Most frequently, however, the absorption spectra look practically continuous due to both the inevitable level broadening and finite experimental resolution. Then, the relevant statistics are the distribution and correlation functions of the absorption probability $\sigma(E)$ (also known as the strength function of the dipole operator $\hat{\mu}$), which, in the simplest situation of uniform level broadening Γ, is given by $\sigma(E) \propto \mathrm{Im}\langle g|\hat{\mu}\hat{G}(E)\hat{\mu}|g\rangle$ (see, e.g., [4] and the discussion therein). Assuming the validity of the RMT, the problem then amounts to studying the statistical properties of the resolvent (Green's function) operator $\hat{G}(E) \equiv (E + i\Gamma/2 - \hat{H})^{-1}$ associated with the random matrix $\hat{H}$, which replaces the actual chaotic Hamiltonian. In particular, the imaginary part of the diagonal entries of $\hat{G}(E)$ is well known in solid-state physics as the local density of states (LDoS), and, in this capacity, its statistics have been much studied [4–8].

From the experimental point of view, the same universality that makes the use of the RMT legitimate provides one with an attractive possibility to employ simple model systems for analyzing the generic statistics of the fluctuating quantities. One of such systems, which proved to be an ideal medium for investigating a variety of quantum chaos phenomena, is various microwave billiards [1]. The billiards are realized as resonators in a form of electromagnetic cavities shaped to ensure the chaoticity of internal scattering and coupled to transmission lines or to waveguides. An adequate description is then achieved in terms of the scattering matrix S relating the amplitudes of the incoming and outgoing waves. High-resolution experiments are usually performed in low-temperature (superconducting) cavities with a very high quality factor [9]. The majority of the experiments are, however, done at room temperature [10–13]. The inevitable energy losses (absorption) leading to uniform broadening of the resonances therefore play an important role and have to be taken into account properly when describing the experiments theoretically.

Various statistics related to the scattering matrix of chaotic systems with losses were the subject of a number of recent papers [14–19]. Explicit analytical results

¶ This article was submitted by the authors in English.

were available, however, only for the simplest case of systems with no time-reversal invariance (TRI) corresponding to the so-called $\beta = 2$ symmetry class of the RMT. At the same time, the majority of the billiard-type experiments are performed in systems which are time-reversal invariant ($\beta = 1$ symmetry class of the RMT). A similar situation holds for the statistics of the local Green's function, in particular, for the LDoS. For the $\beta = 2$ case, the corresponding expressions were obtained by various methods in [5–7, 20]. An attempt [8] to provide an expression for the LDoS distribution for the $\beta = 1$ case cannot be considered as particularly successful, as the general expression was given in the form of an intractable fivefold integral. Finally, it is worth mentioning the existence of the $\beta = 4$ symmetry class describing time-reversal invariant chaotic systems with half-integer spin. This situation may occur in quantum dots with strong spin–orbit scattering [21]and in Rydberg atoms driven by microwave fields [22] and can be efficiently simulated in some other models of quantum chaotic systems [23].

Here, we are going to concentrate on the simplest case of a single one-channel antenna experiment. To be able to employ the RMT methods, it is conventional to represent the resonant part of the S matrix in the following form (see, e.g., [24]):

$$S(E) = \frac{1 - iK(E)}{1 + iK(E)} = \sqrt{r}e^{i\theta}, \qquad (1)$$

where $K(E) = V^{\dagger}\hat{G}(E)V$ is the so-called K matrix. The Hamiltonian $\hat{H}$ of the closed chaotic cavity gives rise to N eigenfrequencies E_n characterized in the relevant range of the scattering energy E by the mean level spacing Δ. The column-vector V describes the energy-independent amplitudes coupling the corresponding eigenmodes to the propagating mode in the antenna. We again see that the study of the statistical properties of the scattering matrix amounts to knowing the statistics of the diagonal element G_{11} of the Green's function of the closed system in some basis. In fact, in the present context, the function $iK \equiv Z$ has the direct physical meaning of the electric impedance Z of the cavity, which linearly relates the voltages and currents at the antenna port [11].

Without absorption, $\Gamma = 0$ and the scattering matrix is unimodular: $r \equiv 1$. At finite absorption, when $\Gamma > 0$, the reflection coefficient r and the scattering phase θ have nontrivial distributions, which have been recently measured in experiments [10, 13]. On the other hand, universal fluctuations of both the real and imaginary parts of the cavity impedance Z have been recently investigated experimentally in [11]. Since the impedance matrix Z is related to the eigenmodes and eigenfrequencies of the closed cavity, the study of Z is in some sense complementary to that of S.

The fundamental quantity that determines the full statistics of S or Z is the joint distribution function $\mathcal{P}(u, v)$ of the real $u = \mathrm{Re}K$ and imaginary $v = -\mathrm{Im}K > 0$ parts of K. Generally, one can always write $K = \kappa(N\Delta/\pi)G_{11}$ in the RMT. The effective coupling constant $\kappa = \pi\|V\|^2/N\Delta > 0$ enters the S matrix statistics only through the so-called transmission coefficient $T \equiv 1 - |\bar{S}|^2$ ($=4\kappa/(1+\kappa)^2$ in the middle of the spectrum, $E = 0$) (see, e.g., [24, 25] for details).

A convenient starting point of our analysis is the observation that, in the case of the so-called "perfect coupling," $T = 1$, the distribution $\mathcal{P}(u, v)$ must always have the following general form:

$$\mathcal{P}(u, v) = \frac{1}{2\pi v^2}P_0(x), \qquad (2)$$

with $x = (u^2 + v^2 + 1)/2v > 1$. It initially emerged in [26] in the course of explicit calculations for the $\beta = 2$ symmetry class, but neither the origin nor the generality of such a form were appreciated. Here, we show that Eq. (2) is the direct consequence of two fundamental properties of the case considered: (i) the statistical independence of the S matrix modulus $r \equiv (x-1)/(x+1)$ and its phase θ; and (ii) the uniform distribution of $\theta \in (0, 2\pi)$. Both these properties can be verified using the methods of [27]. The joint distribution $P(x, \theta)$ then factorizes to $P_0(x)/2\pi$. Choose now the new variable $y \equiv \mathrm{Re}S/\mathrm{Im}S = \cot(\theta)$ instead of θ so that $|d\theta/dy| = (1 + y^2)^{-1}$. Noticing that $y = (u^2 + v^2 - 1)/2u$, and, evaluating the corresponding Jacobian $|\partial(x, y)/\partial(u, v)| = (1 + y^2)/v^2$ of the transformation from x and y to u and v, we come, after a simple calculation, to (2).

The explicit form of $P_0(x)$ at arbitrary absorption for various symmetry classes will be given and discussed below. Having $P_0(x)$ at our disposal, it is easy to find the distribution of the imaginary part v (the LDoS is normalized for convenience to have the unit mean value):

$$\mathcal{P}_v(v) = \frac{\sqrt{2}}{\pi v^{3/2}}\int_0^{\infty} dq P_0\left[q^2 + \frac{1}{2}\left(v + \frac{1}{v}\right)\right]. \qquad (3)$$

The distribution is normalized to 1 and has the first moment unity, $\langle v\rangle \equiv \int_0^{\infty} dv\, v\mathcal{P}(v) = 1$, automatically due to the invariance of the integrand with respect to the change $v \longrightarrow 1/v$. Similarly, one can find the distribution of the real part u to be

$$\mathcal{P}_u(u) = \frac{1}{2\pi\sqrt{u^2+1}}\int_0^{\infty} dq P_0\left[\frac{\sqrt{u^2+1}}{2}\left(q + \frac{1}{q}\right)\right]. \qquad (4)$$

Although u has no direct physical meaning in the context of solid-state mesoscopic systems, both $\mathcal{P}_u(u)$ and $\mathcal{P}_v(v)$ are directly measurable in microwave cavities [11].

Let us now discuss the explicit forms of $P_0(x)$ for various symmetry classes: $\beta = 1, 2, 4$. For the simplest

case of broken TRI ($\beta = 2$), an exact result is available at arbitrary values of the dimensionless absorption strength $\gamma \equiv 2\pi\Gamma/\Delta$ [16–18]. Scaling the absorption parameter for subsequent use as $\alpha \equiv \gamma\beta/2$, we can represent the $\beta = 2$ result as follows:

$$P_0(x) = \frac{\mathcal{N}_\beta}{2}[A(\alpha(x+1)/2)^{\beta/2} + B]e^{-\alpha(x+1)/2}, \quad (5)$$

with the α-dependent constants $A \equiv e^\alpha - 1$ and $B \equiv 1 + \alpha - e^\alpha$ and the normalization constant $\mathcal{N}_2 = 1$.

For the case $\beta = 4$, the exact form became available very recently [28] by exploiting important advances in the RMT [29]. The explicit derivation will be given elsewhere, the final result being [28]:

$$P_0^{\mathrm{gse}}(x) = \tilde{P}_0^{\mathrm{gue}}(x) + C(x,\gamma)e^{-\gamma x}\int_0^\gamma dt\frac{\sinh t}{t}, \quad (6)$$

where $\tilde{P}_0^{\mathrm{gue}}(x)$ is the distribution (5) for $\beta = 2$ taken, however, at $\alpha = 2\gamma$ and $C(x, \gamma) \equiv \gamma^2(x+1)^2/2 - \gamma(\gamma+1)(x+1) + \gamma$.

Unfortunately, for the most interesting case $\beta = 1$, the explicit formula for $P_0(x)$ is not available yet, apart from the limiting cases of weak or strong absorption:

$$P_0(x) \simeq \begin{cases} \dfrac{\alpha^{\beta/2+1}}{2\Gamma(\beta/2+1)}\left(\dfrac{x+1}{2}\right)^{\beta/2}e^{-\alpha(x+1)/2}, & \gamma \ll 1 \\ (\alpha/2)e^{-\alpha(x-1)/2}, & \gamma \gg 1. \end{cases} \quad (7)$$

The first line here results from the following relation [14, 16]: $2/(x+1) = 1 - r \approx \gamma\tau$ at $\gamma \ll 1$ between the reflection coefficient and the (dimensionless) time-delay τ and the known time-delay distribution [24, 30] for all $\beta = 1, 2, 4$: $\mathcal{P}_\tau(\tau) = [(\beta/2)^{\beta/2}/\Gamma(\beta/2)]\tau^{-\beta/2-2}e^{-\beta/2\tau}$. In the opposite case $\gamma \gg 1$, the known limiting Rayleigh distribution [15] $P(r) \simeq (\gamma\beta/2)e^{-r\gamma\beta/2}$ yields the second line in Eq. (7).

In the absence of a general expression for $\beta = 1$, the natural idea is to try to invent a formula that interpolates between the known limiting cases [13]. We suggest Eq. (5) to be the appropriate natural candidate with the normalization constant being $\mathcal{N}_\beta = \alpha/(A\Gamma(\beta/2+1, \alpha) + Be^{-\alpha})$, where $\Gamma(\nu, \alpha) = \int_\alpha^\infty dt\, t^{\nu-1}e^{-t}$. Indeed, such a form correctly reproduces Eq. (7) as both limits are determined solely by the first (universal) term in (5). One needs, however, to keep B in order to properly handle the case of moderate absorption ($\alpha \sim 1$).

The figure shows the results of numerical simulations with random matrices drawn from the Gaussian orthogonal (GOE, $\beta = 1$), unitary (GUE, $\beta = 2$), or symplectic (GSE, $\beta = 4$) ensemble. The overall agreement of Eq. (5) with the data at $\beta = 1$ is nearly as good as for the exact cases $\beta = 2, 4$. Another check was performed in [13], which measured the distributions of the reflection coefficient and the scattering phase in a broad range of system parameters and found very good agreement with the corresponding expressions following from Eq. (5) (see also Eq. (16) below).

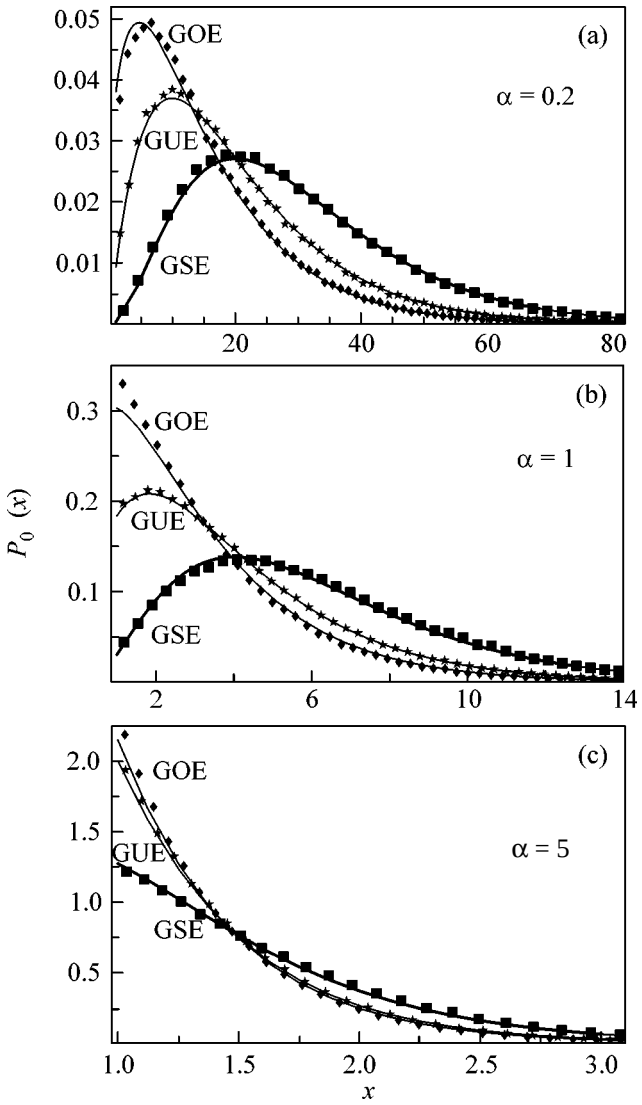

The distribution $P_0(x)$ (Eq. (5)) at different values of the absorption parameter $\alpha = \beta\pi\Gamma/\Delta$. The solid lines correspond to the $\beta = 1$ (GOE) and 2 (GUE) cases and to the exact $\beta = 4$ (GSE) result (Eq. (6)). The symbols stand for the numerics performed for 400 realizations of 500×500 random matrices.

We now discuss the behavior of $\mathcal{P}_v(v)$ and $\mathcal{P}_u(u)$. Performing the integration in Eq. (3), we arrive for $\beta = 2$ at

$$\mathcal{P}_v^{\mathrm{gue}}(v) = (\gamma/16\pi)^{1/2}v^{-3/2}\exp[-\gamma(v+v^{-1})/4] \times\left[2\cosh\frac{\gamma}{2} + (v+v^{-1}-2/\gamma)\sinh\frac{\gamma}{2}\right], \quad (8)$$

which is exactly the LDoS distribution obtained earlier in [5]. For the case $\beta = 1$, we get the following result:

$$\mathcal{P}_v^{\rm goe}(v) = \frac{\mathcal{N}_1 e^{-a}}{\pi\sqrt{2\gamma}\,v^{3/2}} \times (A[K_0(a) + K_1(a)]a + \sqrt{\pi}Be^{-a}), \quad (9)$$

with $a \equiv \frac{\gamma}{16}(\sqrt{v} + 1/\sqrt{v})^2$ and $K_\nu(z)$ being the MacDonald function. It is instructive to consider the asymptotic behavior of these functions in the limits of small or large absorption. At $\gamma \ll 1$, the distribution $\mathcal{P}_v(v)$ becomes very broad having a maximum at $v \sim \gamma$ and a power-law bulk behavior and an exponential cutoff at the far tails:

$$\mathcal{P}_v(v) \propto \begin{cases} \alpha^{(1+\beta)/2} v^{-(3+\beta)/2} e^{-\alpha/4v}, & v \ll \alpha \\ \alpha^{1/2} v^{-3/2}, & \alpha \ll v \ll 1/\alpha \\ \alpha^{(1+\beta)/2} v^{-(3-\beta)/2} e^{-\alpha v/4}, & 1/\alpha \ll v, \end{cases} \quad (10)$$

where constants ~1 are omitted. This result can be physically interpreted in the single-level approximation [5, 8] when the bulk and tail behavior is governed by spectral and wave function fluctuations, respectively. As γ increases, the number of levels contributing to v grows as ~γ; consequently, $\mathcal{P}_v(v)$ tends to the limiting (almost Gaussian at $\gamma \gg 1$) distribution

$$\mathcal{P}_v(v) = \sqrt{\frac{\alpha}{4\pi v^3}} \exp\left[-\frac{\alpha}{4}\left(\sqrt{v} - \frac{1}{\sqrt{v}}\right)^2\right], \quad (11)$$

which has a peak at $v \sim 1$ of width $\propto 1/\sqrt{\gamma} \ll 1$ in agreement with the earlier result [8].

As to the distribution $\mathcal{P}_u(u)$, equation (4) leads after the integration to the following exact $\beta = 2$ result:

$$\mathcal{P}_u^{\rm gue}(u) = \frac{\gamma}{2\pi}\left[\sinh\frac{\gamma}{2} K_0\left(\frac{\gamma\tilde{u}}{2}\right) + \frac{\cosh\frac{\gamma}{2}}{\tilde{u}} K_1\left(\frac{\gamma\tilde{u}}{2}\right)\right], \quad (12)$$

where $\tilde{u} \equiv \sqrt{u^2 + 1}$. Integrating the interpolation formula for the case $\beta = 1$, we obtain

$$\mathcal{P}_u^{\rm goe}(u) = \frac{\mathcal{N}_1 e^{-\gamma/4}}{2\pi\tilde{u}}\left[\frac{A}{2}\sqrt{\frac{\gamma}{4}} D\left(\frac{\tilde{u}}{2}\right) + BK_1\left(\frac{\gamma\tilde{u}}{4}\right)\right], \quad (13)$$

where $D(z) \equiv \int_0^\infty dq \sqrt{1 + z(q + q^{-1})} e^{-\gamma z(q+q^{-1})/4}$ is introduced for convenience. The limiting forms of $\mathcal{P}_u(u)$ at weak and strong absorption follow readily as

$$\mathcal{P}_u(u) \simeq \begin{cases} \pi^{-1}(1 + u^2)^{-1}, & \alpha \ll 1 \\ \sqrt{\alpha/4\pi} e^{-\alpha u^2/4}, & \alpha \gg 1, \end{cases} \quad (14)$$

and describe a crossover from the Lorentzian to the Gaussian distribution as the absorption grows. This type of behavior, as well as the trend of $\mathcal{P}_v(v)$ to the Gaussian (11), was recently observed in the experimental study of the cavity impedance [11].

Finally, let us mention that the case of nonperfect coupling, $T < 1$, can be mapped [31, 32] onto that of the perfect one by making use of the parameterization [33] $S_0 = (S - \sqrt{1-T})/(1 - \sqrt{1-T}\,S)$. Here, S_0 is the scattering matrix of the system in the perfect coupling case. Now, x and θ do correlate, and, after the evaluation in parameterization (1) of the corresponding Jacobian, the joint distribution $P(x, \theta)$ is found to be

$$P(x, \theta) = \frac{1}{2\pi} P_0(xg - \sqrt{(x^2 - 1)(g^2 - 1)}\cos\theta), \quad (15)$$

with $g \equiv 2/T - 1$. Complementary to Eq. (2), equation (15) provides an access to scattering observables. The integration there over x yields the scattering phase distribution. In particular, when the absorption vanishes, $x \longrightarrow \infty$ ($r \longrightarrow 1$) and $P_0(x) \longrightarrow \delta(1/x)$ readily give $P(x, \theta) = \rho(\theta)\delta(1/x)$ with the phase density $\rho(\theta) = [2\pi(g - \sqrt{g^2 - 1}\cos\theta)]^{-1}$, which was found earlier [32]. As another example, the distribution of the reflection coefficient in terms of $P_0(x)$ is given at arbitrary coupling by (cf. Eq. (5) in [18] and see also [13, 17] in this respect)

$$P_r(r) = \int_0^{2\pi} \frac{d\theta\pi^{-1}}{(1-r)^2} P_0\left[\frac{2(g - \sqrt{g^2 - 1}\sqrt{r}\cos\theta)}{1-r} - g\right]. \quad (16)$$

In conclusion, although rigorous analytical treatment of the $\beta = 1$ case remains a theoretical challenge, it is worth stressing, however, that the suggested interpolation formulas should be sufficient for most practical purposes of comparison to the data.[1]

Moreover, all the physically interesting limiting cases, e.g., Eqs. (10), (11), and (14), are already reproduced from the exact limiting statistics (7) and are in agreement with the available experimental data [11, 13].

ACKNOWLEDGMENTS

We are grateful to S. Anlage, P. Brouwer, U. Kuhl, A. Mirlin, H.J. Sommers, and E. Strahov for useful communications at various stages of this work. This work was supported by the SFB/TR 12 der DFG.

[1] We note, at the same time, that the excellent performance of the interpolation formula (5) for $\beta = 1$ is nothing else than a lucky coincidence. Indeed, applying the same formula for the $\beta = 4$ case, we found that, apart from the well-reproduced limits of the weak and strong absorption, the agreement with the numerics at intermediate values, $\gamma \sim 1$, turns out to be by far not as good as in the GOE ($\beta = 1$) case.

REFERENCES

1. H.-J. Stöckmann, *Quantum Chaos: An Introduction* (Cambridge Univ. Press, Cambridge, 1999).
2. T. Guhr, A. Müller-Groeling, and H. A. Weidenmüller, Phys. Rep. **299**, 189 (1998).
3. Y. Alhassid, Rev. Mod. Phys. **72**, 895 (2000).
4. Y. V. Fyodorov and Y. Alhassid, Phys. Rev. A **58**, R3375 (1998).
5. K. B. Efetov and V. N. Prigodin, Phys. Rev. Lett. **70**, 1315 (1993).
6. C. W. J. Beenakker, Phys. Rev. B **50**, 15170 (1994).
7. A. D. Mirlin and Y. V. Fyodorov, Europhys. Lett. **25**, 669 (1994).
8. N. Taniguchi and V. N. Prigodin, Phys. Rev. B **54**, 14305 (1996).
9. C. Dembowski *et al.*, Phys. Rev. Lett. **89**, 064101 (2002).
10. R. A. Méndez-Sánchez *et al.*, Phys. Rev. Lett. **91**, 174102 (2003).
11. S. Hemmady *et al.*, cond-mat/0403225; X. Zheng *et al.*, cond-mat/0408317; cond-mat/0408327.
12. J. Barthélemy, O. Legrand, and F. Mortessagne, cond-mat/0401638; cond-mat/0402029.
13. U. Kuhl *et al.*, cond-mat/0407197.
14. S. A. Ramakrishna and N. Kumar, Phys. Rev. B **61**, 3163 (2000).
15. E. Kogan, P. A. Mello, and H. Liqun, Phys. Rev. E **61**, R17 (2000).
16. C. W. J. Beenakker and P. W. Brouwer, Physica E (Amsterdam) **9**, 463 (2001).
17. D. V. Savin and H.-J. Sommers, Phys. Rev. E **68**, 036211 (2003).
18. Y. V. Fyodorov, JETP Lett. **78**, 250 (2003).
19. I. Rozhkov *et al.*, Phys. Rev. E **68**, 016204 (2003); D. V. Savin and H.-J. Sommers, Phys. Rev. E **69**, 035201(R) (2004); Y. V. Fyodorov and A. Ossipov, Phys. Rev. Lett. **92**, 084103 (2004).
20. A. V. Andreev and B. D. Simons, Phys. Rev. Lett. **75**, 2304 (1995).
21. I. L. Aleiner and V. I. Fal'ko, Phys. Rev. Lett. **87**, 256801 (2001).
22. K. Sacha and J. Zakrzewski, Phys. Rev. Lett. **86**, 2269 (2001).
23. J. Bolte and J. Harrison, J. Phys. A **36**, 2747 (2003).
24. Y. V. Fyodorov and H.-J. Sommers, J. Math. Phys. **38**, 1918 (1997).
25. V. V. Sokolov and V. G. Zelevinsky, Nucl. Phys. A **504**, 562 (1989).
26. A. D. Mirlin and Y. V. Fyodorov, Phys. Rev. Lett. **72**, 526 (1994); J. Phys. I **4**, 655 (1994).
27. P. W. Brouwer and C. W. J. Beenakker, Phys. Rev. B **55**, 4695 (1997).
28. Y. V. Fyodorov, unpublished.
29. A. Borodin and E. Strahov, math-ph/0407065.
30. V. A. Gopar, P. A. Mello, and M. Büttiker, Phys. Rev. Lett. **77**, 3005 (1996).
31. P. W. Brouwer, Phys. Rev. B **51**, 16878 (1995).
32. D. V. Savin, Y. V. Fyodorov, and H.-J. Sommers, Phys. Rev. E **63**, 035202 (2001).
33. P. A. Mello, P. Pereyra, and T. Seligman, Ann. Phys. (N.Y.) **161**, 254 (1985).

JETP Letters, Vol. 80, No. 12, 2004, pp. 730–733. Translated from Pis'ma v Zhurnal Éksperimental'noĭ i Teoreticheskoĭ Fiziki, Vol. 80, No. 12, 2004, pp. 860–864.

X-ray Spectroscopic Observations of a Superdense Plasma in Nanoparticles Irradiated by Superintense Femtosecond Laser Radiation

A. Ya. Faenov[1], T. A. Pikuz[1], I. Yu. Skobelev[1], A. I. Magunov[1], V. P. Efremov[2], M. Servol[3], F. Quéré[3], M. Bougeard[3], P. Monot[3], Ph. Martin[3], M. Francucci[4], G. Petrocelli[4], and P. Audebert[5]

[1] *Multicharged Ion Spectra Data Center, NPO VNIIFTRI, Mendeleevo, Moscow region, 141570 Russia*
e-mail: skobelev@izmaylovo.ru
[2] *Institute of High Temperatures Scientific Association (IVTAN), Russian Academy of Sciences, Izhorskaya ul. 13/19, Moscow, 127412 Russia*
[3] *DSM-DRECAM-Service des Photons, Atomes et Molécules, CEA Saclay, 91191 Gif-sur-Yvette Cedex, France*
[4] *Dipartimento di Scienze e Technologie Fisiche ed Energetiche, Universita di Roma "Tor Vergata," 00133 Rome, Italy*
[5] *LULI (CNRS), Ecole polytechnique, 91 128 Palaiseau Cedex, France*

Received November 9, 2004

The interaction of femtosecond laser pulses with SiO_2 aerogel targets has been analyzed by x-ray spectroscopic methods. The use of an aerogel target with transparent grains makes it possible to considerably reduce the requirements on laser-pulse contrasts for which heating occurs without the formation of a preplasma. A nanoplasma with a density sevenfold higher than the solid-state density has been detected. © *2004 MAIK "Nauka/Interperiodica".*

PACS numbers: 52.50.Jm; 52.70.La

1. Investigations of the interaction of intense ultrashort laser pulses with solid and gas targets have become particularly urgent in recent years. Such investigations, first, enable one to study the fundamental properties of matter under extreme conditions and, second, give new approaches for solving a number of applied problems such as the initiation of nuclear fusion, the acceleration of electrons and heavy ions, and the creation of sources of intense x-ray radiation for medical and biological purposes and lithography (see, e.g., [1–4]). According to the first experiments with solid targets, the contrast of a laser pulse, i.e., the ratio $K = P_{\text{pulse}}/P_{\text{prep}}$ of the power of the main laser pulse to the power of the prepulse, is a very important parameter determining the interaction of ultrashort laser pulses with matter. In particular, the formation of a superdense plasma turned out to be possible only with the use of pulses of very high contrast $K \sim 10^{10}$, when the heating-radiation flux density in the prepulse is insufficient for the formation of preplasma and the main-pulse energy is absorbed immediately in a solid (see, e.g., [5–11]). However, as was experimentally shown in [5], the requirements for the contrast are weaker when targets transparent to heating laser radiation are used.

The role of the contrast becomes particularly important when spatially inhomogeneous targets with the nanometer characteristic size of inhomogeneities are used. Among such targets are cluster targets where the cluster sizes vary from fractions of a nanometer to hundreds of nanometers and porous targets with approximately the same inhomogeneity parameters. The use of such targets, first, ensures the efficient absorption of energy in the target regions with a high density and, second, owing to the decreased average density of the target, increases the energy contribution per one atom of the target substance and improves the conditions for the observation and diagnostics of the radiation from the irradiated region. The features of nanostructure targets can be completely manifested if the duration of a heating laser pulse lies in the subpicosecond range and is not larger than the time of gas-dynamic scattering of clusters and the contrast of the laser pulse is high enough so that a preplasma that could destroy the spatially inhomogeneous structure of the target is not formed. In other words, if $\tau \ll R/C(T)$, where τ is the duration of the laser pulse, R is the radius of a nanoparticle, and $C(T)$ is the bulk speed of sound, then the nanoparticle is heated and a solid-density plasma is formed when the radiation power is sufficient [5–11]. Similar properties were observed for pulsed x-ray radiation [12].

After the heating stage, the formed nanoplasma decays and its average density begins to decrease. One can expect that, upon the volume heating of the nanoparticle at the early stage of decay, the central part of the nanoplasma will first be compressed due to ablation

pressure and certain plasma regions at certain times will have density higher than the solid-state density. However, such a compression of nanotargets has not yet been observed.

In this work, to increase the effective contrast of the laser pulse, aerogel targets with grains transparent to heating laser radiation are used. This enables us to obtain nanoplasma with a density sevenfold higher than the solid-state density upon the heating of an aerogel target by femtosecond laser pulses of moderate contrast.

2. Experimental investigations were carried out on a laser setup at the Saclay Research Center (France) [13]. A Ti–Sa laser with a wavelength of 800 nm and a repetition frequency of 20 Hz was used. The energy of the laser pulse reached 40 mJ and its duration varied in the range 50 fs–1.2 ps due to the change in the distance between the compressor grids. The time contrast of the laser pulse was equal to 3×10^6 and 10^4 in the nanosecond and picosecond ranges, respectively. Figure 1 shows the scheme of the experiment. The interaction of the laser pulses with SiO_2 aerogel targets was studied. The targets were made of a porous substance with cubic pores with a size of about 20 nm formed by chains of SiO_2 grains each about 3 nm in size. A continuous flow of an aerogel powder [14] with particles of sizes 50–500 μm was supplied due to gravity to the interaction region from a conic funnel with an opening angle of 100° and an outlet hole 0.9 mm in diameter. The laser radiation was focused onto a spot whose diameter was equal to about 15 μm so that the heating radiation flux density varied in the range 10^{16}–4×10^{17} W/cm^2. In each pulse, the substance was degraded in the irradiation region. However, since the displacement of the target substance between the pulses was equal to several millimeters, the next pulse of laser radiation was focused on the fresh substance.

The x-ray spectra was detected in the range 6.1–6.4 Å by an FSSR spectrograph [15–17] with a spherically bent quartz crystal $10\bar{1}1$ ($2d$ = 6.6 Å) with a curvature radius of R = 150 mm and a 15×50-mm working region. X rays were detected by an RAR-2492 Kodak film, which was protected from visible and ultraviolet radiation by two layers of a polypropylene film that had a thickness of 1 μm and was covered with an aluminum layer 0.2 μm thick. The dispersion scheme was adjusted for work in the first reflection order (the distance from the plasma source to the crystal was equal to 210 mm, the Bragg angle was equal to $\Theta = 69.4°$, and the distance from the crystal to the film was equal to 64.9 mm). This scheme allowed the observation of the Ly_α resonance line of the hydrogen-like Si XIV ion and its dielectron satellites with a spectral resolution of $\lambda/\delta\lambda \sim 5000$. The spectra were detected with a one-dimensional spatial resolution of about 20 μm, and the laser beam propagated in the plane of spatial resolution (see Fig. 1). Figure 2 shows the density patterns of the resulting spectra.

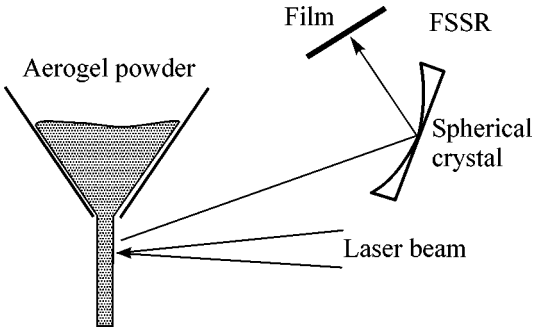

Fig. 1. Scheme of the experiment.

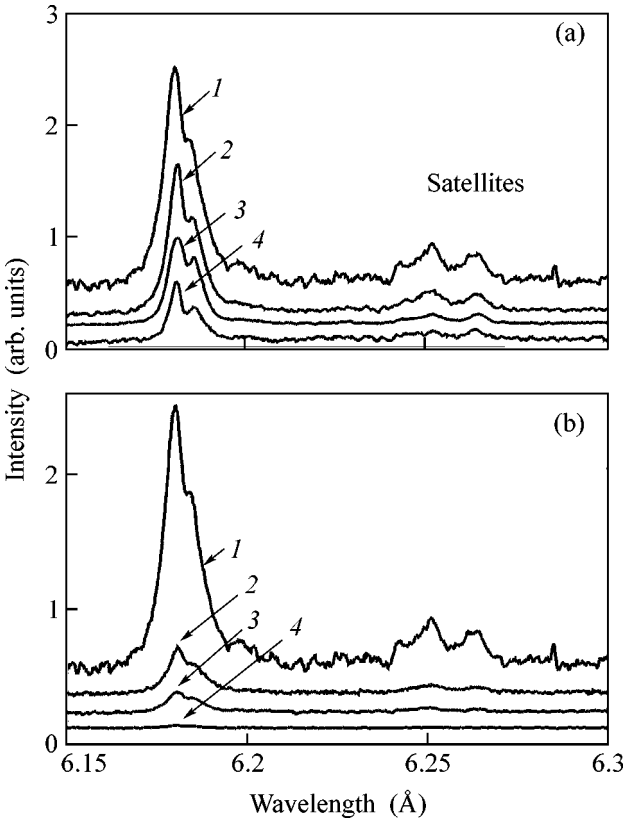

Fig. 2. Density patterns obtained for the (a) duration τ_{las} = (*1* and *7*) 54, (*2*) 110, (*3*) 500, (*4*) 1100, and (*5* and *6*) 55 fs and (b) energy E_{las} = (*1*) 34, (*2*) 39, (*3*) 36, (*4*) 28, (*5*) 23, (*6*) 11, and (*7*) 4 mJ of a laser pulse.

3. The spectra detected for the Ly_α resonance line of the hydrogen-like Si XIV ion and its dielectron satellites make it possible to estimate the parameters of the produced plasma. As is known (see, e.g., [18]), the ratio of the intensities of the resonance line and its dielectron satellites is sensitive to the electron plasma temperature T_e and the structure of the intensities of the satellites is sensitive to the electron plasma density N_e (see also [19]). Figure 3 shows the results of calculation of the spectra using the FLY package based on the stationary

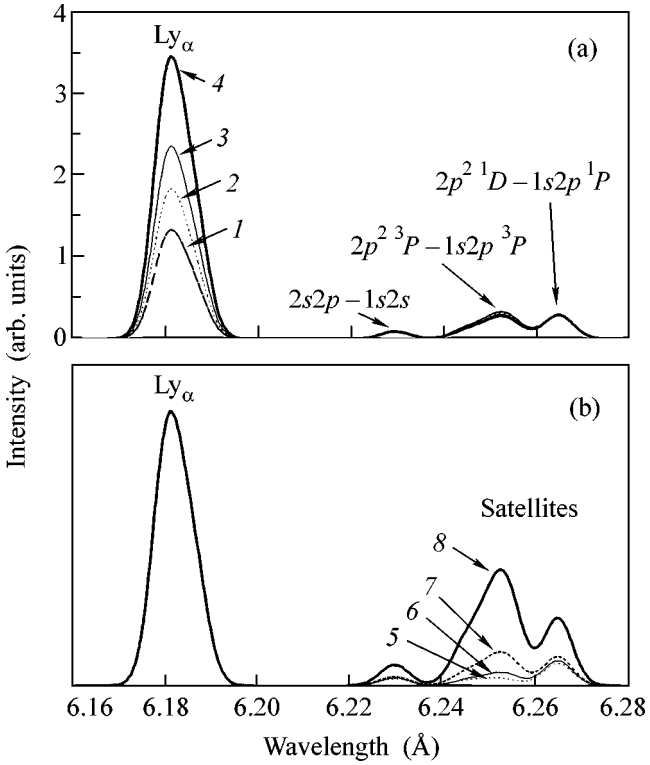

Fig. 3. Radiation spectra of the silicon plasma near the Ly$_\alpha$ line of the Si XIV ion as calculated for the (a) temperature T_e = (*1*) 500, (*2*) 600, (*3*) 700, (*4*) 900, and (*5–8*) 800 eV and (b) density N_e = (*1–4*) 6.24×10^{23}, (*5*) 10^{22}, (*6*) 10^{23}, (*7*) 10^{24}, and (*8*) 10^{25} cm^{-3} of the plasma.

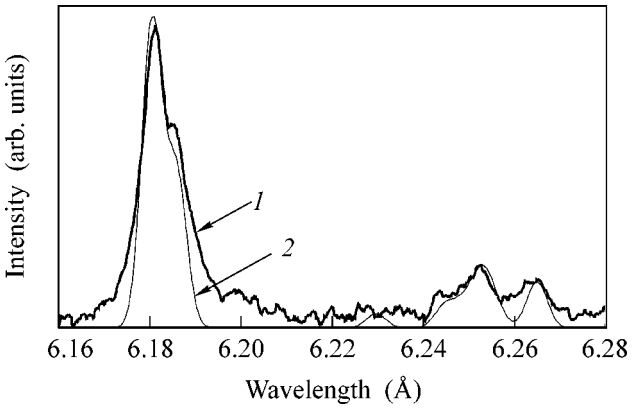

Fig. 4. (*1*) Experimental spectrum detected for $q_{las} = 3.6 \times 10^{17}$ W/cm^2 and (*2*) calculation for $N_e = 4.4 \times 10^{24}$ cm^{-3} and T_e = 900 eV.

radiative–collision kinetic model [20–22]. As is seen in this figure, the structure of the intensities of the satellite lines is nearly independent of the temperature and changes significantly when the density changes, and the sensitivity of the spectrum to the density remains at $N_e \sim 10^{25}$ cm^{-3}.

The comparison of the experimental spectra shown in Fig. 2 with the calculated spectra (Fig. 3a) shows that the observed structure of the satellites cannot be described under the assumption that the plasma density is equal to (or less than) the solid-state density. For $N_e = N_e^{solid} = 6.24 \times 10^{23}$ cm^{-3}, the intensity of the group of triplet satellite transitions $2p^2\,{}^3P$–$1s2p^3P$ for all the T_e values does not exceed the intensity of the singlet satellite $2p^2\,{}^1D_2$–$1s2p^1P_1$, whereas experiment shows the inverse relation to be particularly pronounced for the maximum fluxes of heating laser radiation. Detailed comparison of the experimental and calculation spectra shown in Fig. 4 indicates that the plasma density in the experiments is higher than the solid-state density and is equal to ~$(0.6–4.4) \times 10^{24}$ cm^{-3}. The table presents the results obtained in several experiments with various energies and durations of the laser pulse. As is seen in the table, the measured N_e values are determined primarily by the laser-radiation flux density and, in particular, the plasma has the same density in two experiments with significantly different energies and durations but with the same flux.

The table also presents the T_e values measured from the ratio of the intensities of the resonance line and satellite structures. Note that the accuracy of the determination of T_e is much lower than that for N_e, because the observed spectrum is an integral in time and contains contributions from all the plasma-evolution stages including the stage of the decay of the dense plasma. At this stage, the plasma is nonequilibrium due to recombination and its radiation is determined primarily by recombination processes (radiative and three-particle) that quite efficiently excite the resonance line but do not affect the intensities of the dielectron satellites. This additional contribution to the intensity of the resonance line is disregarded in the calculation model. As a result, the calculated intensity is somewhat overestimated; i.e., the electron temperature of the plasma is somewhat overestimated. On the contrary, the error in the calculation of the intensities of the dielectron-satellite spectrum is determined only by the accuracy of the atomic constants used, and, according to our estimates, the error in the measurement of N_e does not exceed (but is likely much better than) 20%.

As is seen in the table, when the laser flux decreases, the characters of the decrease in the plasma temperature are different in two cases: first, when the flux changes due to a decrease in the energy of a pulse whose duration is constant and, second, when this change occurs due to a change in its duration with a fixed energy. In the first case (experiments 1, 5, and 6), the temperature decreases rapidly from 900 to 600 eV when the flux decreases by one third. In the second case (experiments 1, 2, and 3), when the flux decreases even by an order of magnitude, the temperature decreases only to 800 eV. This property is also clearly seen in Fig. 2, according to which the plasma luminosity decreases

Parameters of the plasma for various parameters of a heating laser pulse. The experiment number corresponds to the spectrum number in Fig. 2

No.	Laser pulse parameters			Plasma parameters	
	Energy, mJ	Duration, fs	Flux, W cm^{-2}	T_e, eV	N_e, cm^{-3}
1	34	54	3.6×10^{17}	900	4.4×10^{24}
5	23	54	2.4×10^{17}	700	2.2×10^{24}
2	39	110	2×10^{17}	900	2.2×10^{24}
6	11	55	1.1×10^{17}	600	$(1–1.5) \times 10^{24}$
3	36	500	4.1×10^{16}	800	8×10^{23}
4	28	1100	1.4×10^{16}	600	6.2×10^{23}

sharply and smoothly with a decrease of the energy of the laser pulse and an increase in its duration, respectively. Such a behavior of the temperature (and, therefore, the luminosity) of the plasma is simply explained. If the plasma is heated quite rapidly so that the process is isochoric, then its temperature is determined by the energy absorbed rather than by the laser radiation flux density. Therefore, the plasma temperature drops when the energy of the pulse decreases (experiments 1, 5, and 6). At the same time, it is nearly unchanged when the duration of the pulse increases (experiments 1, 2, and 3). The process becomes nonisochoric only when the pulse duration increases to 0.5–1.1 ps. In this case, the plasma has time to expand significantly in the heating process, its density decreases, and a portion of the laser pulse passes through it without absorption. A decrease in the energy contribution results in a corresponding decrease in the temperature (experiments 3 and 4). Therefore, a rough estimate of the time τ_d of the existence of a superdense plasma region is determined by the maximum duration of the laser pulse for which the plasma temperature does not noticeably decrease. For the conditions under consideration, $\tau_d \sim 100–500$ fs.

Thus, a nanoplasma with density sevenfold higher than the solid-state density was detected in this work upon the heating of an aerogel target by femtosecond laser pulses. In a previous work [11], an aluminum plasma with an electron density of 10^{24} cm^{-3}, which is also higher than the solid-state value, was observed upon the heating of a flat solid target by a 150-fs laser pulse with a much higher time contrast of 10^{10}. The use of an aerogel target with transparent glass grains makes it possible to considerably reduce the requirements for laser-pulse contrasts for which heating occurs without the formation of a preplasma.

This work was supported in part by the program Access to Research Infrastructure Action of the Improving Potential Program, contract no. HPRI-CT-2002-00191.

REFERENCES

1. T. Ditmire, T. Donnelly, A. M. Rubenchik, *et al.*, Phys. Rev. A **53**, 3379 (1996).
2. P. Gibbon and E. Forster, Plasma Phys. Controlled Fusion **38**, 769 (1996).
3. H. M. Milchberg, S. J. Mcnaught, and E. Parra, Phys. Rev. E **64**, 056402 (2001).
4. P. Audebert, R. Shepherd, K. B. Fournier, *et al.*, Phys. Rev. E **66**, 066412 (2002).
5. A. Zigler, P. G. Burkhalter, D. J. Nagel, *et al.*, Opt. Lett. **16**, 1261 (1991).
6. A. Ya. Faenov, J. Abdallah, Jr., R. E. H. Clark, *et al.*, Proc. SPIE **3157**, 10 (1997).
7. A. M. Urnov, J. Dubau, A. Ya. Faenov, *et al.*, Pis'ma Zh. Éksp. Teor. Fiz. **67**, 489 (1998) [JETP Lett. **67**, 489 (1998)].
8. A. Ya. Faenov, A. I. Magunov, T. A. Pikuz, *et al.*, Phys. Scr. T **80**, 536 (1999).
9. A. Maksimchuk, M. Nantel, G. Ma, *et al.*, J. Quant. Spectrosc. Radiat. Transf. **65**, 367 (2000).
10. F. B. Rosmej, U. N. Funk, M. Gessel, *et al.*, J. Quant. Spectrosc. Radiat. Transf. **65**, 477 (2000).
11. A. Saemann, K. Eidmann, I. E. Golovkin, *et al.*, Phys. Rev. Lett. **82**, 4843 (1999).
12. B. R. Gafarov, E. S. Yushkov, V. P. Efremov, and E. B. Druzhkov, Khim. Fiz. **14**, 24 (1995).
13. M. Servol, F. Quéré, M. Bougeard, *et al.*, submitted to Appl. Phys. Lett.
14. http://www.cabot-corp.com/nanogel.
15. A. Ya. Faenov, S. A. Pikuz, A. I. Erko, *et al.*, Phys. Scr. **50**, 333 (1994).
16. I. Yu. Skobelev, A. Ya. Faenov, B. A. Bryunetkin, *et al.*, JETP **81**, 692 (1995).
17. B. K. F. Young, A. L. Osterheld, D. F. Price, *et al.*, Rev. Sci. Instrum. **69**, 4049 (1998).
18. V. A. Boiko, A. V. Vinogradov, S. A. Pikuz, *et al.*, J. Sov. Laser Res. **6**, 83 (1985).
19. A. Ya. Faenov, I. Yu. Skobelev, S. A. Pikuz, *et al.*, Phys. Rev. A **51**, 3529 (1995).
20. R. W. Lee, B. L. Whitten, and R. E. Strout, J. Quant. Spectrosc. Radiat. Transf. **32**, 91 (1984).
21. R. W. Lee and J. T. Larson, J. Quant. Spectrosc. Radiat. Transf. **56**, 535 (1996).
22. R. W. Lee, J. Quant. Spectrosc. Radiat. Transf. **40**, 561 (1988).

Translated by R. Tyapaev

JETP Letters, Vol. 80, No. 12, 2004, pp. 734–738. From Pis'ma v Zhurnal Éksperimental'noĭ i Teoreticheskoĭ Fiziki, Vol. 80, No. 12, 2004, pp. 865–869.

Nonlinear Evolution of a Relativistically Strong Electromagnetic Wave in Self-Created Electron–Positron Plasma¶

S. S. Bulanov[1], A. M. Fedotov[2], and F. Pegoraro[3]

[1] *Institute of Theoretical and Experimental Physics, Moscow, 117218 Russia*
[2] *Moscow State Engineering Physics Institute, Moscow, 115409 Russia*
[3] *Department of Physics, University of Pisa and INFM, Pisa, Italy*
e-mail: bulanov@heron.itep.ru, fedotov@cea.ru, pegoraro@df.unipi.it

Received November 11, 2004

The nonlinear interaction between the electron–positron pairs produced by an electromagnetic wave in plasma and the wave leads to damping of the wave, frequency upshift, change of polarization, and particle acceleration. The case of a circularly polarized wave is investigated in the framework of the relativistic Vlasov equation with a source term based on the Schwinger formula for the pair creation rate. © *2004 MAIK "Nauka/Interperiodica".*

PACS numbers: 12.20.Fv; 13.40.–f; 52.20.–j; 52.27.–h; 52.35.Mw

The effect of particle creation in vacuum by an external field was first used to investigate the production of electron–positron pairs in a constant, spatially homogeneous electric field [1–3]. It is often referred to as the Schwinger mechanism and is considered as one of the most intriguing nonlinear phenomena in quantum field theory. The effect lies beyond the reach of the perturbation theory, and its experimental verification would test the validity of the theory in the region of strong fields. It is believed that the most probable way of detecting this effect is connected with e^+e^- pair production by lasers under the action of a time-varying electromagnetic (EM) field [4–7], especially, in view of the recent developments in laser technology [8]. In addition, several methods for reaching the critical intensity $I_{Sch} = 4.6 \times 10^{29}$ W/cm^2 (which corresponds, for a laser pulse with the wavelength ≈ 1 μm, to an electric field equal to the critical Schwinger field $E_{Sch} = 1.32 \times 10^{16}$ V/cm) with presently available systems have been proposed recently [9, 10].

However, we should note that, in [1–7], the mutual interaction of the particles produced and the effect of these particles on the original electric field (backreaction) are not taken into account. The problem of the backreaction of the produced particles on the background field was discussed extensively in a number of papers on the particle formation process in high-energy hadronic interactions [11–13] as well as under the action of electric fields [14]. It was understood that, in solving a dynamical problem with a strong initial electric field, the effect of the produced particles on the electric field (the backreaction) should be taken into consideration. A kinetic equation coupled to Maxwell equations was used to solve this problem. However, the spatially homogeneous time-dependent electric field that was used is not a solution of Maxwell equations in vacuum. We also note that, in [11–14], special attention was paid to the properties of the emerging plasma, while the properties of the background field were not studied in detail.

In the present paper, we consider the process of e^+e^- pair production in a cold collisionless plasma by an EM field, which is an actual solution of the Maxwell equations (a similar approach was used in [15, 16]), as well as the backreaction of the produced pairs on the background field. In doing so, we use the kinetic equation with a source term obtained from the pair production rate [11, 12]. In order to elucidate the role of the magnetic field component of the EM wave on the e^+e^- pair production, we consider a planar, circularly polarized wave propagating in an underdense collisionless plasma[1] For the sake of simplicity, we consider an e^+e^- plasma:

$$\mathbf{A} = A_0[\mathbf{e}_x \cos(\omega t' - kz) + \mathbf{e}_y \sin(\omega t' - kz)], \qquad (1)$$

where A_0, ω, and k are the wave amplitude, frequency, and wave vector, respectively, and t' is the time in the laboratory frame. In the case of a planar wave in a plasma, the first field invariant $\mathcal{F}$ is not equal to zero due to the different dispersion equation with respect to that in vacuum:

$$\mathcal{F} = \frac{1}{2}(\mathbf{E}^2 - \mathbf{B}^2) = \frac{\Omega^2}{2}A_0^2 \equiv \frac{1}{2}\left(\frac{\Omega}{\omega}\right)^2 E_0^2, \qquad (2)$$

¶ This article was submitted by the authors in English.

[1] In the following, we use the $c = 1$ and $\hbar = 1$ convention.

where $\Omega = [8\pi e^2 n_0/(m^2 + P^2)^{1/2}]^{1/2}$ is the Langmuir frequency, which enters the dispersion equation for the EM wave propagating in the plasma in the laboratory frame:

$$\omega^2 = k^2 + \Omega^2, \quad (3)$$

and P is the momentum of the plasma particles. Therefore, in a plasma, e^+e^- pairs can be produced by a planar EM wave as was shown in [15]. The nonlinear EM wave in plasmas is also characterized by the dependence of its phase and group velocity on the plasma parameters and on the wave amplitude ($v_{ph} = \omega/k$, $v_g = \partial\omega/\partial k$; see Eq. (3)). In this case, a Lorentz transform to the reference frame moving with the group velocity v_g of the wave transforms the EM field into a purely electric field that rotates with constant frequency and with no associated magnetic field

$$\mathbf{E} = \Omega A_0(\mathbf{e}_x \sin\Omega t - \mathbf{e}_y \cos\Omega t). \quad (4)$$

Further, we shall use the notation $E = \Omega A_0 \equiv (\Omega/\omega)E_0$. Although this transformation reduces the problem under consideration to the situation where the pairs are produced by a time-varying electric field, the effects of the wave magnetic field are incorporated rigorously into our model (see also [17, 18]).

We consider the propagation of a circularly polarized EM wave in an underdense collisionless plasma in the boosted frame of reference. The relativistic kinetic equation

$$\frac{\partial f_\alpha}{\partial t} + e_\alpha \mathbf{E}(t)\frac{\partial f_\alpha}{\partial \mathbf{p}} = q_\alpha(|\mathbf{E}|, p), \quad (5)$$

describes the dependence on time and momentum of the positron (electron) distribution function $f_\alpha(\mathbf{p}, t)$ in the boosted frame where a spatially homogeneous electric field $\mathbf{E}(t)$ is present. The distribution function is normalized in such way that $\int f_\alpha(\mathbf{p}, t)d^3p/(2\pi)^3 = n_\alpha$ gives the number n_α of positrons or electrons per unit volume and e_α is their electric charge with $\alpha = +$ for positrons and $\alpha = -$ for electrons. The source term in Eq. (5) is proportional to the quasi-classical probability

$$\exp\left[-\frac{\pi(m^2 + p_\perp^2)}{|e\mathbf{E}(t)|}\right] \quad (6)$$

of tunneling through the gap between the lower and the upper continuum of the electron energy spectrum in the presence of the constant electric field. However, the naive estimation of the characteristic time of the pair production c/l_c, $l_c = \hbar/mc$, as well as the quasi-classical tunneling time $t_{tun} = 1/a\omega$ [6, 15], where $a = eA/mc$, is negligible with respect to the wave period. Thus, it is possible to use expression (6) for the time-varying electric field with the time playing the role of a parameter. In addition, following the reasoning of [11, 12], we assume that the pairs are produced at rest; i.e., the momentum distribution of the source term is taken to be proportional to the Dirac delta function

$$q_\alpha(|\mathbf{E}|, p) = 2e^2|\mathbf{E}(t)|^2 \exp\left[-\frac{\pi m^2}{|e\mathbf{E}(t)|}\right]\delta(\mathbf{p}). \quad (7)$$

This assumption is reinforced by the fact that the momentum distribution in Eq. (6) has a width $p_\perp \sim (|e\mathbf{E}(t)|)^{1/2} = m(|\mathbf{e}(t)|)^{1/2} \ll m$, which is negligible with respect to the momentum that the electrons (positrons) acquire in the electric field. Here, $\mathbf{e} = \mathbf{E}/E_{Sch} \ll 1$ is the normalized electric field and $E_{Sch} = m^2/e$ is the critical Schwinger field. The source term has been normalized in such way that

$$W(\mathbf{E}) = \int q_\alpha(|\mathbf{E}|, \mathbf{p})\frac{d^3p}{(2\pi)^3} = \frac{|e\mathbf{E}|^2}{4\pi^3}\exp\left[-\frac{\pi m^2}{|e\mathbf{E}|}\right], \quad (8)$$

where $W(E)$ gives positrons (electrons) produced according to the Schwinger formula.

We solve Eq. (5) by integrating it along the particle characteristics. Introducing a function $\mathbf{A}(t) = -\int_0^t \mathbf{E}(s)ds$, we obtain the distribution function

$$f_\alpha = f_{\alpha,0}[p_\parallel, \mathbf{p}_\perp + e_\alpha\mathbf{A}(t)] + \int_0^t q_\alpha\{\mathbf{p}_\perp + e_\alpha[\mathbf{A}(t) - \mathbf{A}(s)], s\}ds, \quad (9)$$

where $f_{\alpha,0}(p_\parallel, \mathbf{p}_\perp)$ is the distribution function of the initial plasma positrons (electrons) before the passage of the EM wave. Let us assume that, at the initial time $t = 0$, the plasma is cold; consequently, $f_{\alpha,0} = n_0(2\pi)^3\delta(p_\perp)\delta(p_\parallel - p_{\parallel,0})$, where $p_\perp$ and $p_\parallel$ are the components of the particle momentum perpendicular and parallel to the direction of the EM wave propagation and $p_{\parallel,0}$ is its initial value, which arises from the Lorentz transform from the laboratory to the boosted frame.

The modification of the kinetic equation given by the source term in Eq. (7) must also be accompanied by a change of the source term in the Maxwell equations. The e^+e^- pair production leads to the appearance of a time-dependent electric dipole that generates a polarization current. Thus, the current density in the Maxwell equation for the electric field acquires an additional term with respect to the situation when no pair production is present [12]:

$$\frac{d\mathbf{E}}{dt} = -4\pi\mathbf{j}_{tot} = -4\pi(\mathbf{j}_{cond} + \mathbf{j}_{pol}). \quad (10)$$

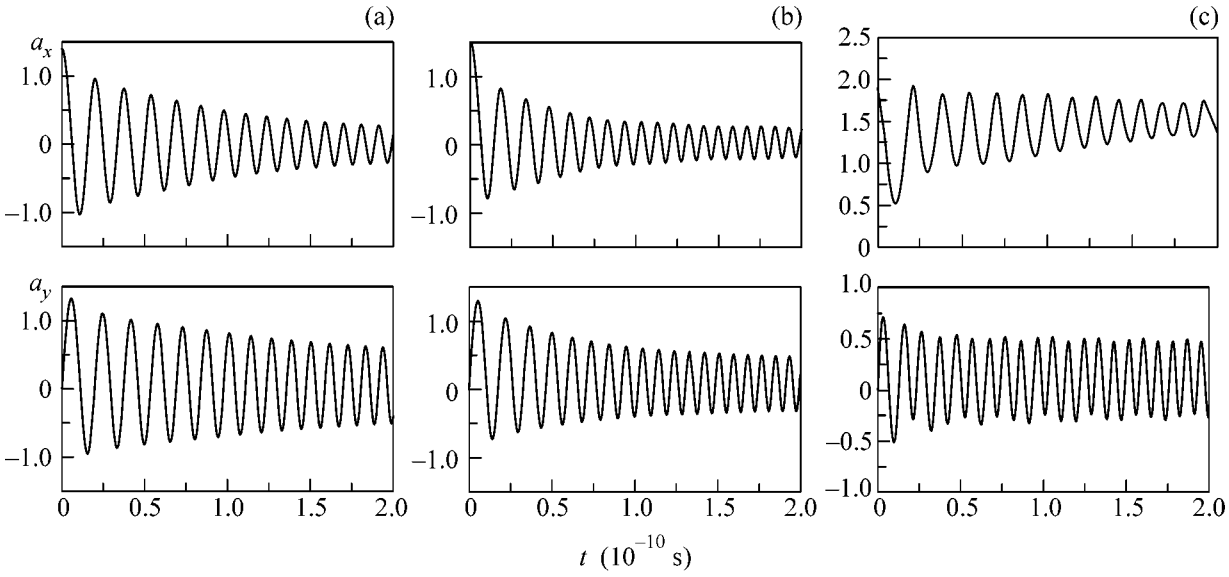

Fig. 1. Time evolution in the moving frame of the x and the y components of the dimensionless vector potential for different initial amplitudes: $a = 1.4 \times 10^5$ (a), $a = 1.5 \times 10^5$ (b), $a = 1.9 \times 10^5$ (c) with the initial plasma density $n_0 = 10^{19}$ cm^{-3} in the moving frame; $v_g \approx 1$, $\gamma_g = 10$. The upper row shows the x component of the vector potential; the lower, the y component. On the x axis, the time is measured in seconds; $a = 1$ corresponds (for a 1 μm wavelength pulse) to an intensity of 10^{18} W/cm^2 and $a = 4.6 \times 10^5$, to the Schwinger intensity.

Here, the conduction and polarization [11] currents are

$$\mathbf{j}_{\text{cond}}(t) = e \sum_{\alpha = +,-} \int f_\alpha(\mathbf{p}, t) \frac{\mathbf{p}}{\mathscr{E}} \frac{d^3p}{(2\pi)^3},$$
$$\mathbf{j}_{\text{pol}}(t) = \frac{\mathbf{E}(t)}{|\mathbf{E}(t)|^2} \sum_{\alpha = +,-} \int q_\alpha(\mathbf{p}, t) \mathscr{E} \frac{d^3p}{(2\pi)^3}, \quad (11)$$

where $\mathscr{E} = (m^2 + p^2)^{1/2}$. Using the distribution function (9), the dimensionless vector-potential $\mathbf{a} = e\mathbf{A}/m$, and the normalized electric field $\mathbf{e} = e\mathbf{E}/m^2$, we obtain a system of equations for the electric field evolution in the presence of the pair production

$$\frac{d\mathbf{a}(t)}{dt} = -m\mathbf{e}(t),$$

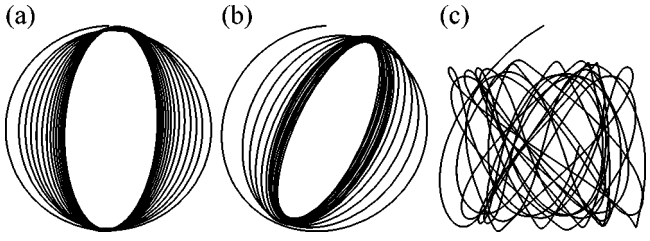

Fig. 2. Trajectories of the projections of the electric field polarization vector for the same set of initial conditions as in Fig. 1.

$$\frac{d\mathbf{e}(t)}{dt} = \frac{\Omega^2}{m}\mathbf{a}(t) - \frac{em}{2\pi^2}\mathbf{e}(t)\exp\left[-\frac{\pi}{|\mathbf{e}(t)|}\right] \quad (12)$$
$$+ \frac{\kappa}{8\pi^3 m^2}\int_0^t \frac{[\mathbf{a}(t) - \mathbf{a}(s)]|\mathbf{e}(s)|^2}{[1 + |\mathbf{a}(t) - \mathbf{a}(s)|^2]^{1/2}}\exp\left[-\frac{\pi}{|\mathbf{e}(s)|}\right]ds.$$

Here, $P = m[1 + \tilde{p}_{\|0}^2 + a^2(t)]^{1/2}$ (see the definition of Ω given above), $\tilde{p}_{\|0} \equiv p_{\|0}/m$ and $\kappa = 8\pi e^2 m^4$, where the factor m^4 stands for the inverse of the invariant Compton 4 volume $m^4 = c/l_c^4 \approx 0.14 \times 10^{53}$ cm^{-3} s^{-1}.

Numerical solutions of this system are presented in Fig. 1 for different initial amplitudes. We can see that the process of e^+e^- pair production leads to the damping of the wave in the plasma and to the nonlinear upshift of its frequency. The damping occurs due to the fact that each event of the pair creation takes a portion of the field energy equal to $2mc^2$ and the amount needed for the particle acceleration. The upshift of the field frequency is due to the increase of the plasma density and thus of the Langmuir frequency as new pairs are created (see also [18]). This frequency upshift is seen in Fig. 1 and bears a strong resemblance to the blue shift of an EM wave that propagates in a medium that becomes ionized, as was investigated theoretically in [19] and experimentally in [20].

Since the pair production rate depends on the field amplitude exponentially, an unbalanced damping of the field components can occur and lead to a change of the

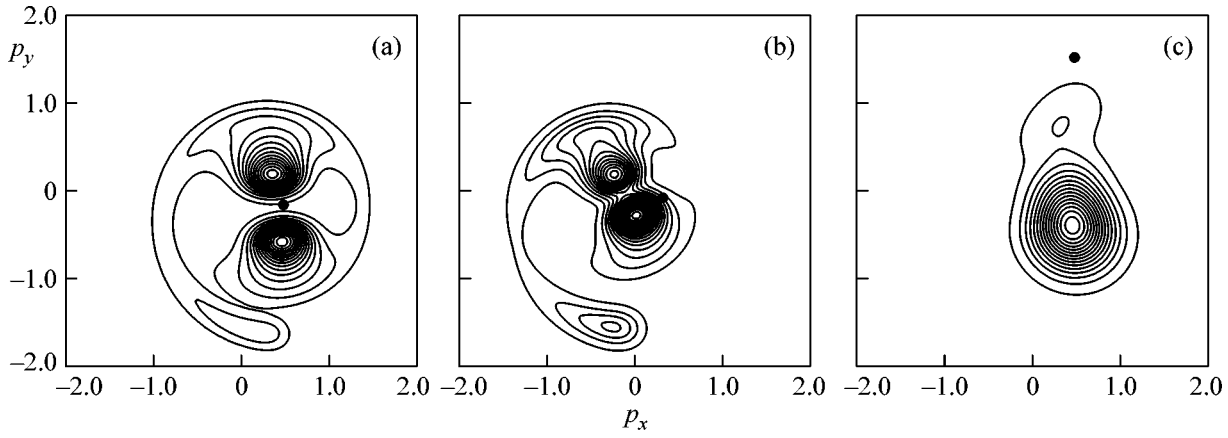

Fig. 3. The electron distribution functions versus p_x and p_y in the moving reference frame for the same set of initial conditions as in Fig. 1 at the time 2×10^{-10} s. The particle momenta are normalized on the dimensionless vector-potential amplitude a multiplied times 10^5. The black circles correspond to the initial plasma particle distribution at the time 2×10^{-10} s.

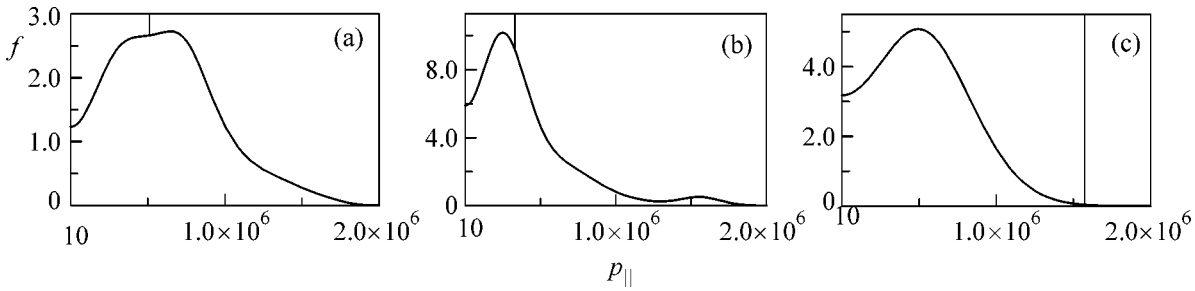

Fig. 4. The electron distribution functions versus $p_{||}$ in the laboratory reference frame for the same set of initial conditions as in Fig. 1 at the time 2×10^{-10} s. The momentum is measured in the same units as in Fig. 3. The vertical lines correspond to the distribution of the initial plasma particles.

field polarization. These properties of the electric field are shown in Fig. 2, where the projections of the polarization vector are presented for the same set of initial parameters as in Fig. 1. In Fig. 2a, we see the damping of the x component of the electric field and the transition from circular to elliptic polarization with the major axis of the ellipse directed along the y axis. In addition, in Fig. 2b, we see a rotation of the principal axes of the ellipse. The situation shown in Fig. 2c is different from the previous situation. In this latter case, the pair production rate at the beginning of the field evolution is so large that the first wave oscillation cycle cannot be completed, which leads to oscillations of the x component of the wave vector potential around a nonzero mean value determined by the balance between the time-averaged parts of the first two terms on the right-hand side of the second of Eqs. (12). This shift of the center of the oscillations of the x component of the vector potential leads to a reduction of the oscillation frequency of this wave component, so that, in this case, the x and the y components of the wave oscillate at different frequencies.

The difference between the above three cases is clearly illustrated by the different shapes of the particle distribution functions in the p_x–p_y plane (note that the electron and the positron distributions are the mirror image of each other). In cases (a) and (b), electrons and positrons are mostly created at the maxima of the electric field $|\mathbf{E}|$ (and thus of the vector potential $|\mathbf{A}|$). Since at birth $\mathbf{p}_\perp = 0$, in the case of a circularly polarized electric field, this should lead to a ring-type distribution. However, since the wave polarization becomes elliptical because of the backreaction due to the pair creation, the distribution function of each population consists (in the canonical momentum $\mathbf{p}_\perp + e_a\mathbf{A}$ plane) mainly of two blobs at $\pm e_a\mathbf{A}_{\max}$. In the p_x–p_y plane, these blobs move according to the time evolution of the vector potential $\mathbf{A}$. On the contrary, the position of the initial distribution function (denoted by a dark dot in the figure) corresponds to $\mathbf{p}_\perp + e_a\mathbf{A} = 0$. In case (c), the pairs are created mostly at the start at $\mathbf{p}_\perp + e_a\mathbf{A} = e_a\mathbf{A}(t = 0)$. Since the time evolution of $\mathbf{A}(t)$ is ergodic, as shown in Fig. 3, their distribution tends to be randomized in the p_x–p_y plane.

The particle distribution function is shown in Fig. 4 versus the parallel momentum $p_\parallel$ in the laboratory frame. Note that, in case (c), the strong damping of the wave due to the pair creation and the resulting nonadiabatic interaction led to a strong acceleration of the particles in the initial plasma. Such large values of the longitudinal momentum of the electrons (positrons) in the laboratory frame are due to the transverse acceleration of the electrons (positrons) in the moving frame. Performing the Lorentz transform back to the laboratory frame, we obtain for the longitudinal momentum in the laboratory frame of the initial electrons and positrons $p_\parallel = \gamma_g[p_{\parallel 0} + v_g(1 + p_{\parallel 0}^2 + |\mathbf{a}^2|)^{1/2}] \approx \gamma_g v_g|\mathbf{a}|$, where we used $|\mathbf{a}| \gg |p_{\parallel 0}|$.

In summary, the production of e^+e^- pairs by the electromagnetic wave propagation in the plasma leads to the upshifting of the wave frequency and to the damping of the wave amplitude and changes the polarization state of the wave.

The authors would like to acknowledge fruitful discussions with N.B. Narozhny, V.D. Mur, L.B. Okun, and V.S. Popov. This work was supported in part by the Russian Foundation for Basic Research (project no. 03-02-17348) and the Federal Program of the Russian Ministry of Industry, Science, and Technology (grant no. 40.052.1.1.1112).

REFERENCES

1. F. Sauter, Z. Phys. **69**, 742 (1931).
2. W. Heisenberg and H. Z. Euler, Z. Phys. **98**, 714 (1936).
3. J. Schwinger, Phys. Rev. **82**, 664 (1951).
4. E. Brezin and C. Itzykson, Phys. Rev. D **2**, 1191 (1970).
5. V. S. Popov, JETP Lett. **13**, 185 (1971); Sov. Phys. JETP **34**, 709 (1972); JETP Lett. **18**, 255 (1973); Sov. J. Nucl. Phys. **19**, 584 (1974).
6. M. S. Marinov and V. S. Popov, Sov. J. Nucl. Phys. **16**, 449 (1973).
7. N. B. Narozhny and A. I. Nikishov, Sov. Phys. JETP **38**, 427 (1974).
8. T. Tajima and G. Mourou, Phys. Rev. ST Accel. Beams **5**, 031301 (2002); physics/0111091.
9. D. L. Burke, S. C. Berridge, C. Bula, *et al.*, Phys. Rev. Lett. **79**, 1626 (1997).
10. S. V. Bulanov, T. Zh. Esirkepov, and T. Tajima, Phys. Rev. Lett. **91**, 085001 (2003).
11. K. Kajantie and T. Matsui, Phys. Lett. B **164B**, 373 (1985); G. Gatoff, A. K. Kerman, and T. Matsui, Phys. Rev. D **36**, 114 (1987).
12. Y. Kluger, J. M. Eisenberg, and B. Svetitsky, Phys. Rev. Lett. **67**, 2427 (1991); Y. Kluger, E. Mottola, and J. M. Eisenberg, Phys. Rev. D **58**, 125015 (1998).
13. S. Schmidt, D. Blanschke, G. Ropke, *et al.*, Int. J. Mod. Phys. E **7**, 709 (1998); J. C. R. Bloch, V. A. Myserny, A. V. Prosorkevich, *et al.*, Phys. Rev. D **60**, 116011 (1999).
14. C. E. Dolby and S. F. Gull, Ann. Phys. (N.Y.) **297**, 315 (2002); R. Ruffini, L. Vitagliano, and S. S. Xue, Phys. Lett. B **559**, 12 (2003).
15. S. S. Bulanov, Phys. Rev. E **69**, 036408 (2004).
16. S. S. Bulanov, N. B. Narozhny, V. D. Mur, and V. S. Popov, Phys. Lett. A **330**, 1 (2004); hep-ph/0403163.
17. H. K. Avetissian, A. K. Avetissian, G. F. Mkrtchian, and Kh. V. Sedrakian, Phys. Rev. E **66**, 016502 (2002).
18. S. S. Bulanov, A. M. Fedotov, and F. Pegoraro, submitted to Phys. Rev. E.
19. V. B. Gil'denburg, V. I. Pozdnyakova, and I. A. Shereshevskii, Phys. Lett. A **203**, 214 (1995); E. Conejero Jarque, F. Cornolti, and A. Macchi, J. Phys. B **33**, 1 (2000).
20. S. P. Kuo, Phys. Rev. Lett. **65**, 1000 (1990); N. Yugami, T. Niiyama, T. Higashiguchi, *et al.*, Phys. Rev. E **65**, 036505 (2002).

JETP Letters, Vol. 80, No. 12, 2004, pp. 739–742. Translated from Pis'ma v Zhurnal Éksperimental'noĭ i Teoreticheskoĭ Fiziki, Vol. 80, No. 12, 2004, pp. 870–874.

Generation of Nonclassical States of Light in the Bose–Einstein Condensate under Electromagnetically Induced Transparency

A. V. Prokhorov, A. P. Alodjants, and S. M. Arakelian

Vladimir State University, Vladimir, 600000 Russia

e-mail: laser@vpti.vladimir.ru

Received October 27, 2004

A quantum theory of the interaction of the atomic Bose condensate with external optical fields has been developed for a two-beam Λ-scheme close to resonance. Regimes have been obtained where the coefficients of Kerr nonlinearity and nonlinear absorption reach giant values and even become negative, which gives rise to the effect of nonlinear electromagnetically induced transparency. The possibility of the efficient generation of quadrature-squeezed light under the condition of the nonlinear compensation of optical losses has been shown.

PACS numbers: 32.80.–t; 42.50.Gy; 42.65.–k

Interest in investigation of electromagnetically induced transparency (EIT) has considerably increased recently [1, 2]. This effect is the propagation of a probe pulse without damping and with the conservation of an envelop shape in a three-level atomic medium with the inversion of populations created by optical pumping. A fundamental property of this effect is a considerable, up to 17 m/s [1], decrease in the group velocity of the probe pulse under the conditions of the propagation of dark and bright polaritons. Such a behavior of an atomic–optical system with memory can be used for processing and transmission of quantum information. At the same time, strong quantum correlations of polaritons can give rise to the generation of nonclassical entangled atomic-optical states [3, 4]. In principle, the possibility of the generation of giant nonlinearity values in the Λ-interaction regime with the use of coherent media was experimentally shown in [5].

In this work, we solve the problem of the interaction of the three-level atomic condensate with external optical fields under the condition of EIT. In this problem, we consider the effects of both linear (in the Jaynes–Cummings approximation) and nonlinear (Kerr) polarizations of condensate atoms.

The optical properties of the atomic Bose condensate upon its Λ-interaction with the pumping optical field of frequency ω_c and test field ω_p (Fig. 1) with the inclusion of the nonlinear polarization of atoms can be described in terms of its index of refraction $n = n_0 + n_2|A_p|^2$ and absorption coefficient $\alpha = \alpha_0 + \alpha_2|A_p|^2$. Here,

$$n_0 = 1 + \frac{1}{2}\mathrm{Re}(\chi_{\mathrm{AT}}^{(1)}), \quad \alpha_0 = \beta_p \mathrm{Im}(\chi_{\mathrm{AT}}^{(1)}), \tag{1a}$$

$$n_2 = \frac{3}{8}\mathrm{Re}(\chi_{\mathrm{AT}}^{(3)}), \quad \alpha_2 = \frac{3}{4}\beta_p \mathrm{Im}(\chi_{\mathrm{AT}}^{(3)}). \tag{1b}$$

Here, $\chi_{\mathrm{AT}}^{(1,3)}$ are the linear and Kerr resonance susceptibilities of the atomic condensate, respectively. Using the standard density-matrix formalism and the relation $P = N\mu_{32}\bar{\rho}_{32}$ [6, 7] for polarization induced in the atomic medium, where N is the atomic density, $\bar{\rho}_{32}$ is the matrix element for the $|3\rangle \longrightarrow |2\rangle$ transition, and μ_{32} is the corresponding dipole moment, we obtain the following expressions for the resonance susceptibilities (cf. [1, 5]):

$$\chi_{\mathrm{AT}}^{(1)} = \frac{N|\mu_{32}|^2}{\hbar\varepsilon_0}\frac{1}{\Gamma},$$
$$\chi_{\mathrm{AT}}^{(3)} = \frac{2i}{3}\frac{N|\mu_{32}|^4}{\varepsilon_0\hbar^3}\frac{\Gamma^* - \Gamma}{\Gamma|\Gamma|^2}\left(\frac{1}{\gamma_{\mathrm{opt}}} + \frac{1}{\gamma_{\mathrm{mag}}}\right). \tag{2}$$

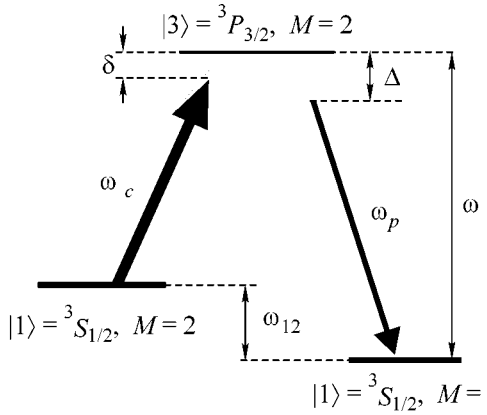

Fig. 1. Λ-scheme of interaction for ^{23}Na atomic energy levels.

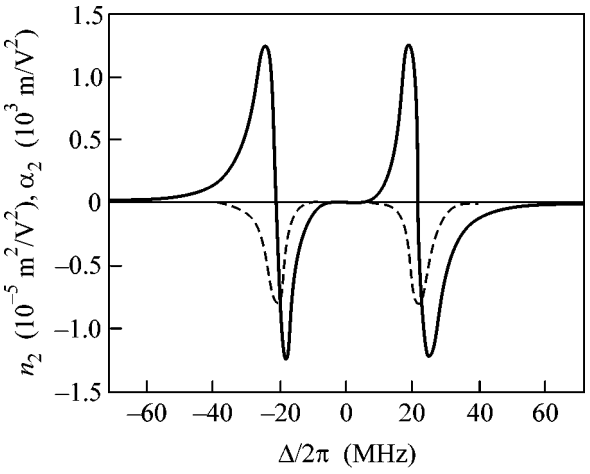

Fig. 2. Frequency dependences of the (solid line) nonlinear index of refraction n_2 and (dashed line) nonlinear absorption coefficient α_2 for the ^{23}Na condensate upon the Λ-interaction with external optical fields. The condensate parameters are $N = 3.3 \times 10^{12}$ cm^{-3}, $\gamma_{opt}/2\pi = 10.2$ MHz, and $\gamma_{mag}/2\pi = 38.2$ kHz. The intensity of a transparency pulse is equal to $I_c = 55$ mW/cm^2.

Here, $\Gamma = \Delta - i\gamma_{opt} + |g_1|^2/(i\gamma_{mag} - \Delta)$, where $g_1 = |\mu_{31}|E_c/\hbar$ is the Rabi frequency for the $|1\rangle \longrightarrow |3\rangle$ transition induced by the transparency field $\mathbf{E}_c$; $\gamma_{opt} = \gamma_{32} + \gamma_{31}$ and $\gamma_{mag} = \gamma_{12}$, where γ_{mn} with $m, n = 1, 2, 3$ describe the spontaneous transitions from the corresponding levels and determine the natural width of the radiation lines for the cold atoms in the condensate; $\Delta = \omega - \omega_p$; and $\delta = \omega - \omega_{12} - \omega_c$.

Figure 2 shows the nonlinear index of refraction n_2 and the nonlinear absorption coefficient α_2 as functions of the frequency detuning Δ of the test field upon the Λ-interaction and in the presence of the strong pumping field $\mathbf{E}_c$ for the atomic density $N = 3.3 \times 10^{12}$ cm^{-3} according to the experiment [1]. In this case, the dipole transition element $|\mu_{32}|$ is equal to 22×10^{-30} C m, and the Rabi frequency $g_1/2\pi = 21.5$ MHz for the intensity of a transparency field is calculated for an intensity of $I_c = 55$ mW/cm^2 with the use of the relation $A_c = \sqrt{2I_c/c\varepsilon_0}$. In the absence of the Doppler broadening of the radiation lines in the condensate, the rate γ_{mn} of the spontaneous decay of atoms is determined by their relaxation time $\tau_{mn} \approx 2\pi/\gamma_{mn}$. They are equal to $\tau_{32} = 0.2$ μs, $\gamma_{31}/2\pi = \gamma_{32}/2\pi = 5.1$ MHz, and the decay rate on the magnetic levels $|1\rangle$ and $|2\rangle$ corresponds to $\gamma_{12}/2\pi = 38.2$ kHz and the relaxation time $\tau_{12} = 26$ μs cm [7].

As is seen in Fig. 2, the parameters n_2 and α_2 can take giant values and be negative. The existence of regions with $n_2 < 0$ is important for the practical problems of the generation and control over the parameters of nonclassical light. At the same time, the presence of negative nonlinear absorption $\alpha_2 < 0$ in Fig. 2 leads to the change of the linear absorption regime for optical radiation in the Bose gas to the regime with effective enhancement when reaching the corresponding threshold intensity of the test field. When $\alpha \equiv 0$, light is not absorbed by the atomic medium, which can be treated as the effect of the EIT of the Bose condensate.

Thus, control over the intensity I_p of the test field and its detuning Δ from the resonance makes it possible to change the relation between the relative contributions of the linear and nonlinear effects for the field propagating in the condensate. This property is responsible for the realization of diverse regimes.

Let us discuss the quantum properties of the test field and their effect on EIT. In the adiabatic approximation, where the population regime for atoms of condensate modes can be considered as steady, the state of the atomic system is given [2]. This approximation is valid if the relaxation time for the lower levels of the scheme satisfies the condition $\tau_{12} \geq \tau_d$ [2], where $\tau_d = n_g(l/c)$ determines the delay time of a pulse passing through the resonance condensate medium with a group index of refraction $n_g = n + \omega_p(dn/d\omega_p)$. In this case, the Hamiltonian of the interaction between the condensate atoms and test field can be obtained using the corresponding transition matrix element multiplied by the atomic–optical interaction constant: $H_{int} = -(k_0/2)(\bar{\rho}_{32} + \bar{\rho}_{23})$, where $k_0 = \mu_{32}\sqrt{\omega/2\hbar\varepsilon_0 V}$ and V is the characteristic interaction volume. With allowance for nonlinear effects based on the cubic susceptibility $\chi^{(3)}$, the matrix element $\bar{\rho}_{32}$ can be expanded in a series in the Rabi frequency of the test field in the form $\bar{\rho}_{32} \cong \bar{\rho}_{32}^{(1)} g_1 + \bar{\rho}_{32}^{(3)} |g_1|^2 g_1$. Finally, the interaction Hamiltonian has the form

$$H_{int} = -\frac{k_0^2}{2}(\bar{\rho}_{32}^{(1)} a^+ + \bar{\rho}_{23}^{(1)} a) - \frac{k_0^4}{2}(\bar{\rho}_{32}^{(3)} (a^+)^2 a + \bar{\rho}_{23}^{(3)} a^+ (a)^2), \quad (3)$$

where $a(a^+)$ is the annihilation (creation) operator of the test-field photons. The first term in Eq. (3) corresponds to the interaction of the condensate with the test field in the framework of the Jaynes–Cummings model. The second term in Eq. (3) is determined by the nonlinear polarization of the atomic system.

To describe the behavior of quantum fluctuations of the test field, we use the Bogoliubov method, which is extensively applied both in statistical physics for studying quasiparticles in mesoscopic quantum systems [8] and in quantum optics for describing the spontaneous parametric scattering of light in the approximation of a given classical pumping field [6]. In this work, the application of this method to analysis of the quantum characteristics of the test field is justified by the adia-

batic approximation when the properties of both the atomic system and transparency (pumping) field are given (see Eq. (3) and cf. [2]). We represent the annihilation operator of a test field of photons in the form $a = f + \Delta a$, where f determines the classical amplitude ($\langle a \rangle = f$) and the operator $\Delta a \equiv c = a - \langle a \rangle$ determines the small fluctuation part of the field, so that $\langle \Delta a \rangle \equiv \langle c \rangle = 0$. Using Eq. (3) in the Heisenberg representation, we arrive at the following system of equations for the mean field f and quantum-noise operator c:

$$\frac{df}{dt} = i\left(\frac{k_1}{2} + \frac{k_2^*}{2} f^2 + k_2 |f|^2\right), \quad \frac{dc}{dt} = i(\theta c + \eta c^+), \quad (4)$$

where $k_1 = k_0^2 \rho_{32}^{(1)}$ and $k_2 = k_0^4 \rho_{32}^{(3)}$ are the coefficients determining the linear and nonlinear energy transfer in the system, respectively; and $\theta = k_2 f^* + k_2^* f$ and $\eta = k_2 f$.

The second of Eqs. (4) is linearized with respect to the small-fluctuation operator c. It is valid under the condition $\langle c^+ c \rangle \ll |f|^2$, and its solution can be represented in the form (cf. [6, 8])

$$c = \mu c_0 + \nu c_0^+, \quad (5a)$$

$$\mu = \cos(\sqrt{\xi} t) + i\frac{\theta}{\sqrt{\xi}} \sin(\sqrt{\xi} t), \quad \nu = i\frac{\eta}{\sqrt{\xi}} \sin(\sqrt{\xi} t), \quad (5b)$$

where $\xi = k_2^2 (f^*)^2 + (k_2^*)^2 f^2 + |k_2|^2 |f|^2$ and $c_0 \equiv c(t)|_{t=0}$. The operators of annihilation c and creation c^+ of quasiparticles satisfy the usual commutation relations $[c; c^+] = |\mu|^2 - |\nu|^2 = 1$ and characterize small quantum perturbations of the test field—bright polaritons propagating in the atomic medium under the conditions of EIT. In this case, the mean number of test-field photons $N_f = \langle a^+ a \rangle = |f|^2 + \langle c^+ c \rangle$ can change both due to a change in the mean-field intensity and in the process of the parametric enhancement of quantum noise (quasiparticles), which becomes possible for $\xi < 0$.

Figure 3 shows the time dependence of the mean number N_f of photons in the probe pulse for various initial numbers of photons at the condensate entry. The detuning frequency of the probe pulse with a duration of 1 μs is taken close to the resonance and is equal to $\Delta/2\pi = 2.66$ MHz. In this case, the coefficients $\alpha_0 > 0$ and $\alpha_2 < 0$ have different signs, which makes it possible to analyze the competition between the linear damping and nonlinear enhancement of the test field in the system under consideration (see Fig. 2). In this case, the threshold intensity N_f of the test field is equal to 25 photons. Figure 3 demonstrates two fundamentally different evolution regimes for the mean number of photons in the probe pulse. First, when the initial mean number of photons is equal to $N_f = |f|^2 = 26$, the nonlinear enhancement threshold is exceeded and a parametric increase in the test-field intensity is observed. Second, when the initial mean number of photons is equal to

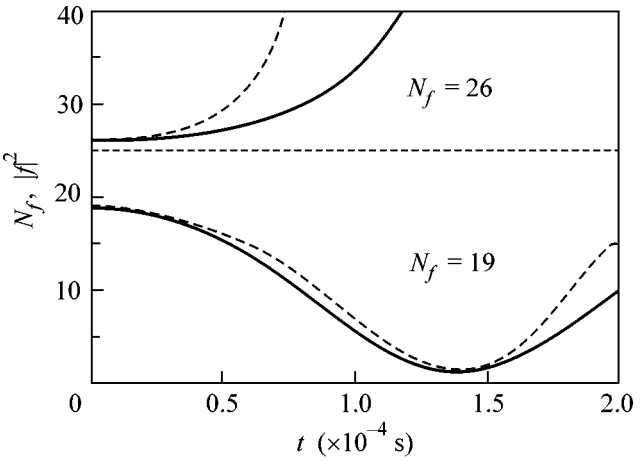

Fig. 3. Time dependence of the photon number N_f of the test field (solid lines for $|f|^2$) in the mean-field approximation and (dashed lines) with inclusion of quantum fluctuations. The parameters of the system are the same as for Fig. 2. The detuning frequency is equal to $\Delta/2\pi = 2.66$ MHz. The initial photon number N_f is indicated near the lines.

$N_f = |f|^2 = 19$, the enhancement threshold is not reached and energy is transferred between the field and condensate in the regime of competition between the linear and nonlinear effects. Each regime is represented by two lines of which one corresponds to the dynamics of the mean field $|f|^2$ and the other presents the dynamics including quantum noise. It is seen that the relative number $\langle \hat{c}^+ \hat{c} \rangle / |f|^2$ is always small in the regime below the threshold. At the same time, the regime of the enhancement of the mean field leads to a fast increase in this number, which corresponds to the parametric enhancement of quantum noise. Since $\langle c^+ c \rangle = |\nu|^2$, the latter case corresponds to the change of sign of the expression for ξ and a hyperbolic increase in ν [see Eq. (5)]. However, even for the case where the initial intensity of the test field is lower than the threshold, the presence of quantum noise in the system can lead to a change in the regime beginning with a certain time—to the enhancement of the test field. It is important that the increase in the mean number of photons shown in Fig. 3 is limited by the pumping intensity, which is treated as classical and inexhaustible. Thus, the approach under consideration implies the condition

$$\langle c^+ c \rangle \ll |f|^2 \ll N_c, \quad (6)$$

where N_c is the number of photons in the pumping field.

Let us determine the Hermitian quadratures $Q = a + a^+$ and $P = i(a^+ - a)$ of the test field. In view of Eqs. (5), their dispersions are represented as $\sigma_Q^2 = |\mu + \nu^*|^2$ and $\sigma_P^2 = |\mu - \nu^*|^2$. Figure 4 shows the time dependences of σ_Q^2 and σ_P^2 for the test field with $N_f = 26$. Quadrature-

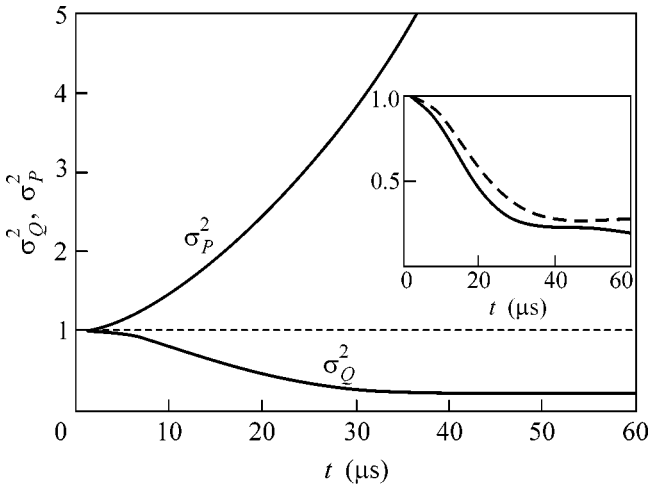

Fig. 4. Time dependences for quadrature dispersions σ_Q^2 and σ_P^2. The parameters of the system are the same as for Fig. 3. The initial number of photons is equal to $N_f = 26$. Inset: the time dependences of σ_Q^2 for N_f = (solid line) 26 and (dashed line) 19.

squeezed light is generated when either σ_Q^2 or σ_P^2 is smaller than unity, which corresponds to the coherent state of the test field at the atomic-system entry. In this case, the efficient suppression of quantum fluctuations of the quadrature Q can be experimentally observed on the characteristic time scale $\tau_{sq} \approx 40$ μs. In particular, if the squeezing time for fluctuations is approximately equal to the pulse delay time τ_d, i.e., $\tau_{sq} \cong \tau_d$, then the optimum length l_{opt} of the active region of the condensate is equal to 7.7 cm, which corresponds to both $n_g = 1.56 \times 10^5$ and the regime of "slow" light for the probe pulse with a group velocity of about 2000 m/s. In this case, for fluctuations of the probe pulse of a duration of τ_p to be efficiently squeezed, it is necessary to satisfy the condition $\tau_{sq} > \tau_p$, which is the case for the microsecond pulse. Finally, we note that conditions (6) are valid over the entire time interval for the dependences shown in Fig. 4. The inset in Fig. 4 shows the results of quadrature squeezing for various numbers of photons of the test field at the condensate entry. It is seen that the enhancement regime for the test field is preferable over competitive regimes for efficient squeezing; see line *1* in Fig. 3.

In the linear case, when $\bar{\rho}_{23}^{(3)} = \bar{\rho}_{32}^{(3)} \equiv 0$, the parameter $k_2 = 0$, so that the quadrature dispersions $\sigma_{Q,P}^2$ remain at the initial level of fluctuations of the coherent field. In this case, the time dependence of the photon number N_f is not sensitive to the initial number of photons at the entry: in the absence of the competition between the linear and nonlinear effects of the energy transfer in the system, either absorption or enhancement of the pulse is observed in dependence on the detuning Δ.

In summary, we note that the optimum length l_{opt} of the atomic–optical interaction can be reached using cigar-shaped condensates obtained in strongly asymmetric traps. The use of optic fibers doped with resonance atoms or fibers filled with the atomic gas condensate is no less interesting and a practically promising possibility of realizing the Λ-interaction for the optical pulses in these fibers. Such an approach makes it possible, first, to sharply increase the nonlinear characteristics of a waveguide, which is the most important point in experiments with squeezed light, and, second, to adjust the scheme so that the forced optical losses are minimal.

We are grateful to A.S. Zibrov, G. Leuchs, and N.V. Korol'kova for stimulating discussions. This work was supported by the Russian Foundation for Basic Research (project no. 04-02-17359) and a Research Program, the Ministry of Industry and Science and the Ministry of Education of the Russian Federation. A.P.A. acknowledges the "Dinastiya" Nonprofit-Program Foundation for support of his scientific activity.

REFERENCES

1. L. N. Hau, S. E. Harris, Z. Dutton, and C. H. Behroozi, Lett. Nature **397**, 594 (1999).
2. M. D. Lukin, Rev. Mod. Phys. **75**, 457 (2003).
3. A. V. Prokhorov, A. P. Alodzhants, and A. M. Arakelyan, Opt. Spektrosk. **94**, 55 (2003) [Opt. Spectrosc. **94**, 50 (2003)].
4. C. H. van der Wal, M. D. Eisaman, A. Andre, *et al.*, Science **301**, 196 (2003).
5. H. Wang, D. Goorskey, and M. Xiao, Phys. Rev. Lett. **87**, 073601 (2001); H. Kang and Y. Zhu, Phys. Rev. Lett. **91**, 093601 (2003).
6. Y. R. Shen, *The Principles of Nonlinear Optics* (Wiley, New York, 1984; Nauka, Moscow, 1989).
7. E. Wolf, in *Progress in Optics* (Elsevier, Amsterdam, 2002), Vol. 43, p. 512.
8. E. M. Lifshitz and L. P. Pitaevskiĭ, *Course of Theoretical Physics*, Vol. 9: *Statistical Physics*, 2nd ed. (Fizmatlit, Moscow, 2001; Pergamon, New York, 1980), Part 2.

Translated by R. Tyapaev

JETP Letters, Vol. 80, No. 12, 2004, pp. 743–747. From Pis'ma v Zhurnal Éksperimental'noĭ i Teoreticheskoĭ Fiziki, Vol. 80, No. 12, 2004, pp. 875–879.

Transitions between π and 0 States in Superconductor–Ferromagnet–Superconductor Junctions¶

N. M. Chtchelkatchev

Landau Institute for Theoretical Physics, Russian Academy of Sciences, Moscow, 117940 Russia
Institute for High-Pressure Physics, Russian Academy of Sciences, Troitsk, Moscow region, 142092 Russia
e-mail: nms@itp.ac.ru

Received November 11, 2004; in final form, November 24, 2004

Experimental and theoretical study of superconductor–ferromagnet–superconductor junctions (SFS junctions) showed that, in a certain range of parameters (e.g., the length of the ferromagnet d_F, the exchange field E_{ex}), the ground state of the SFS junction corresponds to a superconducting phase difference π or 0. The phase diagram of an SFS junction with respect to π and 0 states is investigated in this letter in E_{ex}, d_F, T space. It is shown that the phase diagram is very sensitive to the geometry of the system, in particular, to the amount of disorder in the junction. © *2004 MAIK "Nauka/Interperiodica".*

PACS numbers: 74.50.+r; 74.80.–g; 75.70.–i

Recently, many interesting phenomena have been investigated in superconductor–ferromagnet–superconductor Josephson contacts. One of the most interesting effects is the so-called π state of SFS junctions [1–11] in which the equilibrium ground state is characterized by an intrinsic phase difference π between the two superconductors.

Theoretical study of SFS junctions [1–3] showed that, if E_{ex} is fixed in the ferromagnet, then the π state appears at $0 < d_F^{(1)} < d_F < d_F^{(2)}$, $d_F^{(2)} < d_F^{(3)} < d_F < d_F^{(4)}$, etc., and, near $d_F^{(i)}$ (i = 1, 2, …), the critical current $I_c(d_F)$ has a cusp. Recent experiments [4, 5] showed that the critical current–temperature curve in SFS junctions at $d_F \approx d_F^{(i)}$, where i = 1, 2, also has a cusp. The temperature of the cusp was identified with the π–0 transition temperature. These experiments became the motivation for the theoretical investigations of the $I_c(T)$ curves and phase diagrams of SFS junctions. It was shown in [8, 9] that, if $d_F \approx d_F^{(i)}$ (i = 1, 2, …) in very short ballistic SFS junctions ($d_F \ll \xi_0 = \hbar v_F/\Delta(T = 0)$), then there is a π–0 transition at a certain temperature and the π state is always (for all i) at higher temperatures than the 0 state. This prediction is in contradiction with the experimental data and calculations of the phase diagram in dirty SFS junctions based on linearized Usadel equations (see [5] and references therein), where the order of π and 0 phases with respect to the temperature is one at $d_F \approx d_F^{(1)}$ and the opposite at $d_F \approx d_F^{(2)}$. The SFS junctions investigated in [5] were dirty. At the first glance, it may seem that disorder strongly influences the phase diagram of SFS junctions. This is exactly so. It is shown in this letter that the phase diagram of SFS junctions is rather sensitive to the geometry of the system, in particular, to amount of disorder in the junction.

This paper is organized as follows: most of the paper is devoted to investigations of phase diagrams of SFS junctions near the first cusp of $I_c(d_F)$ (at $d_F \approx d_F^{(1)}$), and the case $d_F \approx d_F^{(i)}$, where $i > 1$, is discussed at end.

The superconducting SFS junction that is investigated here is sketched in Fig. 1. A barrier (e.g., an insulator layer) is situated at the position $x = a$ from the junction center.

First, we will considered ballistic SFS junctions. I assume the following: the exchange energy of the ferromagnet $E_{ex} \ll E_F$; there is no barrier at the SF bound-

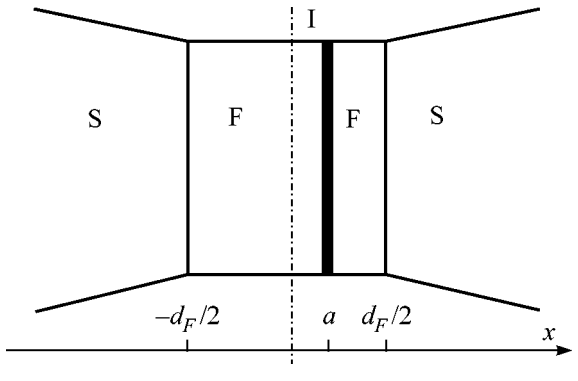

Fig. 1. A sketch of an SFS junction. A barrier (e.g., insulator layer I) is situated at the position $x = a$ from the junction center.

¶ This article was submitted by the author in English.

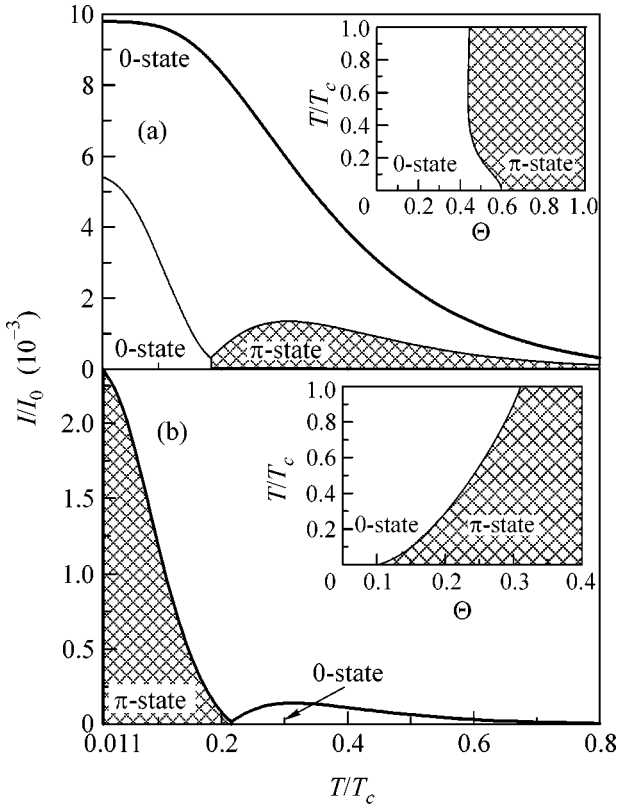

Fig. 2. Critical current–temperature relation in two short SFS junctions with the same normal conductance and $d_F \approx d_F^{(1)}$: (a) ballistic junction, (b) dirty one. The insets show the "phase diagrams" of the junctions. The current scale $I_0 = N_{ch}e\Delta_0/\hbar$, where N_{ch} is the number of open channels in the junction. The thick curve in (a) corresponds to the same $\Theta = 0.18$ as in (b); the other curve in (a) corresponds to $\Theta \approx 0.5$. It is seen that the π state in a ballistic SFS junction is at higher temperatures than the 0 state; the opposite phenomenon takes place in a dirty SFS junction.

aries: the probability of Andreev reflection of subgapped Bogoliubov quasiparticles from an SF boundary is equal to unity; and the variation of the superconducting gap in S near the boundary will be neglected (this is a correct approximation if our SFS is a quantum point contact [12, 13]; in other cases, this approximation can be used because it usually leads to mistakes of only a few percent in the Josephson current). Then, the Josephson current can be found, for instance, using scattering matrix method [8, 12]:

$$I(\varphi) = \frac{2e}{\hbar}\frac{1}{2}\sum_{\sigma=\pm1} T\sum_{\omega}\partial_{\varphi}\ln g(\omega, \varphi, \sigma), \qquad (1)$$

where

$$g(\omega, \varphi, \sigma) = (2\omega^2 + \Delta^2)\cosh(\Phi) + 2\omega\sqrt{\omega^2 + \Delta^2}\sinh(\Phi) + \mathcal{T}\cos\varphi + \mathcal{R}\cosh\beta. \qquad (2)$$

Here, φ is the phase difference between the superconductors; Δ is the bulk superconducting gap; $\omega = 2\pi(n+1/2)$, $n = 0, \pm1, \ldots$; $\Phi = 2d_F(\omega + iE_{ex}\sigma)/\hbar v_F\cos\theta$, $\beta = 4a(\omega + iE_{ex}\sigma)/\hbar v_F\cos\theta$ and $\mathcal{T} = t_\uparrow t_\downarrow$, $\mathcal{R} = r_\uparrow r_\downarrow$, where $(t_\uparrow)^2$ and $(r_\uparrow)^2$ are the transmission and reflection probabilities of the barrier for spin-up electrons, and θ is the angle between the trajectory and the X axis. Equations (1) and (2) can be generalized if the ratio E_{ex}/E_F is arbitrary. Then, for example, $\Phi = \mathrm{Im}d_F\{\sqrt{2m(E_F + i\omega + E_{ex}\sigma)} - \sqrt{2m(E_F - i\omega - E_{ex}\sigma)}\}$, β can be written in a similar way. The ω dependence of Φ was neglected in [7–9] because, there, d_F was much smaller than ξ_0. Physically, the ballistic model of an SFS junction could be realized, for example, in gated heterostructures [14] or in the break junctions [15] in an external magnetic field producing Zeeman splitting of Andreev levels [16].

The case $a = 0$ (then, the scattering potential of the junction is symmetric), $d_F \lesssim \xi = \hbar v_F/\Delta$ was considered in papers [7–9]. This model is important because, on a qualitative level, it describes SFS junctions well where F is a ferromagnetic granule or a spin-active interface (see [7] and references therein). It was shown that, if $d_F \approx d_F^{(1)}$, $\beta < 1$, and one fixes E_{ex} and changes the temperature, then the π state of a ballistic SFS junction usually appears at higher temperatures than the 0 state. The opposite phenomenon appears at $d_F \approx d_F^{(1)}$ if the junction is dirty and there is no other scattering potential in the junction than the impurity potential. (I make this statement after solving self-consistently Eilenberger quasi-classical equations with impurities and analyzing Josephson current evolution with temperature in wide range of parameters.) To illustrate this point of view, I consider the Josephson current in two similar SFS junctions with the same dimensionless normal conductance per channel, the same Δ, E_{ex}, and the same number of open channels, etc. The only difference between the junctions is that, in the first one, the normal conductance is provided by an insulator layer with a flat surface at the center of the ferromagnet as in Fig. 1 and, in the second one, by nonmagnetic impurities in the ferromagnetic region. The following parameters were chosen: $d_F = \xi_0 = \hbar v_F/\Delta_0$, $\Delta_0 = \Delta(T = 0)$; $\Theta = 2d_F E_{ex}/\pi\xi_0\Delta_0 = 0.18$. The disorder strength in the second junction was $\Delta_0/\tau = 10$, where τv_F is the mean free path. The transmission probability of the insulator layer in the first junction was $D(\theta) = D_0\cos^2\theta/(1 - D_0 + D_0\cos^2\theta)$, where $D_0 = 0.127$. The current scale is $I_0 = N_{ch}e\Delta_0/\hbar$, where N_{ch} is the number of open channels in the junction. The thick curve in Fig. 2a corresponds to the same $\Theta = 0.18$ as in Fig. 2b; the other curve in Fig. 2a corresponds to $\Theta \approx 0.5$. Note that $d_F \approx d_F^{(1)}$ in Fig. 2. It is seen that the π state in the ballistic SFS junction is at higher temperatures than the 0 state; the opposite phenomenon takes place in dirty SFS junctions. If there is an insula-

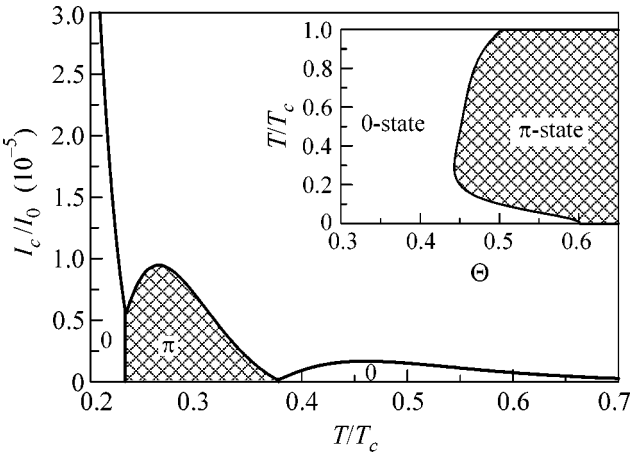

Fig. 3. Critical current–temperature relation in a long $d_f \approx 3\xi_0$ ballistic SFS junction with $D_0 = 0.127$, $\Theta \approx 0.445$. The inset shows the "phase diagram" of the junction. If impurities were added to this type of junction, then the phase diagram would finally look as in Fig. 2b. If I make $D_0 \approx 1$ (see Fig. 4), then the phase diagram will become similar to the phase diagram shown in Fig. 2b.

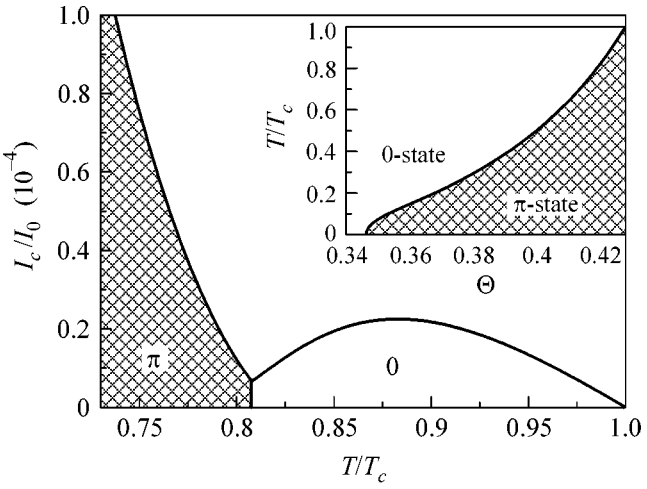

Fig. 4. Critical current–temperature relation in a long $d_f \approx 3\xi_0$ ballistic SFS junction with $D_0 = 1$, $\Theta \approx 0.42$. The inset shows the "phase diagram" of the junction. The phase diagram (and the current temperature relation) in a short dirty SFS junction (Fig. 2b) looks quite similar to the one shown in Fig. 5.

tor barrier in a ballistic short SFS junction and we add nonmagnetic impurities to it, the transition from the case shown in Fig. 2a to the case shown in Fig. 2b is expected to occur when $l/d_F \sim D$, where l is a mean free path. Josephson current calculations in ballistic junctions were performed using Eqs. (1)–(3) with $t_\uparrow = t_\downarrow = \sqrt{D}$; in dirty junctions, using the Ricatti form of the Eilenberger quasi-classical equations [17].

A "short" SFS junction with $d_F \lesssim \xi_0$ was considered above. What may happen if $d_F > \xi_0$ is illustrated in Fig. 3. The junction is ballistic (with the same normal conductance corresponding to $D_0 = 0.127$), and $d_F \approx 3\xi_0$. The inset shows the "phase diagram" of the junction. Hence, by freezing the long SFS junction (in the proper range of E_{ex}) starting from T_c, one can go through a sequence of phase transitions: $0 \longrightarrow \pi \longrightarrow 0$. In general, one can make a junction phase diagram similar to any of the phase diagrams depicted in Figs. 1–3 by the proper choice of the position of the insulator barrier and the length of the junction. For example, if I make $D_0 = 1$, then the phase diagram in Fig. 1 will transform to the phase diagram shown in Fig. 2b (the junction is ballistic!). This is shown in Fig. 4. The same transformation of the phase diagram occurs due to impurities as shown by the numerical calculations.

Below, a short description of the numerical calculation procedure that was used for creation of Fig. 2b is given. The calculations were performed using the Ricatti representation of the Eilenberger quasi-classical equations (because Eilenberger equations are unstable) [17]. The quasi-classical Green's functions can be parameterized via the new functions a and b; therefore,

$$f = \frac{2a}{1+ab}\operatorname{sgn}\omega, \quad g = \frac{1-ab}{1+ab}\operatorname{sgn}\omega. \tag{3}$$

The amplitudes a and b change according to the Ricatti equations

$$\begin{aligned} \mathbf{v}_F\nabla a + 2\omega_R a + \tilde{\Delta}_R a^2 - \Delta_R &= 0, \\ \mathbf{v}_F\nabla b - 2\omega_R b - \Delta_R b^2 + \tilde{\Delta}_R &= 0, \end{aligned} \tag{4}$$

where $\Delta_R = \Delta + \langle f\rangle/2\tau$, $\tilde{\Delta}_R = \Delta^* + \langle \tilde{f}\rangle/2\tau$, and $\omega_R = \omega_n + i\sigma E_{ex} + \langle g\rangle/2\tau$. Here, $\langle\ldots\rangle$ denotes averaging over the directions of the quasi-classical trajectories, and τ is the mean free path of an electron in the impurity potential. Equations (4) were solved numerically self-consistently; the Josephson current density was evaluated as follows:

$$j = -i\pi e\nu T\sum_\omega\sum_\sigma \langle \mathbf{v}_F g\rangle_{\mathbf{v}_F}, \tag{5}$$

where ν is the normal density of states. I tried to expand the Ricatti equations over τ^{-1} in the first order to find analytically how disorder influences the phase diagram of a short SFS junction. My calculations showed no effect in the first order.

The discussion above may lead to the conclusion that, in dirty Josephson junctions with ferromagnet layers between superconductors, the phase diagram always looks similar to Fig. 2b. It seems that this statement is true for short SFS junctions when E_{ex} is not too large, but it is not true in general. To prove it, I shall give below an example (more examples and a detailed discussion will be given in the extended version of this letter). Consider a dirty SFIFS junction (e.g., as in

Fig. 1). The Josephson current can be found from Usadel equations [17]. In general, Usadel equations are nonlinear over quasi-classical Green's functions. But, near the critical temperature of the junction or if the superconductors and ferromagnets are weakly coupled in some sense, the Usadel equations can be linearized. Then, the linearized Usadel equations in the ferromagnets for an anomalous function f look similar to

$$\partial^2 f - \frac{2|\omega| + 2iJ_{1,2}\sigma\,\mathrm{sgn}\,\omega}{D_{1,2}} f = 0, \qquad (6)$$

where $D_{1,2}$ is the diffusion constant and $J_{1,2}$ are the exchange energy in the left (right) ferromagnetic layer. If the magnetizations of the ferromagnetic layers are collinear, then the f function to the left of the insulator layer I (see Fig. 1) is $f = \frac{1}{\sqrt{|\kappa_1/\rho_1|}}(Ae^{\kappa_1 x} + Be^{-\kappa_1 x})$, and to the left, $f = \frac{1}{\sqrt{|\kappa_2/\rho_2|}}(Ce^{\kappa_2 x} + De^{-\kappa_2 x})$. Here, $\kappa_{1,2} = \sqrt{(|\omega| + 2iJ_{1,2}\sigma\,\mathrm{sgn}\,\omega)/D_{1,2}}$, where $\rho_{1,2}$ is the resistivity of the ferromagnets. The amplitudes A, B, and … are not independent, but they are connected by boundary conditions [18] that I write here in the matrix form:

$$\begin{pmatrix} B \\ C \end{pmatrix} = S \begin{pmatrix} A \\ D \end{pmatrix}, \qquad (7)$$

$$S = \begin{pmatrix} e^{2\kappa_1 a}\dfrac{\tilde\kappa_1 - \tilde\kappa_2 - \tilde\kappa_1\tilde\kappa_2 R}{\tilde\kappa_1 + \tilde\kappa_2 - \tilde\kappa_1\tilde\kappa_2 R} & e^{(\kappa_1-\kappa_2)a}\dfrac{\sqrt{\tilde\kappa_1\tilde\kappa_2}}{\tilde\kappa_1 + \tilde\kappa_2 - \tilde\kappa_1\tilde\kappa_2 R} \\ e^{(\kappa_1-\kappa_2)a}\dfrac{\sqrt{\tilde\kappa_1\tilde\kappa_2}}{\tilde\kappa_2 + \tilde\kappa_1 - \tilde\kappa_1\tilde\kappa_2 R} & e^{-2\kappa_2 a}\dfrac{\tilde\kappa_2 - \tilde\kappa_1 - \tilde\kappa_1\tilde\kappa_2 R}{\tilde\kappa_2 + \tilde\kappa_1 - \tilde\kappa_1\tilde\kappa_2 R} \end{pmatrix}, \qquad (8)$$

where S is the "scattering matrix" of the F–F boundary (the diagonal elements of S play the role of "reflection" amplitudes; the off-diagonal, "transmission" amplitudes).

Here, $\tilde\kappa_{1,2} = \kappa_{1,2}/\rho_{1,2}$; R is the resistance of the F–F boundary. When $R = 0$, the scattering matrix S is similar to the quantum mechanical scattering matrix of a potential step. At the SF interface, the boundary conditions resemble

$$\begin{pmatrix} A \\ D \end{pmatrix} = S_b \begin{pmatrix} B \\ C \end{pmatrix} - \boldsymbol{\Delta}_{\mathrm{eff}}, \qquad (9)$$

$$S_b = \begin{pmatrix} e^{2\kappa_1 d_F} & 0 \\ 0 & e^{2\kappa_2 d_F} \end{pmatrix}, \qquad (10)$$

$$\boldsymbol{\Delta}_{\mathrm{eff}} = \begin{pmatrix} \Delta_L e^{\kappa_1 d_F}/\Omega R_L \\ \Delta_R e^{\kappa_2 d_F}/\Omega R_r \end{pmatrix}, \qquad (11)$$

where $\Delta_{L(R)} = \Delta\exp(\pm i\phi/2)$ are the gaps of the left (right) superconductors and $\Omega = \sqrt{|\Delta|^2 + \omega^2}$, $R_{L(r)}$ are the resistances of the SF boundaries. From Eqs. (7)–(11), I obtain

$$\begin{pmatrix} A \\ D \end{pmatrix} = (S_b S - 1)^{-1}\boldsymbol{\Delta}_{\mathrm{eff}}. \qquad (12)$$

The approach applied above is similar to the scattering matrix method used in [12] for calculation of the Josephson current in SNS junctions. Then, the Josephson current density can be found: $j = \frac{\sigma_N \pi i}{2e} T\sum_\omega \mathrm{Tr}\,\{\tilde f \partial f - f\partial\tilde f\}$, where Tr is taken over spin degrees of freedom and $\tilde f(\omega) = f^*(-\omega)$. Figure 5 shows the critical current–temperature dependence in the dirty SFIFS junction with the following parameters: $J_1 = -1.9T_c$, $J_2 = 3T_c$, $d_F/\xi = 1$, $a/\xi = -0.2$, $D_1 = D_2$ ($\xi = \sqrt{D/T_c}$) $R/\rho_1\xi = 0.1$. Linearization of the Usadel equa-

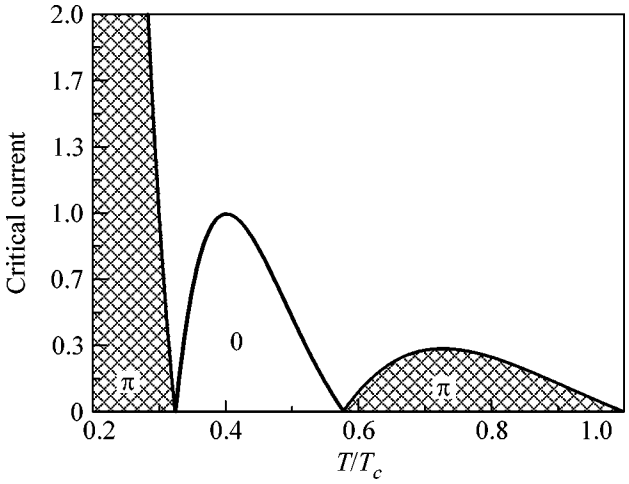

Fig. 5. Critical current–temperature dependence in a dirty SFIFS junction with the following parameters: $J_1 = -1.9T_c$, $J_2 = 3T_c$, $d_F/\xi = 1$, $a/\xi = -0.2$, $D_1 = D_2$ ($\xi = \sqrt{D/T_c}$), $R/\rho_1\xi = 0.1$. The critical current is normalized on its value in the maximum of $I_c(T)$ corresponding to the 0 state.

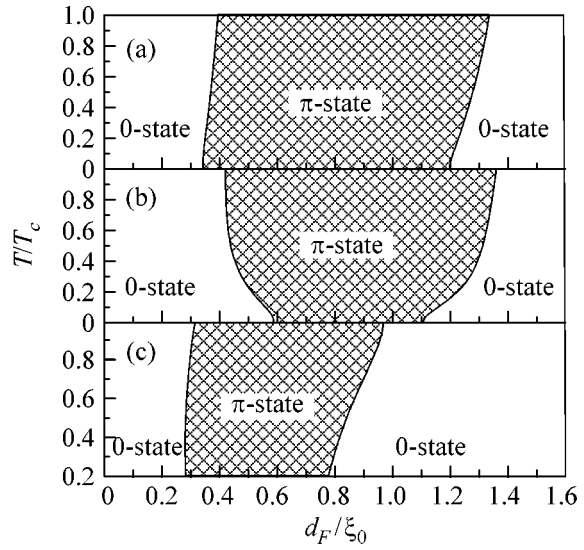

Fig. 6. This figure illustrates how the geometry of an SFS junction and disorder could influence the shape of the phase diagram. In all the figures, $2E_{ex}/\pi\Delta_0 = 1$. The first and the second diagrams (a, b) correspond to ballistic SFS junctions described by Eqs. (1) and (2) with $D_0 = 1$ (no layer I in Fig. 1) and $D_0 = 0.127$, respectively, and $a = 0$. The role of impurities can be seen in (c). There, $D_0 = 1$ and $\hbar/\Delta_0\tau = 10$. At $d_F/\xi_0 = 1$, the normal conductance of the junction in (c) becomes equal to the normal conductance of the junction shown in (a). If I drew the phase diagrams for the SFS junctions in Θ, T_c space, they would look similar to as in the figure.

tions is correct at these parameters. Figure 5 is similar to Fig. 3 corresponding to a ballistic SFS junction.

The phase diagrams were considered above in $(T, \Theta) \sim (T, E_{ex})$ space at fixed d_F. If one fixes E_{ex} near the first cusp of $I_c(E_{ex})$ and changes d_F, one will obtain similar figures.

Above, I considered only phase diagrams of SFS junctions near the first cusp of $I_c(d_F)$ (at $d_F \approx d_F^{(1)}$). Below, I will briefly discuss the phase diagram in the general case. Figure 6 shows three phase diagrams. In all the figures, $2E_{ex}/\pi\Delta_0 = 1$. The first and the second diagrams (Figs. 6a, 6b) correspond to the ballistic SFS junctions described by Eqs. (1) and (2) with $D_0 = 1$ (there is no layer I in Fig. 1) and $D_0 = 0.127$, respectively. The role of impurities can be seen in Fig. 6c. There, $D_0 = 1$ and $\hbar/\Delta_0\tau = 10$. At $d_F/\xi_0 = 1$, the normal conductance of the junction in Fig. 6c becomes equal to the normal conductance of the junction shown in Fig. 6a. If I use the linearized Usadel equations to describe the phase diagram of an SFS junction, I should get a graph resembling that in Fig. 6c. The phase diagram in Fig. 6c qualitatively agrees with the experimental results in [5], which state that the order of the π and 0 phases with respect to the temperature is one at $d_F \approx d_F^{(1)}$ and the opposite at $d_F \approx d_F^{(2)}$.

In conclusion, π–0 transitions in Josephson junctions with ferromagnetic layers are investigated in this letter. It is shown that the phase diagram is very sensitive to the geometry of the system, in particular, to the amount of disorder in the junction.

ACKNOWLEDGMENTS

I am grateful to I.S. Burmistrov; A.S. Iosselevich; and, especially, Yu.S. Barash for stimulating discussions. This work was supported by the Russian Foundation for Basic Research (project nos. 03-02-16677, 04-02-08159, and 02-02-16622), the Russian Ministry of Science, the Netherlands Organization for Scientific Research (NWO), the CRDF, the Russian Science Support Foundation, and the State Scientist Support Foundation (project no. 4611.2004.2).

REFERENCES

1. L. N. Bulaevskii, V. V. Kuzii, and A. A. Sobyanin, Pis'ma Zh. Éksp. Teor. Fiz. **25**, 314 (1977) [JETP Lett. **25**, 290 (1977)].
2. A. V. Andreev, A. I. Buzdin, and R. M. Osgood, Phys. Rev. B **43**, 10124 (1991).
3. A. I. Buzdin, B. Vujicic, and M. Yu. Kupriyanov, Zh. Éksp. Teor. Fiz. **101**, 231 (1992) [Sov. Phys. JETP **74**, 124 (1992)].
4. A. V. Veretennikov, V. V. Ryazanov, V. A. Oboznov, *et al.*, Physica B (Amsterdam) **284–288**, 495 (2000); V. V. Ryazanov, V. A. Oboznov, A. Yu. Rusanov, *et al.*, Phys. Rev. Lett. **86**, 2427 (2001).
5. V. V. Ryazanov, V. A. Oboznov, A. S. Prokofiev, *et al.*, J. Low Temp. Phys. **136**, 385 (2004).
6. T. Kontos, M. Aprili, J. Lesueur, *et al.*, Phys. Rev. Lett. **89**, 137 007 (2002).
7. M. Fogelström, Phys. Rev. B **62**, 11812 (2000).
8. N. M. Chtchelkatchev, W. Belzig, Yu. V. Nazarov, and C. Bruder, Pis'ma Zh. Éksp. Teor. Fiz. **74**, 357 (2001) [JETP Lett. **74**, 323 (2001)].
9. Yu. S. Barash and I. V. Bobkova, Phys. Rev. B **65**, 144502 (2002).
10. Z. Radovic, N. Lazarides, and N. Flytzanis, Phys. Rev. B **68**, 014501 (2003).
11. A. A. Golubov, M. Yu. Kupriyanov, and Ya. V. Fominov, Pis'ma Zh. Éksp. Teor. Fiz. **75**, 223 (2002) [JETP Lett. **75**, 190 (2002)].
12. C. W. J. Beenakker, Phys. Rev. Lett. **67**, 3836 (1991).
13. A. Furusaki, H. Takayanagi, and M. Tsukada, Phys. Rev. Lett. **67**, 132 (1991); Phys. Rev. B **45**, 10563 (1992).
14. H. Takayanagi, T. Akazaki, and J. Nitta, Phys. Rev. Lett. **75**, 3533 (1995).
15. E. Scheer, N. Agrait, J. C. Cuevas, *et al.*, Nature **394**, 154 (1998).
16. S. K. Yip, Phys. Rev. B **62**, R6127 (2000).
17. W. Belzig, F. K. Wilhelm, C. Bruder, *et al.*, Superlattices Microstruct. **25**, 1251 (1999).
18. M. Yu. Kupriyanov and V. F. Lukichev, Zh. Éksp. Teor. Fiz. **94**, 139 (1988) [Sov. Phys. JETP **67**, 1163 (1988)].

JETP Letters, Vol. 80, No. 12, 2004, pp. 748–751. Translated from Pis'ma v Zhurnal Éksperimental'noĭ i Teoreticheskoĭ Fiziki, Vol. 80, No. 12, 2004, pp. 880–883.

Inverted EPR Signal from Nitrogen Defects in a Synthetic Diamond Single Crystal at Room Temperature

N. A. Poklonski, N. M. Lapchuk, and T. M. Lapchuk

Belarussian State University, Minsk, 220050 Belarus

e-mail: poklonski@bsu.by

Received November 9, 2004

Electron paramagnetic resonance (EPR) in diamond single crystals was studied. The crystals were grown using apparatuses of the "split-sphere" type in a Ni–Fe–C system using the temperature gradient method with a subsequent high-temperature high-pressure treatment. It was found that, after the high-temperature high-pressure treatment of a diamond sample, the EPR signal from the lattice defects containing nitrogen atoms became inverted with the growth of the microwave power in an H_{102} resonator. In a constant polarizing magnetic field, when the microwave power applied to the diamond was low, a resonance absorption by the nitrogen defects took place, whereas, when the microwave power was high, an emission was observed. The inversion of the EPR lines of a single nitrogen atom substituting for a carbon atom at a diamond lattice site could be caused by the presence of a nickel atom with an uncompensated magnetic moment at the adjacent tetrahedral interstitial site. In synthetic diamond crystals that were not subjected to high-temperature high-pressure treatment, the inversion of the EPR signal from nitrogen atoms (P1 centers, nitrogen in the C form) was absent. © *2004 MAIK "Nauka/Interperiodica".*

PACS numbers: 76.30.–v; 84.40.Ik

In solid-state masers (paramagnetic amplifiers), the working medium is usually cooled down to cryogenic temperatures [1]. Diamond crystals have never been considered as a promising working medium for masers (see, e.g., reviews [2–5]).

An inverted population of spin levels (an inverted EPR signal) in thermally treated oxygen-containing silicon crystals [6] and maser radiation in a ruby [7] were observed at liquid helium temperatures. We note that the inversion of the EPR signal by paramagnetic centers of a Si crystal surface was detected only with an interband illumination at liquid-nitrogen temperature [8]. The optically induced inversion of the EPR signal in Ib-type diamond crystals was observed at cryogenic temperatures under illumination with a photon energy lower than the energy gap [9, 10].

Under normal conditions (at room temperature in air in the dark), the weakly pronounced inversion of the EPR signal was observed in polycrystalline diamond films grown on silicon crystals by chemical gas-phase deposition from a methane–hydrogen mixture [11]. (In one of the EPR spectra presented in [12] for natural diamond crystals at room temperature, one can notice hints of the inversion of some of the resonance paramagnetic absorption lines.) The results of these studies suggest that one can obtain an inverted population of spin levels in synthetic diamond single crystals, for which the type of impurity-defect associates (and their paramagnetic relaxation times [13]) can be controlled to a certain extent.

EXPERIMENT

By the EPR method, we studied two synthetic diamond single-crystal samples (a half-octahedron in the form of a square pyramid) with a mass of ≈0.5 carat each. The diamonds were grown in an apparatus of the split-sphere type (the Adamas enterprise at Belarussian State University) in the Ni–Fe–C system by the temperature gradient method at temperatures of 1750 to 1800 K under pressures of 5.4–5.5 GPa.

Diamond sample 1 (the initial sample) had paramagnetic and optical properties typical of crystals grown by the aforementioned method. The concentration of single paramagnetic nitrogen atoms at the diamond lattice sites (in the C form) was on the order of 3×10^{19} cm^{-3}.

Diamond sample 2 was subjected to high-temperature high-pressure treatment for 12 h under a pressure of 6.8 GPa at a temperature of 2250 K. (Before this treatment, the properties of samples 1 and 2 were identical.) The high-temperature high pressure treatment of the diamond changed its color from light brown to yellow green. The optical properties of such crystals were described in [14], where it was found that, as a result of high-temperature high-pressure treatment, the residual Ni (metal catalyst) that was present in the synthetic diamond "reacted" with nitrogen.

The EPR spectra of samples 1 and 2 were recorded at room temperature in the dark in air by a RadioPAN SE/X-2543 spectrometer with an H_{102} resonator (a frequency of 9.311 GHz) with a modulation (a frequency

0021-3640/04/8012-0748$26.00 © 2004 MAIK "Nauka/Interperiodica"

of 100 kHz and an amplitude of 0.1 mT) of the polarizing magnetic field; the sensitivity of the spectrometer was $\approx 3 \times 10^{12}$ spin/mT. The induction of the polarizing magnetic field was measured by an NMR magnetometer, and the frequencies in the microwave resonator, by a frequency meter. For the purposes of controlling the resonator quality factor, tuning the phase of the magnetic field modulation, and calibrating the H_1 component of the microwave radiation, we used a ruby crystal (Al_2O_3:Cr) fixed on the wall of the resonator. The diamond samples under investigation were placed at the center of the H_{102} resonator.

We used a standard way of recording the EPR spectra with an automatic klystron frequency control by the measuring H_{102} resonator. The choice of the modulation amplitude and measuring time constant was determined by the known requirement that the first derivative of the resonance absorption signal with respect to the magnetic induction be undistorted in the course of the measurement [15]. By varying the time of recording of each single EPR spectrum from 1 to 30 min, we noticed no considerable changes in the shape of the resulting spectra for sample 1, as well as for sample 2. The nonresonance absorption of microwave radiation by samples 1 and 2 was negligibly small.

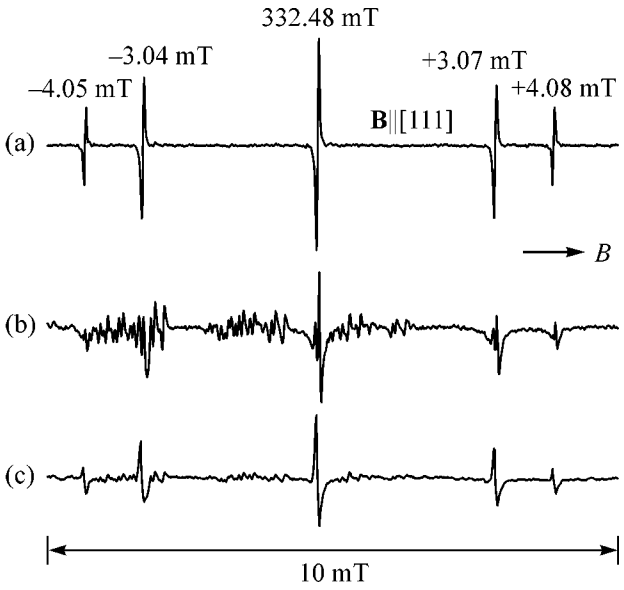

Fig. 1. EPR spectra of sample 2 of a synthetic diamond single crystal at a temperature of 300 K for three levels of microwave power: (a) 70 μW, (b) 7 mW, and (c) 70 mW; the magnetic induction vector **B** is parallel to the [111] crystallographic direction; the microwave radiation frequency is 9.311 GHz. The shifts of the low-field (–) and high-field (+) satellites with respect to the central line are indicated in the plot (g = 2.00225; a width of 0.12 mT).

RESULTS AND DISCUSSION

The EPR spectrum of sample 1 (similar to the spectrum of sample 2 shown in Fig. 1a) exhibits a characteristic signal from a P1 paramagnetic center (i.e., C center) represented by a nitrogen atom substituting for a carbon atom in the diamond lattice. The g factor of the central line of the EPR spectrum is equal to 2.00221 mT, and the width is 0.17 mT. For an arbitrary orientation of the induction **B** of the polarizing magnetic field with respect to the crystallographic directions in the diamond, symmetrically positioned low-field (–) and high-field (+) satellites of the central EPR line of the P1 center are observed (±3.07 and ±4.08 mT for **B** ∥ [111]).

Note that, when the microwave power exceeds 3 mW, the EPR spectrum of sample 1 exhibits two additional lines (at ±1.5 mT with reference to the central line of the spectrum), which are caused by the exchange interaction between nitrogen atoms when their concentration is high ($>2 \times 10^{18}$ cm^{-3}) [16].

Thus, for the initial diamond sample 1, we have a spectrum of P1 centers that is in good agreement with the literature data [16–18]. As is known [18], the EPR spectrum of these centers is formed by the hyperfine interaction between an unpaired electron and a ^{14}N nitrogen nucleus with a spin equal to unity.

From studying sample 2 under the same conditions, we have found that (Fig. 1) an increase in the level of the microwave power supplied to the sample leads to an inversion of the EPR spectrum lines. This inversion is caused by the population inversion in the spin system (paramagnetic centers of the P1 type) and is unrelated to the conditions of passing through the resonance. At a low power (70 μW), the uninverted signal is symmetric, whereas, at a high power (70 mW), an asymmetry of the inverted EPR signals (both the central line and its satellites) is observed.

We have also found that, when the induction **B** of the external polarizing magnetic field is perpendicular to the (111) plane, the low-field lines (satellites) of the EPR spectrum of sample 2 lie 0.03 mT closer to the central line than the corresponding lines observed for the initial sample 1 (see Fig. 1a).

Note that, in sample 2, as in sample 1, the signal from exchange-coupled pairs of nitrogen atoms manifests itself only when the microwave power exceeds 3 mW. However, in sample 2 subjected to high-temperature high-pressure treatment, unlike the initial sample 1, the EPR signals from exchange-coupled pairs of nitrogen atoms manifest themselves only when the induction of the magnetic field is parallel to the (100) plane of the crystal. In addition, in sample 2, the amplitude of the high-field EPR line of the exchange-coupled pairs is approximately twice as great as the amplitude of the low-field line irrespective of the microwave power.

Figure 2 shows the amplitude A of the EPR signal from nitrogen (P1 centers) as a function of the strength H_1 of the magnetic component of the microwave radiation in the H_{102} resonator for samples 1 and 2. The signal from the P1 centers exhibits a saturation with increasing microwave power, and this saturation occurs

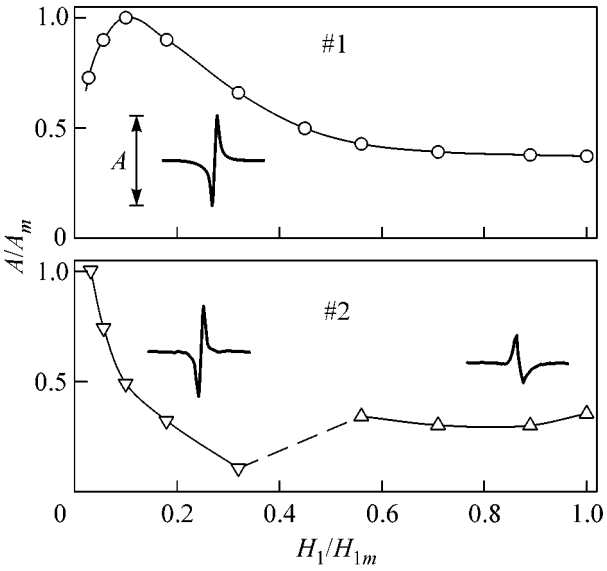

Fig. 2. Amplitude A of the central EPR line (normalized to its maximal value A_m) for sample 1 (the initial one) and sample 2 (subjected to high-temperature high-pressure treatment) vs. the strength H_1 of the magnetic component of the microwave field in the H_{102} resonator; the value of H_{1m} corresponds to a microwave power of 70 mW.

in different ways in the two samples, which means that the paramagnetic relaxation times [19] in these samples are different.

The mechanisms of the aggregation of nickel, iron, and nitrogen atoms and atomic lattice defects in synthetic diamond are still not clearly understood (see, e.g., [20–25]). Therefore, in discussing the results of our measurements, we use model representations.

Presumably, the inversion of the EPR signal in the diamond sample 2 subjected to high-temperature high-pressure treatment is related to the interaction of single N atoms located at the diamond lattice sites with Ni atoms located at the tetrahedral interstitial sites adjacent to them. The magnetic field of a Ni atom (with an uncompensated magnetic moment, which, however, does not show any EPR activity in the magnetic field region where the signal from the P1 centers is observed) shifts the low-field satellites of the central line of P1 centers by 0.03 mT toward greater values of magnetic induction. In this case, a spin–spin correlation manifests itself; i.e., the magnetic moment of the Ni atom, being oriented along the direction of the external polarizing magnetic field, "stabilizes" the opposite orientation of the unpaired spin of the nitrogen atom (P1 center) after the resonance absorption of microwave radiation by the nitrogen atom takes place. The correlation between the magnetic moments of N and Ni atoms possibly suppresses the spin relaxation of the unpaired electron of the nitrogen atom (see [26–28]). Thus, in the EPR measurements, the magnetic field of the nickel atom not only locally screens the external polarizing magnetic field but also increases the life time of the upper spin level of the nitrogen atom located near the nickel atom. Therefore, the low-field satellites of the central line of a P1-type paramagnetic center are observed at a higher magnetic induction (see Fig. 1) as compared to the case where the effect of nickel on the P1 center can be ignored. (The effect of the magnetic moment of the Ni atom on the high-field satellites of the central EPR line of the P1 center is less pronounced.) This interpretation of our results is indirectly supported by the results reported in [25]: it was found that, in a synthetic diamond crystal, Ni atoms are EPR-active in the region of magnetic induction values lower than those characteristic of P1 centers; i.e., the total magnetic moment of a Ni atom is greater than the magnetic moment of a nitrogen atom at a diamond lattice site. In principle, in the diamond lattice, Fe or Co atoms could play the role of Ni atoms. However, presumably, in the diamond subjected to high-temperature high-pressure treatment, only Ni atoms have the crystal chemical prerequisites (see, e.g., [18]) to be dissolved rather than to be pushed out to the surface of the single crystal or to form inclusions.

We are grateful to G.A. Gusakov for discussing the problems of the synthesis and characterization of diamond single crystals. This work was supported by the program "Low-Dimensional Systems" of the Ministry of Education of the Republic of Belarus.

REFERENCES

1. N. T. Cherpak, *Distributed-Type Quantum Amplifiers (Masers) in the Microwave Waveband* (Naukova Dumka, Kiev, 1996) [in Russian].
2. M. P. Vaĭsfel'd, Zh. Éksp. Teor. Fiz. **89**, 1280 (1985) [Sov. Phys. JETP **62**, 741 (1985)].
3. R. J. Trew, J.-B. Yan, and P. M. Mock, Proc. IEEE **79**, 598 (1991).
4. V. S. Vavilov, Usp. Fiz. Nauk **167**, 17 (1997) [Phys. Usp. **40**, 15 (1997)].
5. Special Issue on Wide Bandgap Semiconductor Devices, Proc. IEEE **90** (6) (2002).
6. V. M. Babich, N. P. Baran, A. A. Bugaĭ, *et al.*, Pis'ma Zh. Éksp. Teor. Fiz. **44**, 513 (1986) [JETP Lett. **44**, 660 (1986)].
7. A. I. Stetsenko and N. T. Cherpak, Pis'ma Zh. Tekh. Fiz. **7**, 105 (1981) [Sov. Tech. Phys. Lett. **7**, 45 (1981)].
8. V. V. Kurylev and S. N. Karyagin, Phys. Status Solidi A **21**, K127 (1974).
9. J. H. N. Loubser and J. A. van Wyk, Rep. Prog. Phys. **41**, 1201 (1978).
10. J. Harrison, M. J. Sellars, and N. B. Manson, J. Lumin. **107**, 245 (2004).
11. N. M. Lapchuk, N. A. Poklonskiĭ, S. A. Vyrko, *et al.*, in *Abstracts of VIII International Conference, Sudak, Crimea, 2003* (IHSE, Kiev, 2003), p. 792.
12. M. Ya. Scherbakova, E. V. Sobolev, and V. A. Nadolinnyĭ, Dokl. Akad. Nauk SSSR **204**, 851 (1972) [Sov. Phys. Dokl. **17**, 513 (1972)].

13. E. C. Reynhardt, G. L. High, and J. A. van Wyk, J. Chem. Phys. **109**, 8471 (1998).
14. A. V. Mudryĭ, T. P. Larionova, I. A. Shakin, *et al.*, Fiz. Tekh. Poluprovodn. (St. Petersburg) **38**, 538 (2004) [Semiconductors **38**, 520 (2004)].
15. J. A. Weil, J. R. Bolton, and J. E. Wertz, *Electron Paramagnetic Resonance—Elementary Theory and Practical Applications* (Wiley, New York, 1994).
16. J. H. N. Loubser, W. P. van Ryneveld, and L. du Perez, Solid State Commun. **3**, 307 (1965).
17. W. V. Smith, P. P. Sorokin, I. L. Gelles, and G. J. Lasher, Phys. Rev. **115**, 1546 (1959).
18. *The Properties of Natural and Synthetic Diamonds*, Ed. by J. E. Field (Academic, London, 1992).
19. R. C. Barklie and J. Guven, J. Phys. C: Solid State Phys. **14**, 3621 (1981).
20. Y. V. Babich, B. N. Feigelson, and A. P. Yelisseyev, Diamond Relat. Mater. **13**, 1802 (2004).
21. A. Yelisseyev, S. Lawson, I. Sildos, *et al.*, Diamond Relat. Mater. **12**, 2147 (2003).
22. K. Bharuth-Ram and M. F. Hansen, Physica B (Amsterdam) **321**, 29 (2002).
23. A. T. Collins, Diamond Relat. Mater. **9**, 417 (2000).
24. R. N. Pereira, W. Gehlhoff, A. J. Neves, and N. A. Sobolev, J. Phys.: Condens. Matter **15**, 2493 (2003).
25. R. I. Mashkovtsev and Yu. N. Pal'yanov, Solid State Commun. **111**, 397 (1999).
26. L. A. Shul'man, V. K. Bezobchuk, and A. B. Brik, Fiz. Tverd. Tela (Leningrad) **24**, 1488 (1982) [Sov. Phys. Solid State **24**, 849 (1982)].
27. K. A. Kikoin and V. N. Fleurov, *Transition Metal Impurities in Semiconductors: Electronic Structure and Physical Properties* (World Sci., Singapore, 1994).
28. P. Fulde, *Electron Correlations in Molecules and Solids* (Springer, Berlin, 2002).

Translated by E. Golyamina

JETP Letters, Vol. 80, No. 12, 2004, pp. 752–756. Translated from Pis'ma v Zhurnal Éksperimental'noĭ i Teoreticheskoĭ Fiziki, Vol. 80, No. 12, 2004, pp. 884–888.

Spectrum of Gases Liberated upon the Stepwise Heating of Single-Walled Carbon Nanotubes Deuterated under Pressure

Yu. M. Shulga[1], I. O. Bashkin[2], A. V. Krestinin[1], V. M. Martynenko[1], G. I. Zvereva[1], I. V. Kondratieva[2], Yu. A. Ossipyan[2], and E. G. Ponyatovsky[2]

[1] *Institute of Problems of Chemical Physics, Russian Academy of Sciences, Chernogolovka, Moscow region, 142432 Russia*
[2] *Institute of Solid State Physics, Russian Academy of Sciences, Chernogolovka, Moscow region, 142432 Russia*
e-mail: bashkin@issp.ac.ru
Received November 9, 2004

The mass spectra of gases liberated from single-walled carbon nanotubes saturated with deuterium under a pressure of 5 GPa at temperatures up to 500°C (10.8 wt % D) have been measured at different steps of heating to 550°C in a vacuum. Hydrocarbons were found to dominate in the spectra at temperatures up to 400°C, whereas the D_2 and HD molecules became the main components of the spectra at 500–550°C. Changes in the spectra with temperature are consistent with the hypothesis that the major portion of hydrogen in the single-walled carbon nanotubes hydrogenated under pressure and reverted to normal conditions was present in the molecular form. The low temperatures of the hydrocarbon liberation are indicative of lower kinetic barriers in the reaction paths of the hydrocarbon liberation as compared with the liberation of D_2 molecules. Spectral-peak-shape analysis demonstrates the high hydrophilicity of hydrogenated single-walled carbon nanotubes, whereas the sorption of atmospheric oxygen is insignificant as compared with the sorption of water. © *2004 MAIK "Nauka/Interperiodica"*.

PACS numbers: 61.46.+w; 61.48.+c; 62.50.+p; 78.30.Na

Previously [1], samples with a hydrogen content of 6.7–7.0 wt % H were prepared by the thermal treatment of single-walled carbon nanotubes and graphite nanofibers at 450°C and a hydrogen pressure of 9 GPa followed by liquid nitrogen quenching. The measurements of the pressure of a gas evolved into a closed volume on continuously heating the hydrogenated single-walled carbon nanotubes demonstrated that a small portion of the gas (0.45 wt % on a pure hydrogen basis) escaped from the sample at temperatures lower than ~50°C, whereas the liberation of the major portion of gaseous products began at about 500°C and reached a value of 5.6 wt % on a hydrogen basis at 650°C. According to elemental analysis data, after the hydrogenation of single-walled carbon nanotubes under pressure and reversion to normal conditions, the concentration of hydrogen was noticeably higher (6.8 wt % H). Therefore, it was assumed that a portion of the hydrogen could be released on heating as hydrocarbons with an atomic ratio of H/C > 2. The partially and fully degassed products were studied by IR spectroscopy and x-ray diffraction analysis [1]. It was found that covalent C–H bonds in nanostructures hydrogenated under pressure were responsible for the addition of no more than 40% of the absorbed hydrogen. The major portion of hydrogen occurred in the state that was inactive in IR spectra.

The aim of this work was to determine the composition of the gases evolved on heating hydrogenated single-walled carbon nanotubes by mass spectrometry. In addition to information on the character of the gas evolution, these data allow us to reveal the state of the hydrogen in single-walled carbon nanotubes. In this study, we used a heavy isotope of hydrogen (deuterium) for the saturation of single-walled carbon nanotubes in order to decrease and, as far as possible, take into consideration the contribution of the ambient atmosphere and other experimental factors. In contrast to the previous work [1], we reduced the pressure of saturation with hydrogen to 5 GPa.

EXPERIMENTAL PROCEDURE

The carbon nanotubes were synthesized by an electric arc method using a nickel–yttrium catalyst. The primary condensation products containing 10–15 wt % single-walled carbon nanotubes were purified by repeated oxidation in air at temperatures up to 550°C alternated with washing in hydrochloric acid for the removal of amorphous carbon and the metal catalyst. According to microprobe analysis data, the metal impurities in the purified nanotubes were Ni and Y catalysts, as well as Cu and Zn, in the ratio Ni : Y : Cu : Zn = 1 : 1.5 : 0.6 : 0.7. The total metal concentration was no higher than 1 wt %. The incombustible residue upon the combustion of a weighed sample in oxygen was consistent with the total oxide amount to within ±30%. The structures of the condensation and purification products were studied previously using high-resolution electron microscopy, optical microscopy, and optical absorption

0021-3640/04/8012-0752$26.00 © 2004 MAIK "Nauka/Interperiodica"

spectroscopy over the range 200–1400 nm [2, 3]. The sensitivity of the absorption spectra in the near-IR region to the purity of products [3, 4] was used for the quantitative determination of the amount of single-walled carbon nanotubes, which was equal to 80–85 wt % in the test samples of the given batch. According to the electron-microscopic data, graphitized black particles and graphite blocks up to 10–15 μm in size were the main impurities in the material and the nanotubes exhibited a narrow diameter distribution with an average value of 1.5 nm. The nanotubes occurred in the sample in a strongly aggregated state as strands, microcrystal films, and polycrystalline covers.

For the deuterium saturation, a 95-mg sample of single-walled carbon nanotubes and 130 mg of AlD_3 (the source of the deuterium) were placed in a copper ampule and separated with a hydrogen-permeable membrane of palladium foil 0.02 mm in thickness. An anvil cell was used to produce a high pressure. The decomposition of the AlD_3 was performed by heating the ampule to 350°C at a pressure of 1.5 GPa; then, the pressure was increased to the final value of 5 GPa. The single-walled carbon nanotubes were deuterated during a two-step exposure at T = 350°C for 21 h and then at T = 460–490°C for 9 h. Thereafter, the cell was cooled to room temperature and unloaded. The single-walled carbon nanotubes were loaded into and removed from a copper ampule in air; the samples were kept hermetically sealed during the rest of the time before the testing. The hydrogenation procedure was described in more detail in [5], where it was applied to the synthesis of C_{60} hydrofullerenes.

The composition of the deuterated samples was analyzed by the combustion of a weighed portion of 3 mg in a flow of oxygen at 1100°C followed by the gravimetric determination of the resulting CO_2 and D_2O. No correction for hydrogen impurity was made. According to the results of the two tests, the deuterated single-walled carbon nanotubes contained 10.8 ± 0.1 wt % D.

The mass spectra of the gases liberated from the test sample upon heating in a vacuum were measured with the use of an MI 1201V mass spectrometer. A 70-eV electron beam was used for the gas ionization in the ion source of the spectrometer. To obtain the gas phase, a weighed portion of the deuterated single-walled carbon nanotubes (about 80 mg) was placed in a quartz ampule of a pyrolyzer. This ampule was connected to the injection system of the mass spectrometer through a fine control valve. The quartz ampule with the sample was evacuated to a pressure of about 2×10^{-5} Pa in order to remove the surface and weakly bound impurities from the sample. After the evacuation, the ampule was isolated from the vacuum system and the sample was heated to 550°C in five steps. At each of the steps, the sample was kept at a fixed temperature for 3 h; next, the fine control valve was opened and the mass-spectrometric analysis of the gas collected in the ampule was performed. After the analysis, the quartz ampule was again evacuated to a high vacuum, the valve was closed, and the sample was heated to the next temperature. The measurements were performed over the range $1 \le m/z \le 90$, where m is the atomic mass and z is the ion charge. The resolution of the spectrometer was approximately equal to 0.08%.

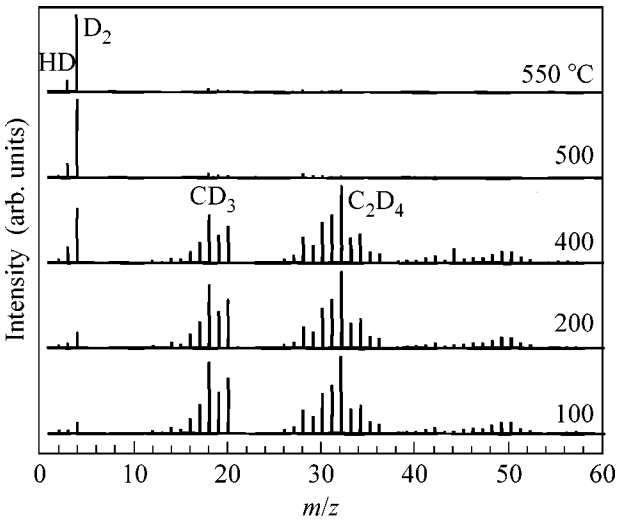

Fig. 1. Mass spectra of the gas phase over a sample of deuterated single-walled carbon nanotubes measured under stepwise heating to specified temperatures. The spectra are restricted to the value of m/z = 60, because the intensities of the peaks due to heavy ions are insignificant. The most intense peaks are identified tentatively (see the text).

RESULTS AND DISCUSSION

Figure 1 shows the mass spectra of gases liberated at various steps during the heating of deuterated single-walled carbon nanotubes. A hydrocarbon mixture was the main constituent of the gas phase at temperatures to 400°C. Both deuterated hydrocarbons (as evidenced by the high intensities of the peaks with m/z = 17–20 and 31–36) and compounds including the light isotope (because peaks with odd mass numbers were present in the spectra) were the constituents of this mixture. The former of these facts implies that the measured spectra describe the properties of the sample rather than the contributions of experimental factors. The latter fact is an indication that the impurities of the light hydrogen isotope or its compounds (which participated in the reactions in the course of the thermal treatment) were present in the parent single-walled carbon nanotubes or in the AlD_3 source of the deuterium.

The presence of a minor impurity of protium in both the parent single-walled carbon nanotubes and AlD_3 was found in special experiments. Because the AlD_3 and the single-walled carbon nanotubes were separated by a Pd membrane in the course of the deuteration, the impurity of the protium or its compounds in the AlD_3 (total concentration of about 2%) did not complicate

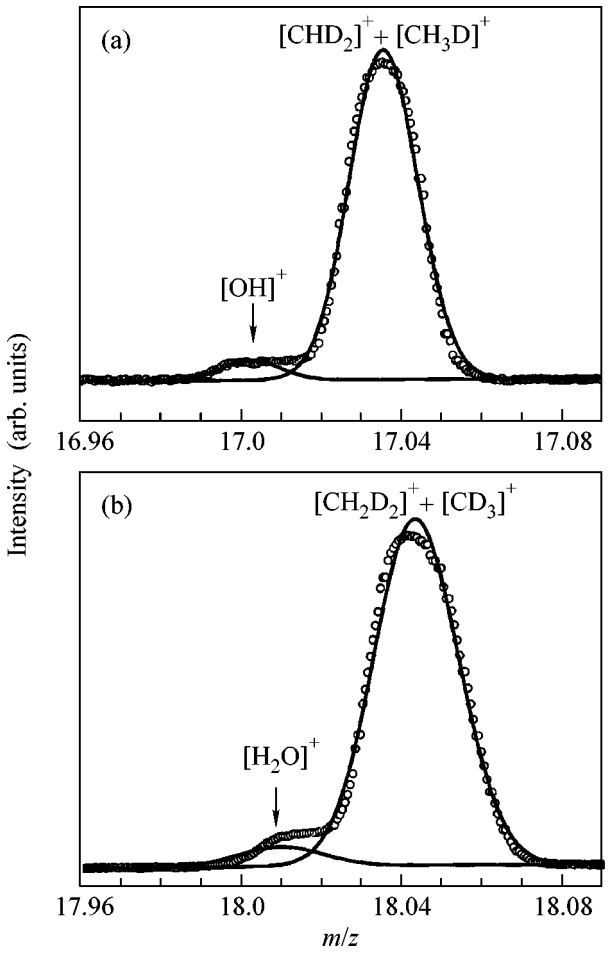

Fig. 2. Peak structures at *m*/*z* = (a) 17 and (b) 18 in the mass spectrum measured upon heating to 100°C.

the interpretation of the spectra in this work. The solvents and gas atmospheres used at the stages of the preparation and purification could have been a source of impurities in the single-walled carbon nanotubes. A peak with *m*/*z* = 31 (corresponding to the $[CH_3O]^+$ ion) exhibited a maximum intensity in the spectrum of the parent single-walled carbon nanotubes; intense peaks with *m*/*z* = 45, 59, and 74 were also detected. The origin of these peaks should be attributed to the fragmentation of diethyl ether. The presence of an acetone impurity also cannot be excluded. Both of the solvents were used at the stage of drying of the single-walled carbon nanotubes. At 200°C or higher, the peaks with *m*/*z* = 44 ($[CO_2]^+$) and 28 ($[CO]^+$) became most intense. In the spectra of deuterated single-walled carbon nanotubes in Fig. 1, the peaks with the above values of *m*/*z* exhibit low or zero intensities. Therefore, impurities of this type can be primarily considered as the source of protium.

The dramatic difference between the compositions of gas mixtures collected below 400°C and at higher temperatures is most pronounced in the spectra shown in Fig. 1. The concentration of D_2 molecules in the gas phase increased as the temperature was increased from 100 to 400°C. In the spectra measured after heating to 500 and 550°C, the peaks with *m*/*z* = 4 and 3 were the most intense peaks. Consequently, D_2 and HD molecules were mainly present in the gas phase at these temperatures. This change in the shape of the spectra with the temperature is consistent with the previous hypothesis [1] that the major portion of the hydrogen was present in the molecular form in the single-walled carbon nanotubes hydrogenated under pressure. Indeed, based on thermodynamic data [6], we can calculate that the $0.47CH_4 : 0.53H_2$ atmosphere with a minor impurity of other hydrocarbons is an equilibrium atmosphere in the C–H system at T = 500°C and a pressure of about 0.1 MPa. If deuterium were attached to carbon fragments by covalent bonds in the samples, it would be expected that the fractions of deuteromethane and D_2 molecules in the high-temperature spectra would be comparable. We experimentally observed that the fraction of CD_4 decreased to almost zero at 500–550°C. This is indirect evidence for not only the absence of covalently bound deuterium but also the almost complete absence of the chemical etching of nanotube walls by deuterium.

Let us consider the structure of the spectra in more detail. Below 400°C, two groups of peaks with maximum group *m*/*z* ratios of 20 and 36, which correspond to deuteromethane and deuteroethane, respectively, can be recognized in the spectra. The peaks with *m*/*z* > 52 (deuteropropane) were insignificant in terms of their intensity. In the first group, two peaks (*m*/*z* = 17 and 18) exhibited a pronounced internal structure, which can be reliably interpreted.

The spectrum near *m*/*z* = 17 (Fig. 2a) is adequately described as a superposition of two Gaussian peaks centered at *m*/*z* = 17.00275 and 17.03598, respectively. The more intense peak was due to $[CHD_2]^+$ ions with the tabulated value of *m*/*z* = *17.03602913* [7, 8] (henceforth, the tabulated values from [7] are italicized). The doubly charged ions $[C_2D_4H_2]^{2+}$ (*17.03602913*) and $[C_2D_5]^{2+}$ (*17.03525555*) can make small contributions as well. The smaller peak corresponds to $[OH]^+$ ions with the tabulated value of *m*/*z* = *17.00274019*. The peak intensity of the $[OH]^+$ ion was about 5% of the base peak intensity. The following conclusion can be drawn from these data: Singly charged $[CHD_2]^+$ ions, which include both deuterium and protium, make the major contribution to the peak with *m*/*z* = 17, because the intensities of the peaks with *m*/*z* = 17 in Fig. 1 are similar to the intensities of the peaks with *m*/*z* = 34. The water content of the sample was very low (water was either initially present in the single-walled carbon nanotubes or trapped during manipulations with the sample in the open air). According to previously obtained data [1], the gas evolution upon heating from room temper-

ature to 400°C was no higher than 2% of the total gas evolution in the range to 550°C.

The spectra near $m/z = 18$ exhibited an analogous peak shape with a shoulder (Fig. 2b). Decomposition into Gaussians gave two peaks centered at m/z = 18.0093 and 18.04348, respectively. We attributed the latter more intense peak in Fig. 2b to the ions $[CD_3]^+$ (*18.04230666*) and $[CH_2D_2]^+$ (*18.04385482*). Taking into account the intensity of the peak that was attributed above to $[OH]^+$ ions, we can explain the peak intensity at $m/z = 18.0093$ by the presence of only $[H_2O]^+$ ions (*18.0105654*). In this case, the contribution of $[DO]^+$ ions (*18.00901722*) can be disregarded even though the value of m/z is appropriate. This follows from the fact that the peak centered at $m/z = 20.05$ has no peculiarities, whereas the resolution of the spectrometer allowed us to reliably distinguish between peaks corresponding to the ions $[CD_4]^+$ (*20.05640888*) and $[D_2O]^+$ (*20.02311946*). Analogously, the peak with $m/z = 19$ has no peculiarities that could be associated with the presence of HDO molecules.

The above consideration of the peak structure excludes the participation of impurity water molecules in the process of the deuterium exchange in the course of the thermobaric treatment. In this case, the absorption of water by the deuterated sample from the atmosphere is the most likely mechanism of the appearance of an H_2O impurity. This fact is quantitative evidence for the hydrophilicity of hydrogenated carbon nanostructures.

We turn our attention to the most intense peak in spectra *1–3* (Fig. 1). This is the peak with $m/z = 32$. It would be expected that, in addition to hydrocarbon ions, such as $[C_2D_4]^+$ (*32.05640888*), $[C_2D_3H_2]^+$ (*32.05795704*), and $[C_2D_2H_4]^+$ (*32.05950520*), $[O_2]^+$ ions (*31.98983004*) also contribute to the intensity of this peak. The O_2 oxygen molecules, as well as water molecules, can be sorbed on the sample on contact with air. The spectrum profile near $m/z = 32$ shown in Fig. 3 appears as a single peak centered at $m/z = 32.0572$. The minor peculiarity at $m/z = 31.986$ (inset in Fig. 3) could be attributed to the presence of oxygen; however, its intensity is comparable to the background level and lower than 0.5% of the base peak intensity. Consequently, the sorption of oxygen molecules by deuterated single-walled carbon nanotubes from the atmosphere is less effective than the sorption of water.

The peaks due to hydrocarbons and their fragments (Fig. 1) exhibited higher intensities in all of the spectra at the steps of heating from 100 to 400°C, and the fraction of molecular deuterium in the gas phase became overwhelming only at 500°C. Deuterated hydrocarbons were likely formed at the stage of the saturation of single-walled carbon nanotubes with deuterium. They were retained by the sample during prolonged evacuation at room temperature; however, they were removed at lower temperatures as compared with the D_2 molecules. Consequently, the kinetic barriers in the reaction paths of the hydrocarbon liberation should be lower than those for D_2 molecules. This suggests a difference in the positions of the hydrocarbon molecules and D_2 molecules in the structure of deuterated single-walled carbon nanotubes.

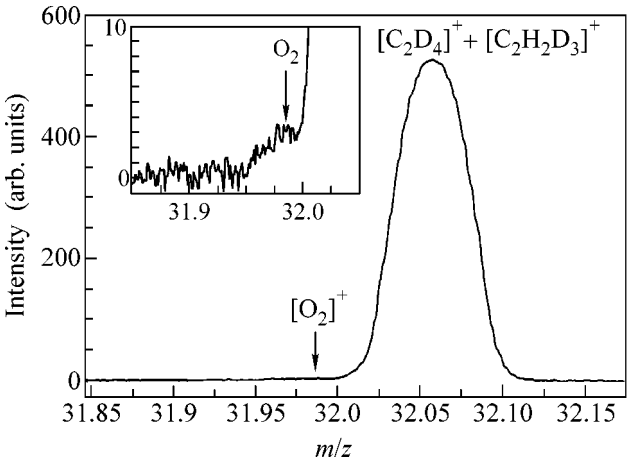

Fig. 3. Same as in Fig. 2 but at $m/z = 32$.

A comparison between the intensities of the peaks with even and odd mass numbers revealed one more property. The table, which summarizes the absolute and relative intensities of the peaks due to ions with m/z = 1, 2, 3, and 4, illustrates this property. It can be seen that the relative fraction of ions in which a deuterium atom is replaced by protium decreased as the temperature of the gas collection was increased. Similar changes with temperature can be observed by comparing the intensity ratios between the neighboring peaks of the hydrocarbons in the spectra corresponding to 100–400°C in Fig. 1. This property may be attributed to the greater mass of the D isotope and, correspondingly, to the longer time taken to diffuse from the sample rather than to the selectivity of single-walled carbon nanotubes for the absorption of isotopically different molecules.

Experimental peak intensities corresponding to deuterium and hydrogen ions. Values (%) normalized to the peak intensities of $[D_2]^+$ in the corresponding spectra are given in parentheses

T, °C	$m/z = 1$	$m/z = 2$	$m/z = 3$	$m/z = 4$
	$[H]^+$	$[H_2]^+$, $[D]^+$	$[HD]^+$	$[D_2]^+$
100	1.5 (2.1)	15.3 (21)	17.5 (24)	73.1 (100)
200	2.7 (1.6)	19.8 (12)	42.7 (26)	166.2 (100)
400	2.5 (0.5)	22.6 (5)	134.1 (27)	489.7 (100)
500	4.5 (0.2)	37.1 (2)	349.3 (17)	2056.6 (100)
550	3.4 (0.1)	43.1 (1)	667.2 (15)	4553.1 (100)

This work was supported by the Russian Foundation for Basic Research (project no. 03-02-16011); the International Science and Technology Center (project no. 2760); an integrated program on hydrogen energetics, the Russian Academy of Sciences and GMK Norilsk Nickel; the program "Controlled Synthesis of Fullerenes and Other Atomic Clusters," the Ministry of Science of the Russian Federation; and the program "New Materials and Structures," Branch of General Physics and Astronomy, the Russian Academy of Sciences.

REFERENCES

1. I. O. Bashkin, V. E. Antonov, A. V. Bazhenov, *et al.*, Pis'ma Zh. Éksp. Teor. Fiz. **79**, 280 (2004) [JETP Lett. **79**, 226 (2004)].
2. A. V. Krestinin, A. V. Raevskii, N. A. Kiselev, *et al.*, Chem. Phys. Lett. **381**, 529 (2003).
3. A. V. Krestinin, N. A. Kiselev, A. V. Raevskii, *et al.*, Eurasian Chem. Tech. J. **5**, 7 (2003).
4. I. W. Chiang, B. E. Brinson, A. Y. Huang, *et al.*, J. Phys. Chem. B **105**, 8297 (2001).
5. V. E. Antonov, I. O. Bashkin, S. S. Khasanov, *et al.*, J. Alloys Compd. **330–332**, 365 (2002).
6. *Thermodynamic Properties of Individual Substances: a Handbook*, Ed. by V. P. Glushko, 3rd ed. (Akad. Nauk SSSR, Moscow, 1979), Vol. 2, Book 2 [in Russian].
7. N. A. Shekhovtsov, *Magnetic Mass Spectrometers: Construction and Methods of Measurements* (Atomizdat, Moscow, 1971) [in Russian].
8. G. Audi and A. H. Wapstra, Nucl. Phys. A **565**, 1 (1993).

Translated by V. Makhlyarchuk

JETP Letters, Vol. 80, No. 12, 2004, p. 757. Translated from Pis'ma v Zhurnal Éksperimental'noĭ i Teoreticheskoĭ Fiziki, Vol. 80, No. 12, 2004, p. 889.

In Memory of Our Authors

R. Z. Levitin *et al.*, Cascade of Phase Transitions in $GdFe_3(BO_3)_4$, JETP Lett. 79, 423 (2004).

Rudol'f Zinov'evich Levitin, a Moscow State University professor, passed away on February 26, 2004. He was a charming person, well-known scientist, physicist and experimentalist, and specialist in magnetism.

Levitin's scientific style was characterized by deep insight into the physical essence of the phenomena under investigation, strict and clear statement of experimental procedures, and clearness in his presentation of results. He obtained fundamental results that considerably expanded the physical understanding of the nature of magnetism and mechanisms of phase transitions in rare-earth ferro-, ferri-, and antiferromagnets. Levitin's works on magnetoelastic effects are fundamental to the physics of magnetic phenomena and have made a considerable contribution to the microscopic theory of magnetoelasticity. The complex investigations of the magnetism of rare-earth and uranium substances carried out by Levitin with a group of scientists from Moscow State University and institutions of the USSR Academy of Sciences were awarded a State Prize of the USSR. The phenomenon of giant magnetostriction studied by him in rare-earth and uranium compounds was heralded as a discovery.

Levitin's works have been highly valued, and his extensive and fruitful contacts with foreign scientists promoted the integration of Russian science into the world scientific community. The scientific results obtained by Levitin were summarized in two monographs and a cycle of fundamental reviews that are used for educating new specialists in magnetism. Rudol'f Zinov'evich won respect and widespread fame in the scientific world due to his devotion to science, great scientific achievements, exclusive erudition in solid state physics, curiosity and openness to new knowledge, and his highly valued qualities as a human being.

I. L. Karpikhin *et al.*, Search for *P*-odd Asymmetry of Prompt Neutron Emission in ^{235}U Fission Induced by Cold Polarized Neutrons, JETP Lett. 80 (11), 675 (2004).

Igor' L'vovich Karpikhin, a leading electronic engineer at the Institute of Theoretical and Experimental Physics (ITEP, Moscow, Russia), passed away unexpectedly on March 8, 2004, at the age of 66.

Karpikhin joined ITEP upon graduation from an instrumental engineering college on March 8, 1960. Then, working at the ITEP, he received his higher education at the Moscow Power Engineering Institute. Beginning with the creation of simple lamp circuits, he was later involved in the development, adjustment, and exploitation of the overwhelming majority of devices that were created and commissioned at the Laboratory of Neutron Physics. In particular, his talent was directed into all the devices for studying the effects of spatial-parity violation in nuclear interactions, into beta NMR spectrometers, and into a setup for studying gravitational effects. He worked as a physicist and experimentalist with neutron beams at the ITEP; St. Petersburg Nuclear Physics Institute (PNPI, St. Petersburg, Russia); Moscow Engineering Physics Institute; Laue–Langevin Institut (Grenoble, France); and Berliner Zentrum für Neutronenstreuung, Hahn–Meitner Institut (Berlin, Germany). He was a coauthor of numerous works on fundamental nuclear physics.

Igor' L'vovich was a versatile individual: he liked music and poetry and knew literature and history well. He was a considerate and responsive person and a reliable friend, who was always ready to help with advice and action. He was the soul of the group and an active organizer and a participant in all the public meetings at the laboratory. His foreign colleagues, as well as the physicists at the ITEP, the Laboratory of Neutron Physics at JINR, and PNPI, loved and respected him.

0021-3640/04/8012-0757$26.00 © 2004 MAIK "Nauka/Interperiodica"

JETP Letters, Vol. 80, No. 12, 2004, p. 758.

Erratum: "Pentaquark Decay Is Suppressed by Chirality Conservation" [JETP Lett. 80, 386 (2004)]

B. L. Ioffe and A. G. Oganesian

PACS numbers: 12.38.–t, 12.39.–x

In the article "Pentaquark Decay Is Suppressed by Chirality Conservation" there are the following misprints:

The local 5 quark current η_θ given by Eq. 1 in fact corresponds to isospin $T = 1$ not to $T = 0$, as was stated in the paper. For this reason, the sum rules presented in the paper refer to $T = 1$ $uudd\bar{s}$ pentaquark state and not to the observed $\Theta^+(1540)$ state with the isospin $T = 0$. The current corresponding to the sum of two terms in (1), which was erroneously referred to as current $T = 1$, is in fact a mixture of states $T = 0$ and $T = 2$. There are certain errors in Eq. 7: the last term in the first set of square brackets, $-4m_s a$, should be replaced by $-(20/3)m_s a$; in the second set of the second square brackets, the term $(1/2)\gamma$ should be replaced by $(5/6)\gamma$; and in the fourth line of Eq. 7, the term $(13/3)\gamma$ should be replaced by $(25/3)\gamma$. There is also a misprint in Eq. 7: in the first term in the curly brackets, the factor $1/a$ was lost. These errors alter the curves in Fig. 1 within the limit of their accuracy, but the agreement of the two curves in Fig. 1a became a bit worse. As a result, a definite conclusion could not be obtained on the existence of the pentaquark state with the isospin $T = 1$.

These errors clearly do not influence the main result of the paper—the suppression of pentaquark decay by chirality conservation and the estimation of Γ_θ.

We are grateful to M. Nielsen, N. Kotchelev, and H.-J. Lee, who directed our attention to the errors.

0021-3640/04/8012-0758$26.00